Dissertations and Theses

11-2014

Exploration of a Computational Fluid Dynamics Integrated Design Methodology for Potential Application to a Wind Turbine Blade

Gaurav Kapoor

EXPLORATION OF A COMPUTATIONAL FLUID DYNAMICS INTEGRATED DESIGN METHODOLOGY FOR POTENTIAL APPLICATION TO A WIND TURBINE BLADE

By

GAURAV KAPOOR

A Thesis Submitted to the Department of Aerospace Engineering, College of Engineering
In Partial Fulfillment of the Requirements for the Degree of
Masters of Science in Aerospace Engineering

Embry-Riddle Aeronautical University
Daytona Beach, Florida-32114.
December 2014

EXPLORATION OF A COMPUTATIONAL FLUID DYNAMICS INTEGRATED DESIGN METHODOLOGY FOR POTENTIAL APPLICATION TO A WIND TURBINE BLADE

By

GAURAV KAPOOR

This thesis was prepared under the direction of the candidate's Thesis Committee Chair, Dr. Sathya Gangadharan, Professor, Daytona Beach Campu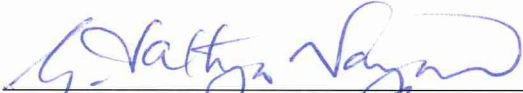s, and Thesis Committee Members Dr. Reda Mankbadi, Distinguished Professor, Daytona Beach Campus, and Dr. Mark Ricklick, Assistant Professor, Daytona Beach Campus

The Thesis has been approved by the Thesis Committee and is submitted to the Department of Aerospace Engineering in partial fulfillment of the requirements for the degree of Masters of Science in Aerospace Engineering.

Thesis Review Committee:

_____
Dr. Sathya Gangadharan,
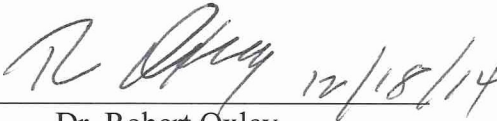Committee Chair

A. dyimtis (on behalf of)
_____
Dr. Reda Mankbadi
Committee Member

_____
Dr. Mark Ricklick
Committee Member

_____
Dr. Yi Zhao
Graduate Program Chair

_____ 12/18/14
Dr. Robert Oxley
Associate Vice President, Academics

ACKNOWLEDGEMENT

I would like to thank Dr. Sathya Gangadharan, my advisor on this research, for his consistent support and guidance throughout this research project, to which he has generously devoted much time and effort.

On the same note, I would like to express my gratitude to Dr. Reda Mankbadi and Dr. Mark Ricklick, for taking time off their busy schedule to serve as committee members. Their suggestions and help, provided more insight to the work for which I am really grateful.

In addition, I would like to thank the staff of the Mechanical and Aerospace Engineering Department for their guidance and patience in helping me through so many of the technicalities that come with research.

Last but not the least, I owe more than thanks to my family members, which includes my grandparents, parents and my younger brother for their financial support and unending encouragement throughout my life, without which it would have been impossible for me to finish my graduate education seamlessly.

ABSTRACT

Author: Gaurav Kapoor

Title: Exploration of a Computational Fluid Dynamics Integrated Design Methodology for

        Potential Application to a Wind Turbine Blade

Institution: Embry-Riddle Aeronautical University, Daytona Beach, FL

Degree: Master of Science in Aerospace Engineering

Year: 2014

The main purpose of this thesis is to conduct a parametric sensitivity study on the blade design of AOC 15/50 wind turbine based on a CFD approach and optimize the blade design for maximizing the power output. The ANSYS® Fluent® flow solver using the k-ω SST turbulence model was validated by simulating the flow over two dimensional airfoils comprising the AOC 15/50 wind turbine blade. The CFD results have shown a considerable agreement with the experimental data for the airfoils. Parametric correlation study and sensitivity analysis were conducted by performing actual flow simulations over the turbine blade using ANSYS® Fluent®. This illustrates the dependence of power output on the blade design parameters. Parametric correlation study reveals that the blade design variables on the outer 40% of the blade span have a predominant effect on the power output of the blade, while the obtained scatter plots and determination matrix indicate the blade optimization problem setup as non-linear and quadratic fit. The most sensitive design parameters are used to formulate the flow optimization problem. A response surface optimization (RSO) methodology is employed for carrying out the blade shape optimization process. Design of Experiments (DoE) using the Latin Hypercube Sampling (LHS)

algorithm is used to construct a robust response surface model, which is then searched for the optimized design using the Nonlinear Programming by Quadratic Lagrangian (NLPQL) technique. Two optimization routines are carried out by varying the geometric constraints on the blade. First optimization routine constrained the blade length and maximum chord occurring at a 40% span location from the hub to be fixed, yielding a design that performs marginally well up to the wind speed of 9.2 m/s with a maximum power increment of 7.55 % occurring at the 8.03 m/s wind speed. The search for the second optimization routine was initialized in the design space with the best candidate point obtained from the first optimization routine. Second optimization routine generated a design configuration that resulted in an increased blade length and surface area, thus leading to an overall lift force augmentation producing a 25.26% increase in the power output. Both the optimized candidates obtained were validated using the flow solver to verify the optimized design for maximized power output. The coefficient of pressure plots at various span locations of the blade bolster the claim that most of the mechanical power is produced in the outer 30-40% of the blade.

TABLE OF CONTENTS

LIST OF FIGURES

LIST OF TABLES

NOMENCLATURE

λ	Tip Speed Ratio
ω	Angular Velocity
R	Rotor Radius
v_0	Free Stream Velocity
n	Rational Speed
π	Pi (Value = 3.14159)
u	Axial Induced Velocity
a	Axial Induction Factor
$P_{available}$	Shaft Power or Available Power
ρ	Density
C_P	Power Coefficient
C_p	Pressure Coefficient
P	Static Pressure
P_0	Free Stream Static Pressure
r	Position Vector
v	Absolute Velocity
v_r	Relative Velocity
p	Local Pressure
τ	Local Stress Tensor
F	External Body Forces or Gravitational Forces

S_h	Heat Energy Added
E_r	Relative Internal Energy
H_r	Relative Total Enthalpy
ω	Specific Dissipation Rate
k	Mean Turbulent Kinetic Energy
x_i	Position Vector in Tensor Notation
μ	Viscosity
$\mathbf{X}$	Vector of Variables
$\mathbf{X}_{DoE}$	Design of Experiments
f	Objective function
$g_i,\ h_k$	Constraint Functions
m , p	Equality and Inequality Constraints
N_s	Number of Sample Points
N_{var}	Number of Design Variables
DV	Design Variables
$F(\mathbf{X})$	Function of $\mathbf{X}$
ϵ	Total Error
ε_i	Error at any Point i
y_i	Actual Value
$\hat{y}_i$	Predicted Value
σ_a	Adjusted Root Mean Square Error
R^2_{adj}	Coefficient of Multiple Determination
R2	Full Model Coefficient of Determination

ABBREVIATIONS

HAWT	Horizontal Axis Wind Turbine
VAWT	Vertical Axis Wind Turbine
CFD	Computational Fluid Dynamics
AOC	Atlantic Orient Corporation
NWTC	National Wind Technology Center
NREL	National Renewable Energy Laboratory
WT	Wind Turbines
GWEC	Global Wind Energy Council
MW	Megawatt
FEM	Finite Element Method
BEMT	Blade Element Momentum Theory
TSR	Tip Speed Ratio
CAD	Computer-Aided Design
RANS	Reynolds-Averaged Navier–Stokes Equations
FSI	Fluid-Structure Interaction
N-S	Navier-Stokes Equations
HPC	High Power Computing
STP	Standard Temperature and Pressure
MRF	Moving Reference Frame
SLM	Sliding Mesh
CAE	Computer Aided Engineering
GBOM	Gradient-Based Optimization Methods

MDO	Multidisciplinary Design Optimization
RSO	Response Surface Optimization
RSM	Response Surface Model
DV	Design Variables
DoE	Design of Experiments
RMS	Root Mean Square
LHS	Latin Hypercube Sampling
NLPQL	Nonlinear Programming by Quadratic Lagrangian
LES	Large-Eddy Simulation
NURBS	Non-Uniform Rational B-Splines

CHAPTER-1

Introduction

Globally, growing energy demands and mounting concerns about the effects of pollution from fossil fuels have driven the development of new and diverse sources of energy. Amongst the many sources of energy available, renewable power offers clean and sustainable options and has therefore seen significant development in the past decades. One of the sources of renewable energy is wind.

Wind power is harvested by wind turbines, ranging from small household units to massive farms of multi-megawatt machines. Many current developmental efforts are aimed at taking advantage of more advantageous wind conditions, which involves building taller, larger turbines and includes offshore technologies. Current efforts also include structural, mechanical, and aerodynamic research all aimed at improving the efficiency and durability of existing and future machines.

Wind turbines (WT) can be roughly classified according to the design energy production in three categories:

- Small size WT: Energy production < 5kW in design condition, suitable for in-house applications.

- Medium size WT: 5kW < Energy production < 100kW in design condition, suitable for buildings and small industries.

- Large size WT: Energy production > 100kW in design conditions, suitable for industries and large living environments power supply systems.
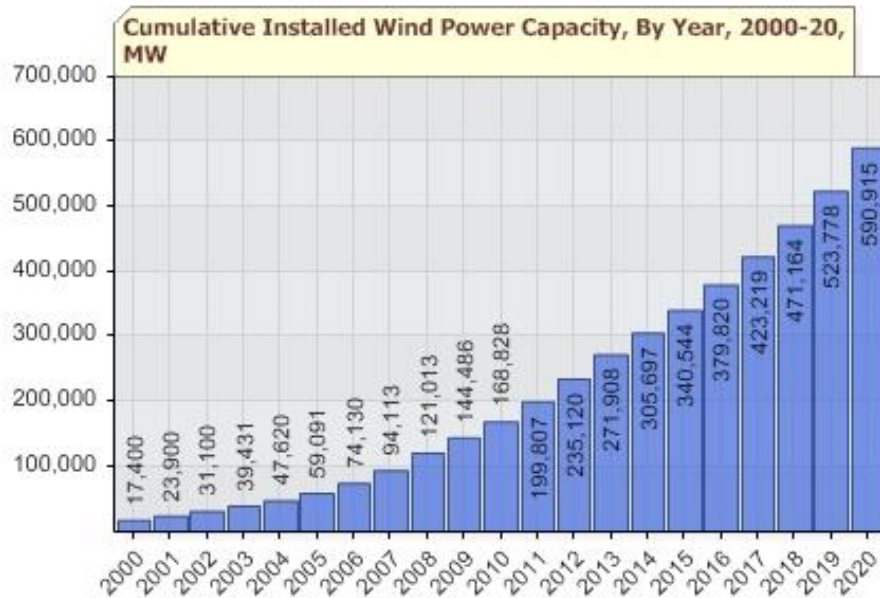
Figure 1: Projected Cumulative Installed Wind Power Capacity (MW) By Year 2020.
Mountain, Kirby. 2013. Web. 1 Oct. 2014. http://www.gf.uns.ac.rs/~wus/wus09/Alternative%20energy/statistic.html

The Global Wind Energy Council (GWEC) released its 2013 global wind statistics report, with cumulative global installed wind capacity reaching a total of 318,137 MW by the end of 2013, an increase of nearly 200,000 MW in the past five years. Statistics also reveal that 35,467 MW of new wind capacity was installed in the year 2013 alone. While China tops the list of countries with a 28.7 % share in the top ten countries census survey of installed cumulative capacity by the end of year 2013, US is not far behind with a 19.2% share. Among the continents, Asia has shown the fastest growth from the year 2005 to 2013, in terms of the annual installed wind capacity [1].

With the ever increasing energy needs and wind energy coming to the forefront as a competitive form of clean and renewable energy, the prospects for 2014 and beyond look much brighter as the projected cumulative installed wind power capacity by the year 2020 is slated to increase by a staggering 93% from the year 2014 (Figure 1).

In the early advent of wind turbines, the research on wind turbine blade design was limited to theoretical study, field testing and real time wind tunnel testing which required tremendous resources [2]. Another area of study and the focus of this thesis, is to increase the wind turbine power output through blade design optimization. The development of computer aided design (CAD) codes is another way to design and analyze the wind turbine blades. Aerodynamic performance of wind turbine blade can be analyzed using Computational Fluid Dynamics (CFD), a branch of fluid mechanics that uses numerical methods and algorithms to solve physical flow problems.

Meanwhile, finite element method (FEM) can be used for the blade structural analysis, conventional analytical methods like blade element momentum (BEM) can be used to predict the blade aerodynamics. Analytical methods are often based on the BEM approach and require pre-calculated data inputs like the airfoil polar curves and other empirical assumptions for off-design operation [3]. Compared to traditional theoretical and experimental methods, numerical methods like CFD are more efficient for the performance analysis and optimal design of wind turbine blades [4]. Wind power continues to grow as a source of energy throughout the world and the performance of wind turbines has improved significantly. Continued efforts aimed at improving wind energy technologies will make this renewable resource even more viable.

1.1 Motivation

As fundamentally known, with an increase in the turbine blade length (Figure 2), aero-elastic effects become more prominent, contributing to fatigue that shortens the life of a turbine [5].

Moreover, longer blade requires taller tower structures capable of withstanding increased loads, thereby increasing the weight and therefore cost of the turbine.
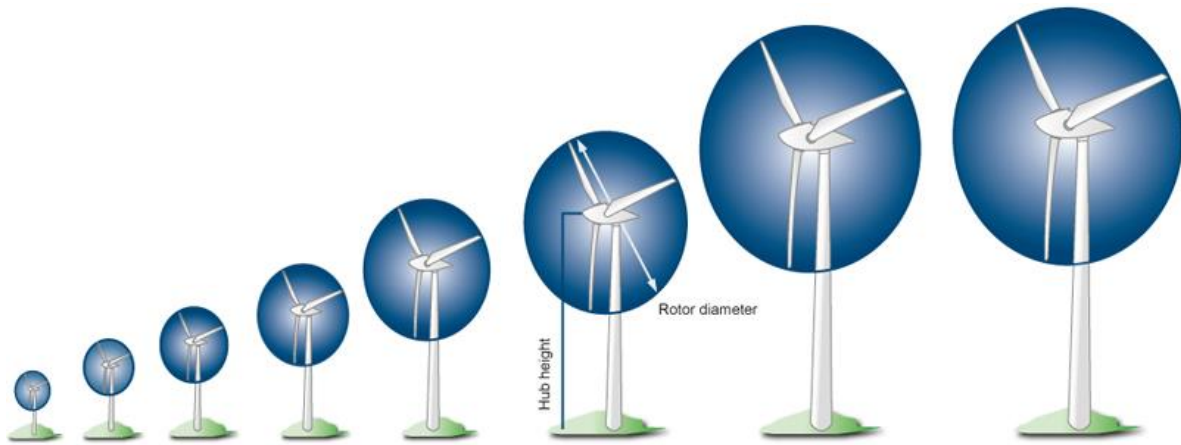
	1985	1990	1995	2000	2005	2008	2011	2012
Nominal power (kW)	80	250	600	1,500	3,000	6,000	7,500	7,500
Rotor diameter (m)	20	30	46	70	90	126	127	154
Hub height (m)	40	50	78	100	105	135	135	160

Figure 2: Growth And Development in Wind Turbines since 1985
German Wind Energy Association (BWE), Dena German Energy Agency. N.D. Web. 1 Oct. 2014.
http://work.renewables-made-in-germany.com/en/renewables-made-in-germany-start/wind-energy/wind-energy/outlook.html

To better carry the structural loads of large turbines, blades with very thick airfoil sections have been proposed. The outcome of such thick sections on aerodynamic performance is difficult to predict, as they rely heavily on blade element momentum theory (BEMT), which cannot accurately predict the response of blade that violate thin airfoil assumptions [6]. Additionally, such methods model aerodynamics as basically two-dimensional phenomena, yet very large turbines with blunt airfoil sections exhibit a great deal of three-dimensional behavior in their flow fields. Analysis of such complex flow fields around the blade requires a more physics-based approach, such as CFD. Unlike BEMT methods, which neglect three-dimensional effects and aerodynamic phenomena occurring on the blade surfaces, CFD models the exact aerodynamic environment using physics-based equations, rather than the empirical relations based on assumptions.

Until recently, majority of the computational studies on wind turbine aerodynamics have used simple and inexpensive methods based on BEMT. These analytical methods provide a basic insight into rotational flows around a turbine, but only under the simple operating conditions of constant wind speed and no yaw. According to the description by Leishman [7], BEMT methods operate with the underlying *independence principle*, wherein the aerodynamics of each airfoil section along the blade span is determined independently of neighboring blade section. Consequently, BEM methods completely neglect span-wise flow and other three-dimensional effects associated with the rotating turbine flows, which have been shown to have a significant effect in lift augmentation and stall delay near the blade root [8]. Therefore, BEMT methods with the applied three-dimensional corrections, under-predict torque on the blade resulting in inaccurate power prediction [9]. Blade design based on BEMT methods can result in turbine structures that buckle to fatigue much earlier than their expected lifespan. Modern computational methods that use CFD flow-field data as their input, greatly improve performance predictions since CFD computes directly from the underlying equations of fluid motion and relies on fewer assumptions as compared to the BEMT methods. CFD methodology can reduce many of the inaccurate simplifying assumptions used in common wind turbine analytical methods.

1.2 Aim and Objectives

Aim

This thesis aims to evaluate the aerodynamic performance of a variable-speed, fixed-pitch Atlantic Orient Corporation AOC 15/50 HAWT [10] rotor through two and three dimensional CFD

analysis. The rotor blade is then optimized for maximizing the torque on the blade, thereby improving the overall power output of the rotor.

Objective

The objective of this thesis is to establish the two and three dimensional CFD models of a wind turbine rotor blade, so as:

I.   To analyze the flow using the commercial flow solver ANSYS® Fluent 14.5 on the family of thick airfoil sections S819, S820 and S821 [11] comprising the turbine blade of AOC 15/50 HAWT. The purpose of this two-dimensional airfoil flow analysis is to compare the results with the available experimental datasheet of each airfoil and to predict, validate the best turbulence model in the ANSYS® Fluent 14.5 flow solver that can be extended to the flow analysis of a full three-dimensional turbine rotor.

II. To establish the flow around the three dimensional AOC 15/50 HAWT rotor and predict the wind turbine power output at different wind speeds.

III. To study the dependence (sensitivity) of blade geometric/design parameters (what-if scenario) on the power generated using ANSYS® Fluent 14.5 using the Design of Experiments (DOE) approach of the inbuilt ANSYS® DesignXplorer.

IV. To identify the most sensitive blade geometric (input) parameters and formulate the flow problem with the most sensitive input parameters as the design variables and the objective function defined as the maximization of the torque on the blade.

V. To find the blade design configuration that produces the maximum power output using the Response Surface Optimization module in ANSYS® Workbench™ and validate the same by conducting flow simulations using ANSYS® Fluent 14.5.

CHAPTER-2

Wind Turbine Design and Working Principle

The structure itself is rather simple and fairly common nowadays (see Figure 3). The rotor is made of generally three blades fixed to a hub. The hub is responsible for the blade control and for connecting the rotor mechanism to the rotor shaft (and consequently to the electrical generator). The nacelle (Figure 4) is the enclosure that holds all mechanical organs of the machine (gearbox, rotor brake, bearings, etc.) as well as the generator and control systems. The bedplate, which connects the nacelle to the tower, is responsible for a very important movement of the WT, the yaw system, allowing the HAWT to face the direction of the wind flow. Finally, the tower is the structure that holds the machine in place and that connects the HAWT to the electrical grid.
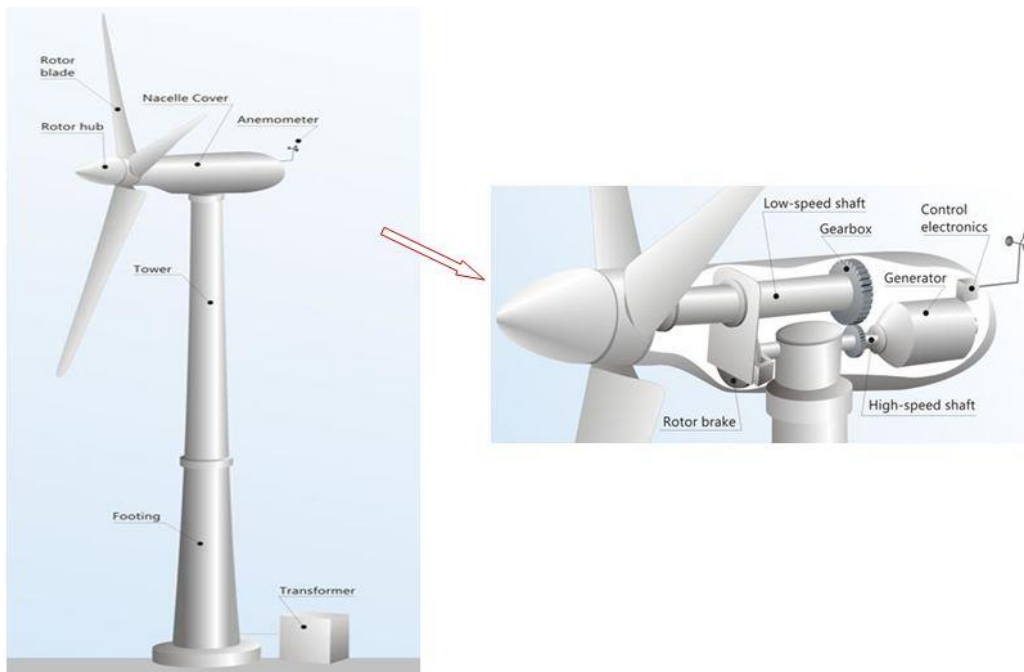
Figure 3: Schematic of a Wind Turbine Generation System
N.D. Web. 1 Oct. 2014. http://becuo.com/wind-turbine-diagram
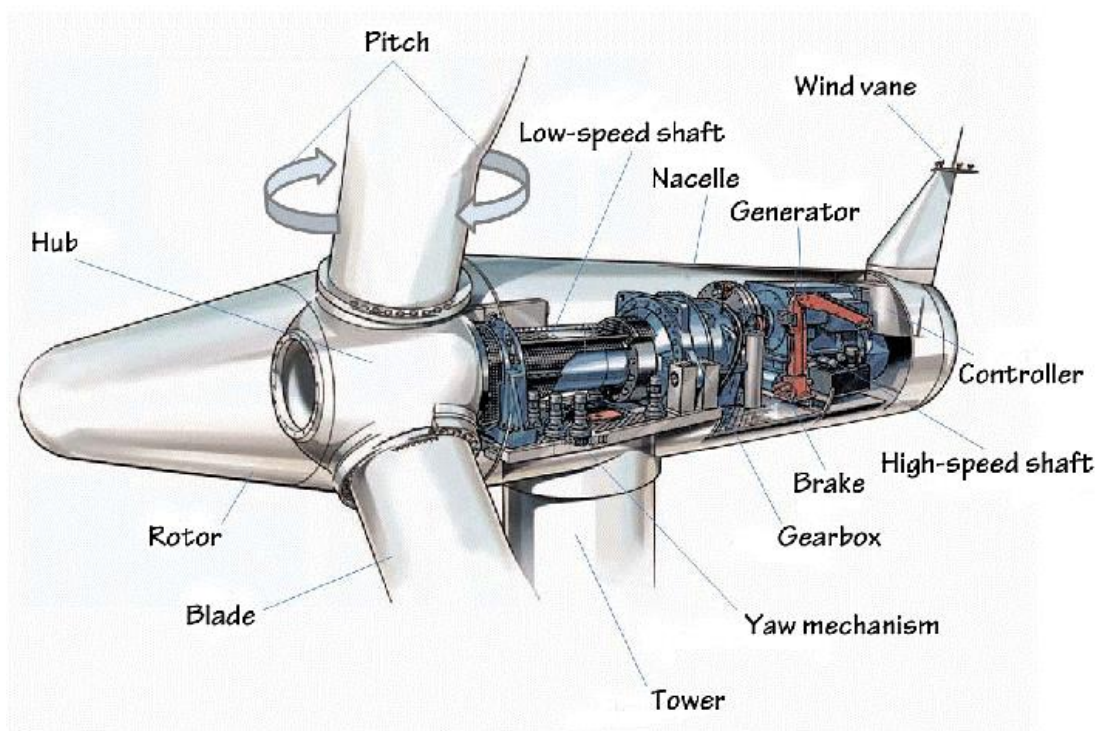
Figure 4: Schematic of Internal Components of a Modern HAWT
Center on Globalization, Governance and Competitiveness, Duke University. Web. 1 Oct. 2014. http://aero2all.blogspot.com/

2.1 Airfoils and Blade Design

The most important factor in designing a wind turbine is the choice of airfoils from which the blade gets it aerodynamic shape, as the entire blade is shape lofted from these airfoils sections. The lift generated from these airfoils at every section causes the rotation of the blade, also the performance of the blade is highly dependent on airfoil performance.

The airfoil near the blade root are usually thicker and are flat-back (or rounded trailing edge) to make the blade thicker at the root section. The airfoil section at the tip of the blade has a sharp trailing edge for achieving higher tip speed ratio [12].
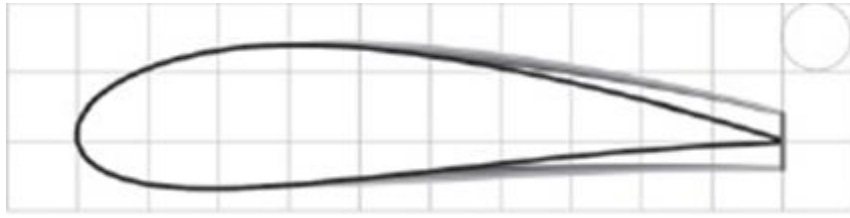
Figure 5: Profiles of Flat-back and Sharp Trailing Edge Airfoils [13]

The airfoil sections closer to the tip of the blade generate higher lift force due to the speed variation in the relative wind, the purpose of airfoils at the root of blade is mainly structural, having a minimal contribution to the aerodynamic performance of the blade. Thus the root section of the wind turbine blade is thicker and stronger than its tip section (Figure 5). Wind turbine blades are shaped to extract maximum power from the wind at the minimum cost involved. Primarily the blade design is driven by the aerodynamic and performance requirements. But in true sense, the economics mean that the blade shape is a compromise to keep the cost of construction, operation and maintenance to a minimum. The blade design procedure starts with obtaining a solution set for both aerodynamic and structural efficiency. The best blade design is a tradeoff between both aerodynamic performance and structural stiffness.

2.2 Blade Twist

Analogous to an airplane wing, wind turbine blades work by generating lift force due to their airfoil shape. The more curved side generates low air pressures while high pressure air pushes on the pressure side of the airfoil. The net result of this pressure difference on either side of the blade surface is a lift force perpendicular to the direction of flow of the air.

Since the turbine blade is in motion, the true wind is incident on it from a different angle. This is called *apparent wind* as shown in Figure 6. The apparent wind is stronger than the true wind but

its angle is less favorable to generate a driving force on the blade. This also means that the lift force contributes to the thrust on the rotor. To maintain an effective angle of attack to generate lift, the blade must be turned further from the true wind angle which gives twist to the blade from root to tip.
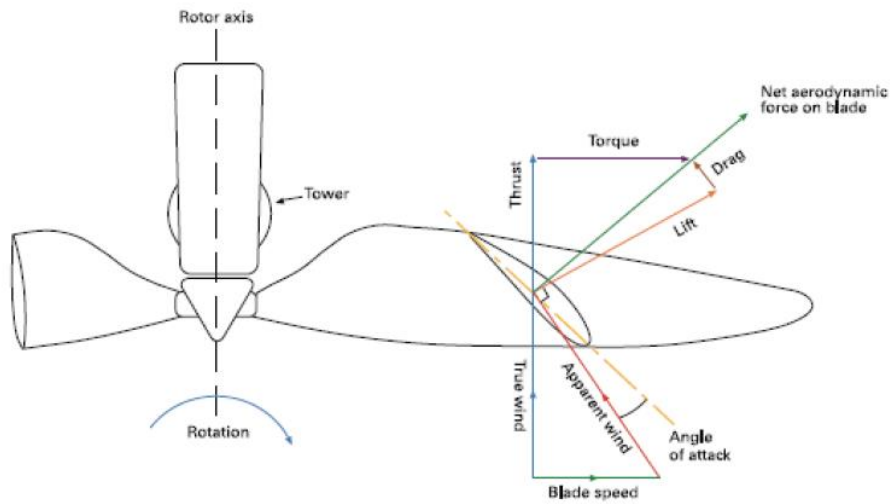
Figure 6: Aerodynamic Forces Acting on the HAWT Blade [14].
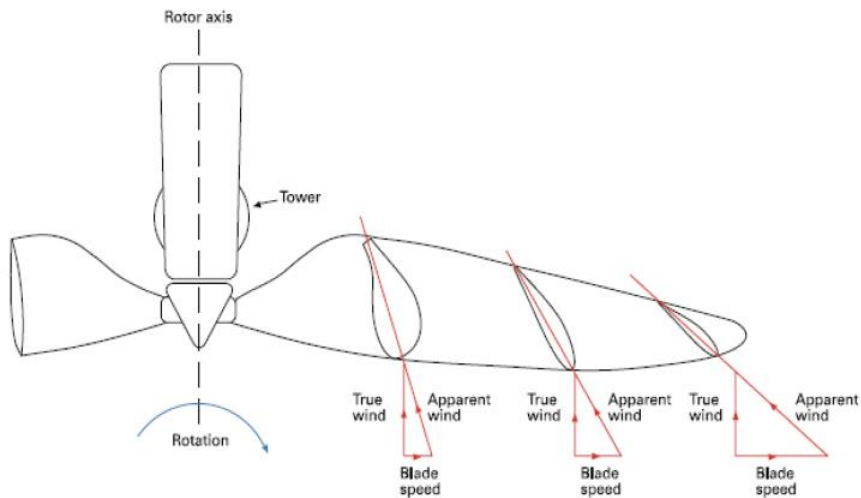
Figure 7: Blade Twist at Span-wise Sections (Airfoils) and Apparent Wind Angles [14]

As can be seen from the Figure 7, the blade tip is moving faster through the air compared to the blade region closer to the root, hence the tip is operating at a greater apparent wind angle. Thus, the blade needs to be turned further at the tips than at the root, which essentially means it must be built with an inherent twist along is length. The requirement to twist the blades has implications on the manufacturing processes.

2.3 Tip Speed Ratio (TSR)

The rotational speed at which the turbine operates is a fundamental choice in the blade design. It is defined in terms of the speed of the blade tips relative to the free wind speed. This is called the tip speed ratio (λ) and its definition is shown in equation (1).

$$\lambda = \frac{\omega R}{v_0} \tag{1}$$

Where, ω is the angular velocity of the wind turbine rotor, R is radius of the rotor and v_0 is the free wind speed. A higher tip speed ratio (TSR) induces the net aerodynamic force on the blade (component of lift and drag) to be approximately parallel to the rotor axis (Figure 8). The lift to drag ratio can be affected severely by presence of dirt or roughness on the blade surfaces [15].
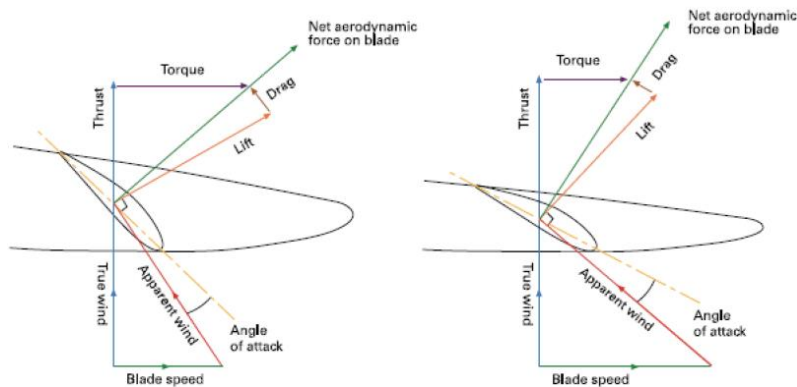
Figure 8: Effect of TSR on the Blade Performance [14]

Low tip speed ratio unfortunately results is lower aerodynamic efficiency due to two effects. Since the lift force on the blade generates torque, according to the laws of motion, it has an equal but opposite effect on the incident wind, tending to push it around tangentially in the other direction. As a result, the air downwind of the turbine has a *swirl*, i.e. it spins in the opposite direction to the blade rotation, as depicted in Figure 9. This swirl represents lost power which reduces the available power that can be extracted from the incident wind. Lower rotational speed requires higher torque to maintain the same power output, so lower tip speed ratio results in greater wake swirl losses.
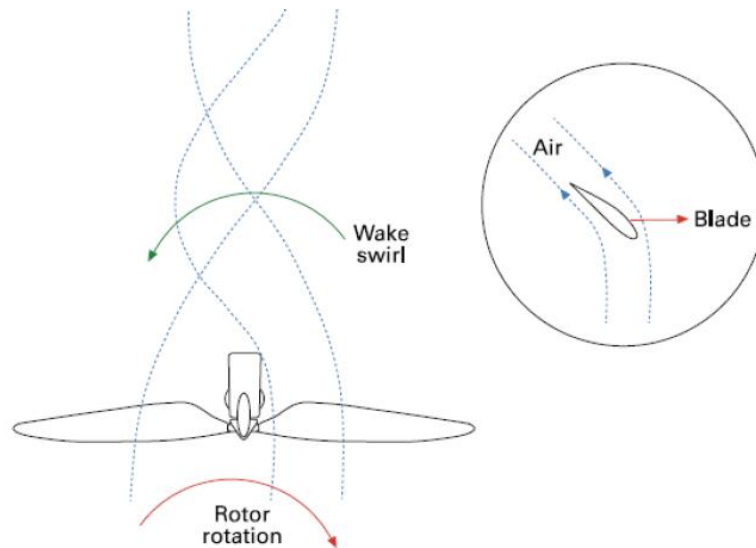
Figure 9: Swirling Flow in the Wind Turbine Wake [14]

The other reason for the reduction in aerodynamic efficiency at low tip speed ratio is due to the tip losses, where high-pressure air from the upwind side of the blade escapes around the blade tip to the low-pressure side, thereby wasting energy. Since power is a product of blade torque and rotational speed, at slower rotational speed the blades need to generate more lift force to maintain the same power output.

In order to generate greater lift for a given length, the blade has to be wider, geometrically speaking, a greater proportion of the blade's width is designed to be close to the tip (Figure 10).
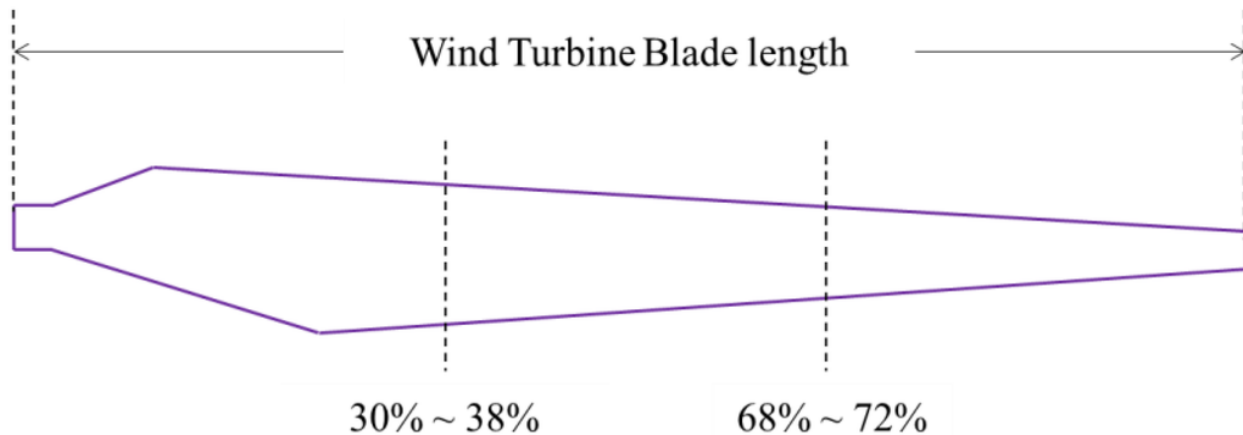
Figure 10: Typical Wind Turbine Blade Planform View

The higher lift force on a wider blade translates to greater structural loads on the outer components such as the hub and bearings. There are practical limits on the absolute tip speed ratio as well. At these speeds, bird impacts and rain erosion starts to decrease the longevity of the blades and noise increases dramatically with the tip speed [16].

2.4 Wind Turbine Operation

Wind turbine operating condition depends on the speed of free stream wind speed; generally, it can be divided into three operation modes (Figure 11),

- Cut-in speed - the minimum wind speed at which the turbine blades overcome frictional force and begin to rotate.

- Operation mode - the range of wind speeds within which the wind turbine actively generates power.

- Cut-out mode - the speed at which the turbine is brought to rest to avoid structural damage due to high wind speeds.
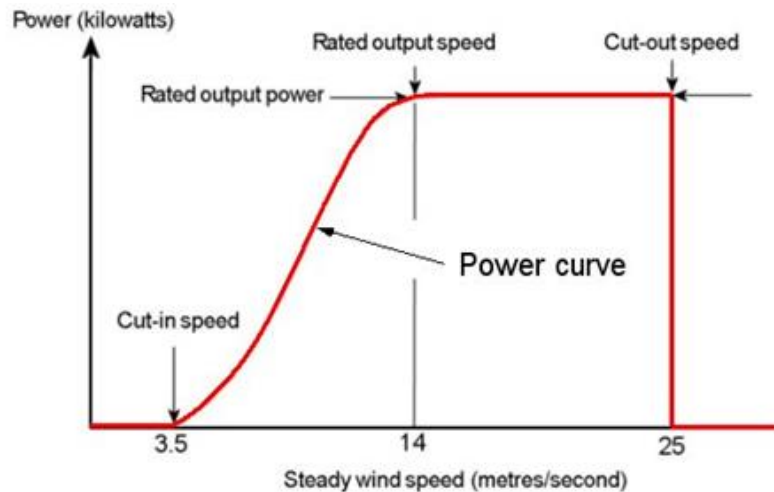
Figure 11: Typical Wind Turbine Power Output Curve

For AOC 15/50 HAWT, if free stream wind speed is less than the cut in speed (4.9 m/s), the wind turbine rotor will not rotate due to less available wind energy and insufficient torque produced to overcome the inertia of the blade. The rotor begins to rotate at speed of 4.9 m/s and begins to generate power. This region of the blade operation from the cut-in wind speed of 4.9 m/s to the cut-out wind speed of 22.4 m/s is referred to as the operation mode or active mode of the wind turbine. Ideal or rated wind speed is 12 m/s for the AOC 15/50 wind turbine. And if free stream wind speed is above 22.4 m/s which is cut-out speed for the AOC 15/50 HAWT, rotor stops rotating to prevent any damage or failure to wind turbine blade and other gear/bearing systems embedded in the nacelle.

2.2 Wind Turbine Aerodynamics

A wind turbine extracts mechanical energy from the kinetic energy of the wind by slowing down the wind. It can either be a Horizontal-Axis Wind Turbine (HAWT) or a Vertical-Axis Wind Turbine (VAWT), depending on either it rotates around its horizontal axis or vertical axis, respectively. In the present work, the turbine in contention is a HAWT configuration.

As discussed earlier, many methods for computing the aerodynamic performance of wind turbines exist. In 1935, Betz and Glauert [17] derived the classical analysis method, the Blade Element Momentum Theory (BEMT), which combines the *Blade Element* and *Momentum* theories. But in this present work, only flow equations from the *Actuator Disc* concept are used and the same will be discussed below.

2.2.1 Actuator Disk Concept

The actuator disk concept is widely used to define the basic aerodynamic flow around the wind turbine. According to this concept, the wind turbine is considered as an ideal actuator disk: frictionless, with an infinite number of blades and with no rotational velocity component in the wake downstream of the turbine. The flow around the turbine is assumed to be homogeneous and steady, while the air is considered incompressible.

If the mass of air passing through the turbine is assumed to be separated from the mass that does not pass, the separated part of the flow field remains a long stream tube lying up and downstream of the turbine. As the flow approaches the wind turbine, it suffers a velocity drop, and in order to compensate for this drop, the stream tube expands (Figure 12).

Actuator disk with stream tube
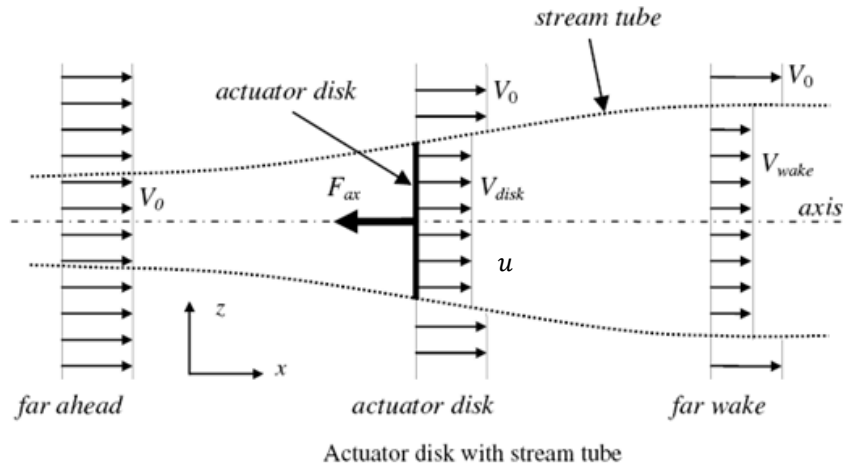
Figure 12: Actuator Disk Concept for Wind Turbine Rotor
Giorgio Crasto. 14 Aug. 2014. Web. 1 Oct. 2014. http://winddturbin.com/actuator-disc-theory-wind-turbines/

From figure 13, the non-dimensionalized difference between the free stream velocity v_0 and axial induced velocity u, the *axial induction* factor is defined as:

$$a = \frac{v_0 - u}{v_0} \tag{2}$$
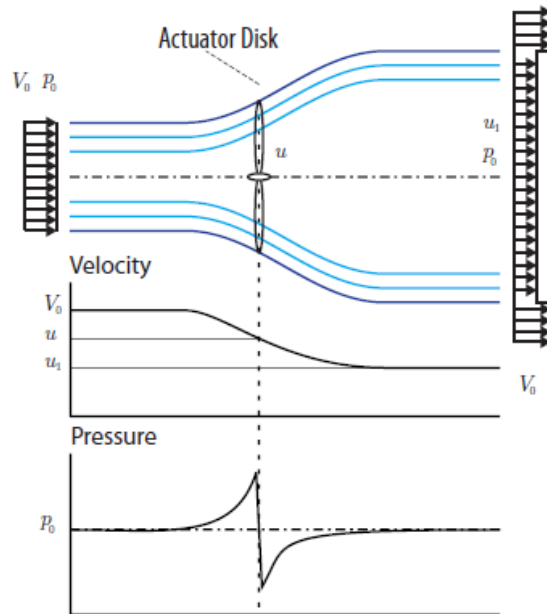
Figure 13: Actuator Disk Concept, Pressure and Velocity Profiles
Giorgio Crasto. 14 Aug. 2014. Web. 1 Oct. 2014. http://winddturbin.com/actuator-disc-theory-wind-turbines/

17

The shaft power $P_{available}$ is calculated by using the energy equation on a control volume defined by the stream tube and assuming no change in the internal energy of the flow (since it is assumed to be frictionless). The power available is;

$$P_{available} = 2 \rho v_0 a (1 - a) A_R \tag{3}$$

where A_R is the area of the rotor and which is often non-dimensionalized with respect to $P_{available}$ as a power coefficient C_P ,

$$C_P = \frac{P_{available}}{\frac{1}{2} A_R \rho v_0^3} \tag{4}$$

The power coefficient for the ideal wind turbine may also be written as:

$$C_P = 4 a (1 - a)^2 \tag{5}$$

Differentiation C_P with respect to a yields,

$$\frac{dC_P}{da} = 4 (1 - a) (1 - 3a) \tag{6}$$

From equation (7) the maximum value of $C_P = {}^{16}/_{27} = \sim 0.593$ is obtained for $a = {}^1/_3$. This theoretical maximum value is known as the *Betz Limit* [18] and it is not possible to design a wind turbine that goes beyond this theoretical limit. In other words, according to the Betz's law, no turbine can capture more than 16/27 ($\sim$ 59.3%) of the kinetic energy in wind.

CHATPER-3

Design of the AOC 15/50 Rotor Blade

A collaboration between National Renewable Energy Laboratory (NREL) and Airfoils Inc. in 1984 lead to the development of series of airfoils for wind turbine generators with aid of Eppler Airfoil Design and Analysis. These airfoil series met the requirement of stall regulation, variable pitch and rpm of wind turbine generators. The 25 airfoils so designed were represented with range from S801 to S828, and were segregated into root, primary and tip airfoil sections. Except for the root airfoil all others were designed to achieve maximum coefficient of lift with insensitiveness to roughness effect with direct proportion to the moment coefficient.

A family of thick airfoils, the S819, S820, and S821 form the three airfoil sections of the AOC 15/50 HAWT blade. These three airfoil sections designated as primary, tip, and root, correspond to the 75%, 95%, and 40% blade radial stations respectively.

The primary airfoil is designated the S819, the tip airfoil as S820, and the root airfoil as S821. Both the tip and root airfoils were derived from the S819 airfoil to increase the aerodynamic and geometric compatibilities of the three airfoils. These shapes and their aerodynamic characteristics are discussed in Tangler and Somers (1996, 2005) [19] [20], Lissaman (1994) [21]. The respective airfoil co-ordinates and the shapes are shown in Appendix D.

3.1 Blade Design in ANSYS® DesignModeler

At each station along the length of the blade, the airfoil shapes are the same as that for the AOC 15/50 wood-epoxy blade (Figure 14)used in the test configuration [22], which has a length of 7.5 m (≈ 295 in). The root of the AOC 15/50 blade starts at the hub-blade connection, at a radius 11 inches from the center of the hub. At the root end of the blade, the cross-sectional shape is relatively oval and is only semi-aerodynamic. From the root region, the blade transitions from an oval shape to an aerodynamic shape at 40% of the tip radius as defined by the SERI 821 airfoil shape. Outboard from the root region, the shape transition continues span-wise to a shape is based on a SERI 819 airfoil at 75% of the tip radius and a shape that is based on a SERI 820 airfoil at 95% of the tip radius.
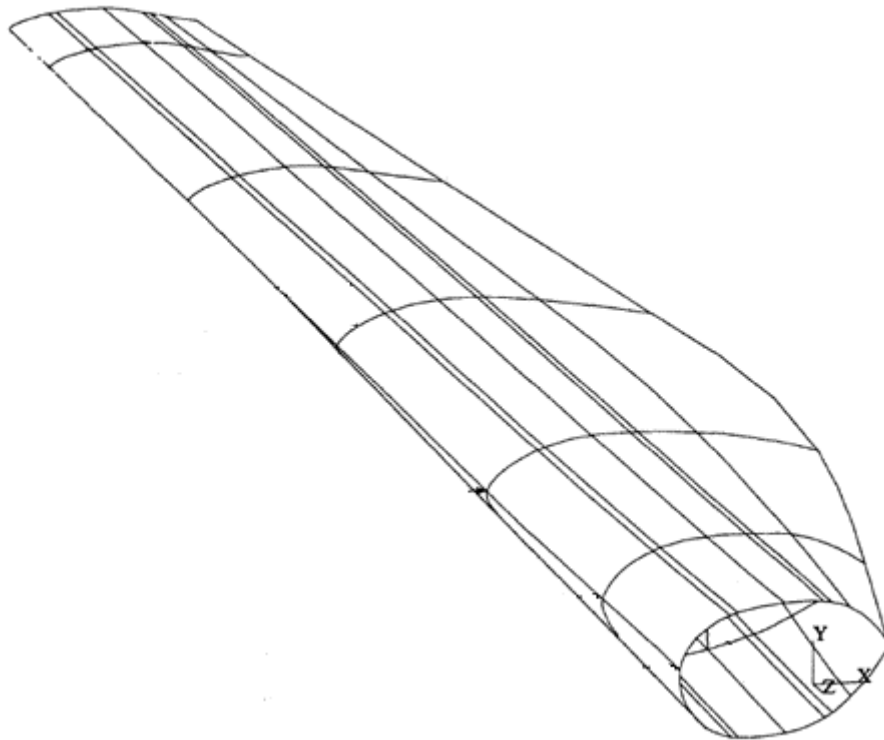
Figure 14: AOC 15/50 Blade Geometry [22]

The blade was designed in the ANSYS® DesignModeler by using the *curve* generation function to import the three different airfoil profiles (S819, S820 and S821) and then the 3-dimensional blade was modeled by using the *skin/loft* feature. Since the hub does not hold any importance in this case study, it was modeled to be a simple circular extrusion to which another two blades were duplicated at 120° angular symmetry using the *pattern* feature. The blade root section was twisted towards the feather at 1.54° and the blade tip was given a feather angle of -1.54°(away from the feather) to represent the same blade geometric features as used in the Power Performance Test Report for AOC 15/50 by NWTC and NREL [23]. Also the blade was imparted a 6° of positive (downwind wind turbine) cone angle. Figure 15, shows the chord and twist distribution along the blade length. Figures 16-19 shows the various views of the blade model.
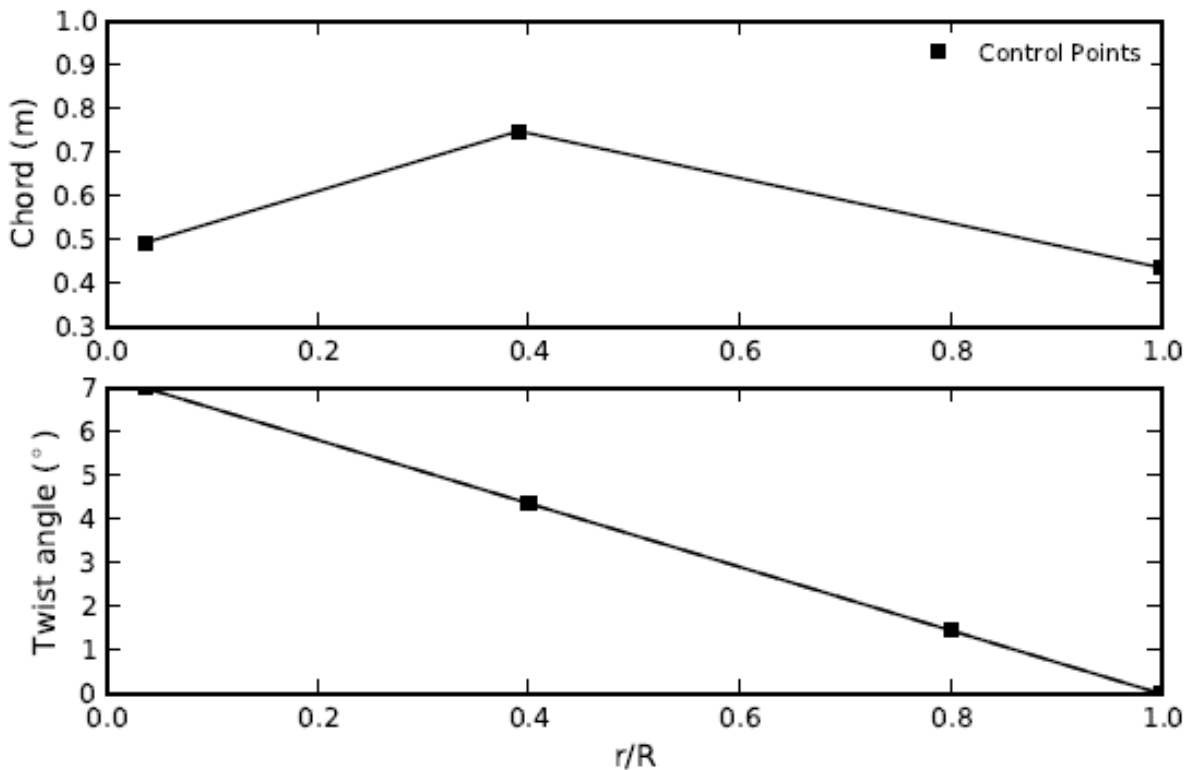
Figure 15: Chord and Twist Distributions of AOC 15/50 Wind Turbine Blade
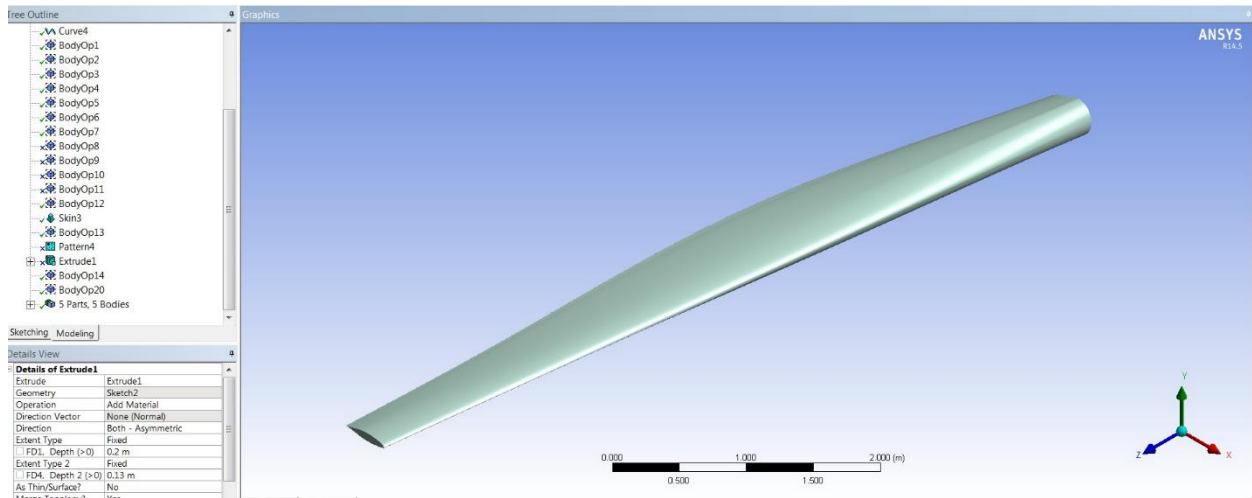
Figure 16: AOC 15/50 Turbine Blade Model in ANSYS® DesignModeler
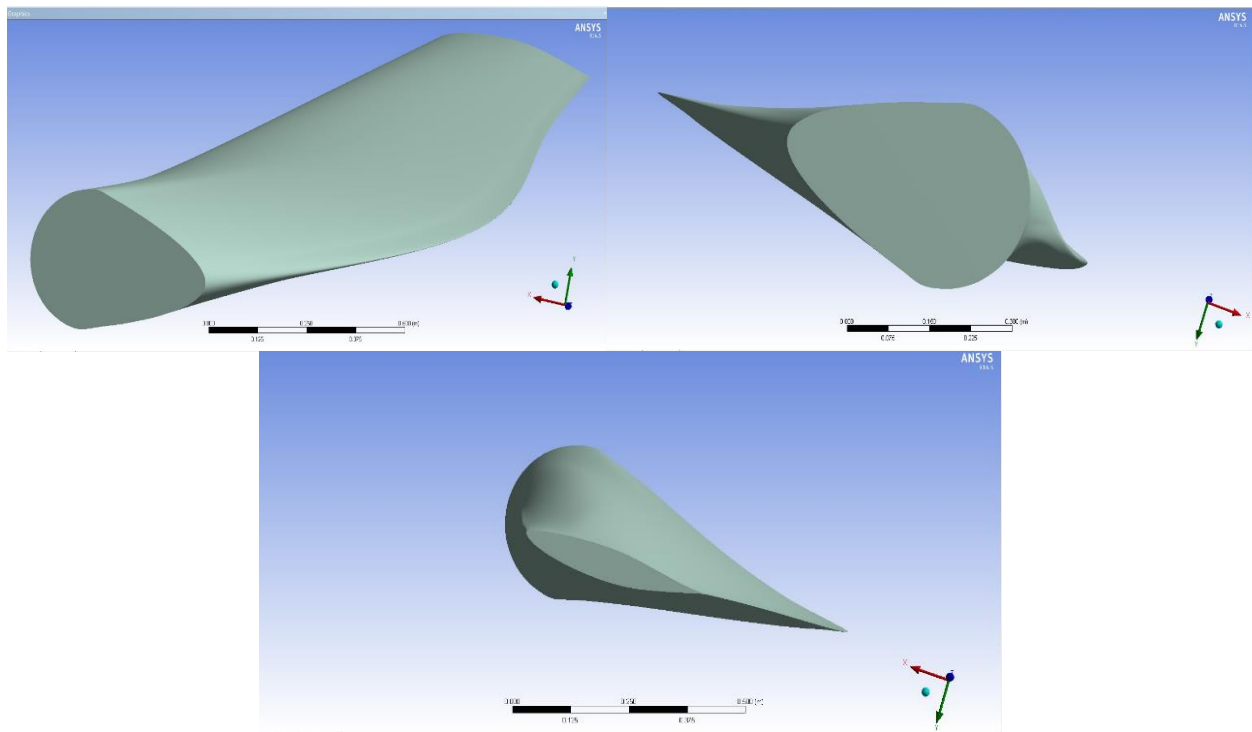
Figure 17: Various Views of the Turbine Blade Model in ANSYS® DesignModeler
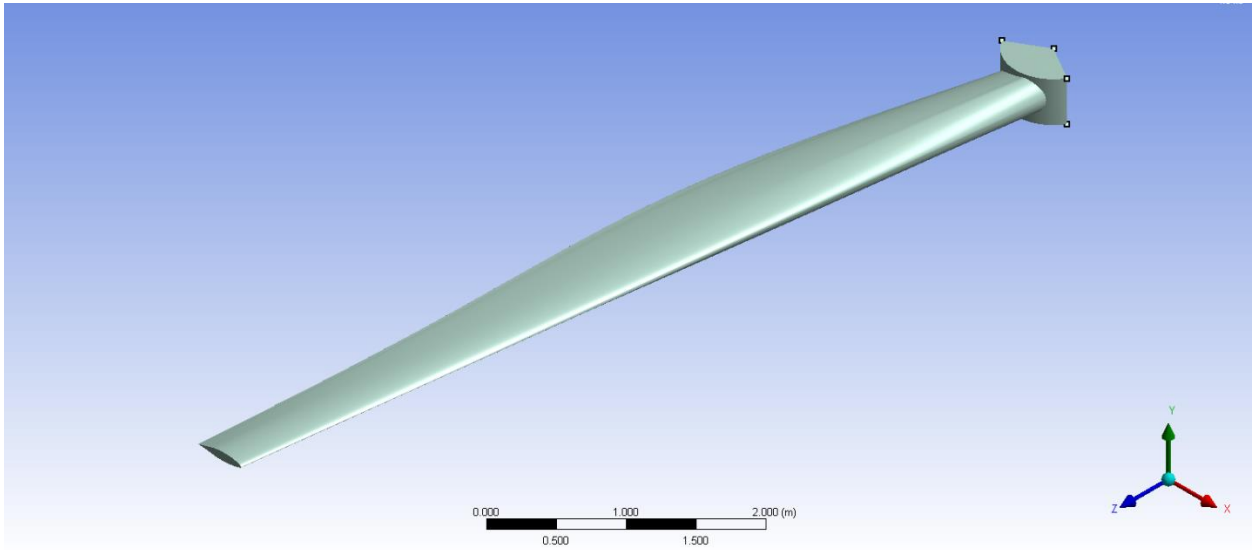
Figure 18: Turbine Blade with 120º Wedged Circular Hub in ANSYS® DesignModeler
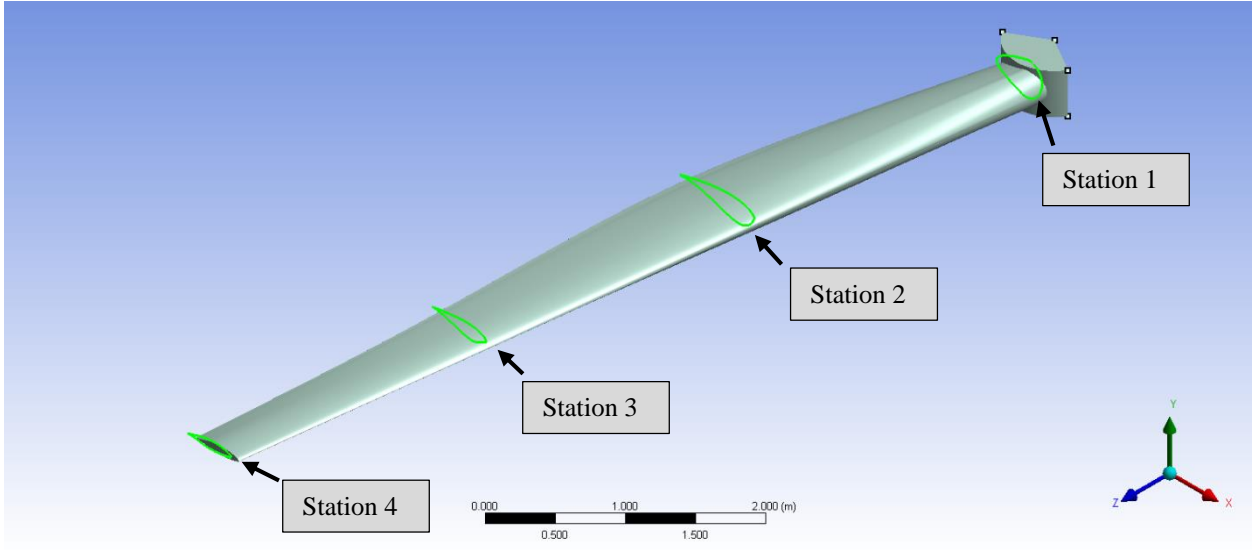
Figure 19: Turbine Blade Showing Various Radial Stations in ANSYS® DesignModeler

CHAPTER-4

Computational Fluid Dynamics Analysis Methodology

Computational fluid dynamics (CFD) deals with the solving the differential equations that govern the physical fluid flow using approximate numerical schemes. Generally in CFD modality, with sufficient grid refinement and detailed modelling, the solution of the flow problem as a whole can be approximated by solving discretized governing flow equations that reasonably and most accurately represent real flow conditions, with some underlying assumptions used to derive the model equations in a simplified manner. (i.e., neglecting complex flow phenomenon like incompressibility, flow mixing across shear layers, rotational effect of vortices, etc.).

One of the earliest uses of CFD in the context of wind turbine analysis was in the prediction of two-dimensional airfoil properties by establishing the flow around the airfoils with appreciable accuracy. However, with advancement in computing power it has progressed to capture flow at all scales, ranging from the airfoil boundary layer effects to the atmospheric boundary layer occurrences. The unexplained nature of turbulent flows is such that their exact solution is simply impossible, especially at high Reynolds number where viscous effects become prominent. Furthermore, in most cases with simplification of the computational model, the effects of turbulence on the mean flow can be solved with a decent accuracy. With high power computing (HPC) now becoming readily available, the use of high fidelity turbulence models like large eddy simulation (LES) for wind energy applications is increasing. But the prevalent general trend in the wind energy research is majorly based on the incompressible Reynolds-Averaged Navier-Stokes (RANS) equations derived from the principles of conservation of mass and momentum.

4.1 Literature Survey of Related Work and Discussion

Analysis of wind turbine blades and their performance involves considerable effort and resources. Moreover, it is challenging to experimentally measure and record a detailed span-wise distribution of aerodynamic characteristics even during in situ testing. It is equally difficult to measure any such data on a full size turbine blade because very few wind tunnels worldwide are capable of housing such large multi-megawatt machines. Analyzing turbine performance computationally is more practical, however it can be computationally expensive as well.

NREL has conducted wind tunnel experiments in real time to measure wind turbine performance. The wind tunnel testing of NREL Phase VI rotor, is of utmost importance to wind turbine researchers. The NREL Phase VI rotor was tested at the NASA Ames Research Center, inside an 80'x120' wind tunnel located at the center premises. Various aerodynamic measurements were recorded and documented [24], including the power generated by the Phase VI rotor. As an alternative approach to the computationally expensive CFD codes used for blade performance prediction, Dr. Michael Selig of University of Illinois at Urbana-Champaign, Applied Aerodynamics Group has developed a numerical code called PROPID [25], which uses blade element momentum theory (BEMT) and pre-computed empirical airfoil data, to compute a flow solution around a wind turbine blade.

The following paragraphs review and discuss various CFD based approaches in the wind energy research for studying the wind turbine blade aerodynamics and power prediction.

4.1.1 Literature Survey of Wind Turbine CFD

The efforts put into designing the two-dimensional airfoils for specific use by wind turbines have been spearheaded by three agencies, namely; NREL, TUDelft and Riso DTU. Analytical tools like XFoil and Eppler codes have extensively been used for performance studies and optimization on the two-dimensional airfoils. CFD analysis not only gives a deeper insight into the flow field around them at different operating conditions, that wind tunnel testing cannot readily produce but also can exclusively be employed as a validation tool to assess aerodynamic characteristics of the airfoils.

Two-dimensional CFD methods for aerodynamic analysis of NREL S809 airfoil used for the NREL Phase VI rotor were discussed by Yang [26] and Wolfe, Ochs [27]. Fuglsang [28] and Bertagnolio [29] also used similar two-dimensional CFD approach for the aerodynamic analysis on the family of airfoil profiles designed by Risø DTU. The aforementioned CFD methods solve the compressible RANS equations and the turbulence closure is effected by using the one equation Spalart Allmaras Model or the two equation models like $k - \epsilon$, $k - \omega$ or $k - \omega$ SST models that are very popular in the wind turbine CFD research community.

The major challenges in the two-dimensional airfoil CFD analysis, especially occur in the stall operation region as described by Rumsey, Ying [30] in their paper. The most important of all is modeling the transition to turbulence flow regime in the boundary layer, as inaccurate modelling significantly affects airfoil performance prediction. According to Mayda, Dam [31], HAWT airfoils are sensitive to Reynolds number in this range order of 10^6, with the development of unsteadiness and laminar separation bubbles in the stall regimes.

Most of the documented work on three-dimensional wind turbine blade analysis is on the NREL Phase VI rotor since the experimental results and data for the NREL Phase VI rotor are made available in the public domain by NREL and NWTC. Myriad of CFD works are extensions of the previous research work by numerous authors on the NREL Phase VI rotor.

One of the very first wind turbine CFD simulations were carried out by Sorensen, Hansen [32] using a rotating reference frame and the *k-ω SST* model. The rotor power thus predicted had a good agreement for wind speeds below 10 m/s, with power being under predicted at higher wind speeds. The partially separated flow on the blade at higher wind speeds is also not correctly captured. This mismatch was attributed to insufficient mesh resolution and limitations of the turbulence model used for the flow modelling.

Another work in the wind turbine CFD is by Duque [33], using the one equation Baldwin–Lomax turbulence model for the compressible Navier–Stokes equations. The pressure distributions along the blade span showed good agreement with the experimental results of the NREL phase II rotor, but the rotor–tower interaction was not well predicted by this turbulence model. In his later work [34], the same turbulence model was used to establish the flow around the NREL phase VI rotor, which showed good agreement of the power prediction with the experimental data even in the stalled and cross flow regions.

Le Pape, Lecanu [35] have also used a compressible CFD formulation, developed at ONERA (French Aeronautics, Space and Defense Research Lab) to study rotating wind turbine aerodynamics for the NREL phase VI rotor. Their research also outlines the relative advantages of the *k−ω-SST* turbulence model over the *k−ω* turbulence model.

Investigation on the influence of blade tip vortices on the velocity at the rotor plane using the $k-\omega$ turbulence model was conducted by Zahle and Sorensen [36]. Important work on transition modeling on the rotor blade was also done by Sorensen using the $k-\omega$ and the Langtry–Menter transition model. This research showed that the transitional computations lead to better agreement with experimental results than fully turbulent conditions.

Another important work by Laursen [37] cited the comparison with the same turbulence and transition models. This work revealed that the application of transition model leads to a more realistic performance of the blade with the basic augmentation of aerodynamic performance caused by increased lift and lowered drag.

From the above discussion it is quite evident that $k-\omega\text{-}SST$ turbulence model has been widely used and accepted as the best model to be used for CFD analysis of a wind turbine, hence the same will be used in this thesis for the flow solver setting.

Limitations of the CFD Approach for Wind Turbine Modelling

It is well understood by various experimental and CFD studies that the performance of a real wind turbine working in situ varies drastically from the wind tunnel experimental results, mainly due to the various atmospheric phenomena present intrinsically at the turbine site location. Wind turbines operate in a complex external flow field characterized by factors including; incoming turbulence, wind shear, tower shadow effects, yaw, upstream and downstream wakes. Accurately modeling of both the mean flow over the turbine blades and the flow in the near and far wake in the downstream of the wind turbine requires massive computational resources, due to the unsteady and turbulent character of the upstream and downstream flow. While the incoming

turbulent flow on the turbine is marked by an atmospheric boundary layer profile [38], the flow field around the blades exhibits scales that range from the size of small eddies in the boundary layer on the blade to as big as the blade itself. In the early CFD stages of wind turbines, uniform inflow velocity profiles were imposed, until the works of Sorenson and Huberson [39] illustrated the pronounced effect presence of the shear inflow profile (boundary layer) has on the flow-field behind the rotor. Simulating the turbulence in the flow accurately and preventing artificial diffusion is an ongoing challenge among the wind turbine community. In the paradigm of CFD modelling, the rotation of the rotor blades also leads to severe problems in constructing a computational grid. Other sources of turbulence are formed by the tip vortices, turbulent boundary layers leaving the blades, the presence of the nacelle as an obstruction to the flow leaving the blades, all of which account for the mechanical turbulence.

Furthermore, it is worthwhile to mention here that CFD methods for wind turbines, despite advanced discretization techniques coupled with high-order schemes to handle various flow scales, the accurate modeling of the inflow turbulence, the associated wake, its viscous and turbulent diffusion in the downstream regions are a particularly difficult problem due to numerical diffusion and due to the difficulty in identifying appropriate turbulence models. Wind turbulence intensity is one of the most complicated parameters to computationally model in wind turbine performance investigation and its value plays an important role in CFD simulations of wind turbines. The turbulence intensity along with the type of terrain, month of the year, and even day-night time effect become very influential for predicting power curves and the energy production of a wind turbine [40] [41].

4.1.2 Literature Survey on Wind Turbine Optimization Using CFD

The literature survey conducted in the Hunt Library at the Embry-Riddle Aeronautical University, Daytona Beach campus revealed two important thesis research works in the field of HAWT design optimization. It would not be out of context to mention both of them in this section. The two dissertations are titled as below:

[42] Naishadh G. Vasjaliya, *"Fluid-Structure Interaction and Multidisciplinary Design Analysis Optimization of Composite Wind Turbine Blade"*, ERAU Library, Thesis Section, August 2013.

[43] Tsewang Rabga Shrestha, *"3D Aerodynamic Optimization of NREL VI Wind Turbine Blade for Increased Power Output and Visualization of Flow Characteristics"*, ERAU Library, Thesis Section, April 2014.

Parametric Model of the Blade

In both the aforementioned research works, the HAWT blade geometry is parameterized in a two dimensional X-Y plane using two design variables; chord length and respective twist of the airfoil sections at various radial locations along the blade span. This approach does not put any limiting constraints on the blade length (span) in the Z direction and consequently makes the optimization formulation unconstrained in the Z-direction (along the blade span). This adds to the uncertainty of the overall system and the effect of the blade length on the objective function (power output) cannot be fully ascertained.

The present work uses an additional design variable, the sectional radius (r/R) for the various airfoil sections from which the complete blade is lofted. This ensures that the blade shape is fully parameterized in the global three dimensional co-ordinate system using Non-Uniform Rational B-Splines (NURBS) for modeling curves and surfaces along the blade span.

Sensitivity Analysis

While the previous research works ilucidate a *qualitative* measure of how the shape design paramaters are related to the objective funtion (power output), they do not encapsulate the *quantitative* measure of the dependence and variation *(what-if scenario)* of the same. The tools in Figures 37-40, like *Determination Histogram* and *Sensitivity Chart* used in present thesis allows one to see which inputs predominantly drive a selected output parameter (torque). This has reduced the optimization problem with only most sensitive input parameters as design variables, thereby decreasing the design space to be searched for optimum solution to the design problem. Additionally, the graphs of objective function (power output) plotted as a function of various input design parameters in Appendix C demonstrate the quantitative variation of input and output functions. These plots give a better understanding of *what* changes occur in the objective function and by *how much*, *if* the input parameters are varied one at a time, keeping the other input parameters constant.

Optimization Methodology and Predictive Capability Measure

The accuracy of optimization routines based on any GBOM, probabilistic or surrogate models is often debatable and the aforementioned research papers do not discuss the predictive

capability or robustness of the same. In the context of an RSM routine used in this research, the main measures of predictive capability; *root mean square error (RMS $_{adj}$)* and *coefficient of multiple determination (R $^2_{adj}$)* are recorded, plotted and validated by verification with the flow solver ANSYS® Fluent®. The what-if scenario graphs plotted are also in good agreement with the optimization results obtained. The *coefficient of determination* is 0.97069 and the *root mean square error is* 2.2129 as seen from Figure 50. Since the computed values from the generated response surface are in a close proximity to the best values, the response surface thus generated can be expected to predict a fairly good trend for the objective function value. In other words, the model represented by the response surface would predict the objective value (torque) within an error of (+ or -) 3.532%.

4.2 Flowchart of Computational Approach for HAWT Performance Study and Optimization

PRELIMINARY DESIGN & ANALYSIS

Airfoil Sections (S819, S820 & S821)
(Software Used: ANSYS® DesignModeler)

↓

Grid Generation on the Airfoil Sections
(Software Used: ANSYS® Meshing)

↓

k-ω SST Turbulence Model on the Airfoil Sections
(Software Used: ANSYS® Fluent)

↓

Validation of the CFD Results for the Airfoil Sections

COMPUTATIONAL FLUID DYNAMICS (CFD)

Blade Design
(Software Used: ANSYS® DesignModeler)

↓

Grid Generation on Turbine Blade Flow Domain
(Software Used: ANSYS® Meshing)

↓

k-ω SST Turbulence Model on Turbine Blade
(Software Used: ANSYS® Fluent)

PARAMETRIC STUDY AND OPTIMIZATION

Parametric Correlation/Sensitivity Study

↓

Building the Response Surface

↓

Optimization Using NLPQL

4.3 CFD Analysis of the Airfoils (S819, S820 and S821)

A fluid flow analysis using the commercial flow solver ANSYS® Fluent is carried out on the family of thick airfoil sections S819, S820 and S821 comprising the turbine blade. The primary airfoil is designated the S819, the tip airfoil is S820, and the root airfoil, the S821. The purpose of the 2-dimensional airfoil flow analysis is to compare the results with the available experimental datasheet of each airfoil, and to predict and validate the best turbulence model in the ANSYS® Fluent flow solver that can be extended to the flow analysis of a full 3-dimensional turbine rotor.

4.3.1 Computational Domain (Grid) for the Airfoils

The meshing is performed in the ANSYS® Meshing module after importing the respective airfoil geometry and creating a flow domain around the airfoil cross section by using the *boolean* feature for the volume extraction. The conventional C-grid topology mesh is used as the computational domain around the airfoil which extends to 15 chord length in the upstream direction and 20 chord length in the downstream direction, as measured from the airfoil leading edge. The grid thus obtained is a structured grid with a grid growth rate of 1.20. The overall mesh is fine with a maximum skewness of 0.695. The grid points are clustered in the proximity and the wake region of the airfoil to capture the flow physics accurately as shown in Figures 20-22.

The boundary conditions for the computational domain are set:

a) Velocity Inlet – The curved surface of the C-Grid is set to the *velocity inlet* condition as the free stream velocity to be simulated in the computational domain is known beforehand.

b) Wall – The airfoil upper and lower surfaces are selected as *wall* condition.

c) Symmetry – The edges of the computational domain on either side of the airfoil surface are selected to be the *symmetry* type. This just means that these boundaries do not affect the flow in any possible way.

d) Pressure Outlet – The edge of the computational domain downstream from the airfoil is set to a pressure outlet condition. This gives a better prediction of the exit pressure distribution and thus results in better accuracy of the overall solution.
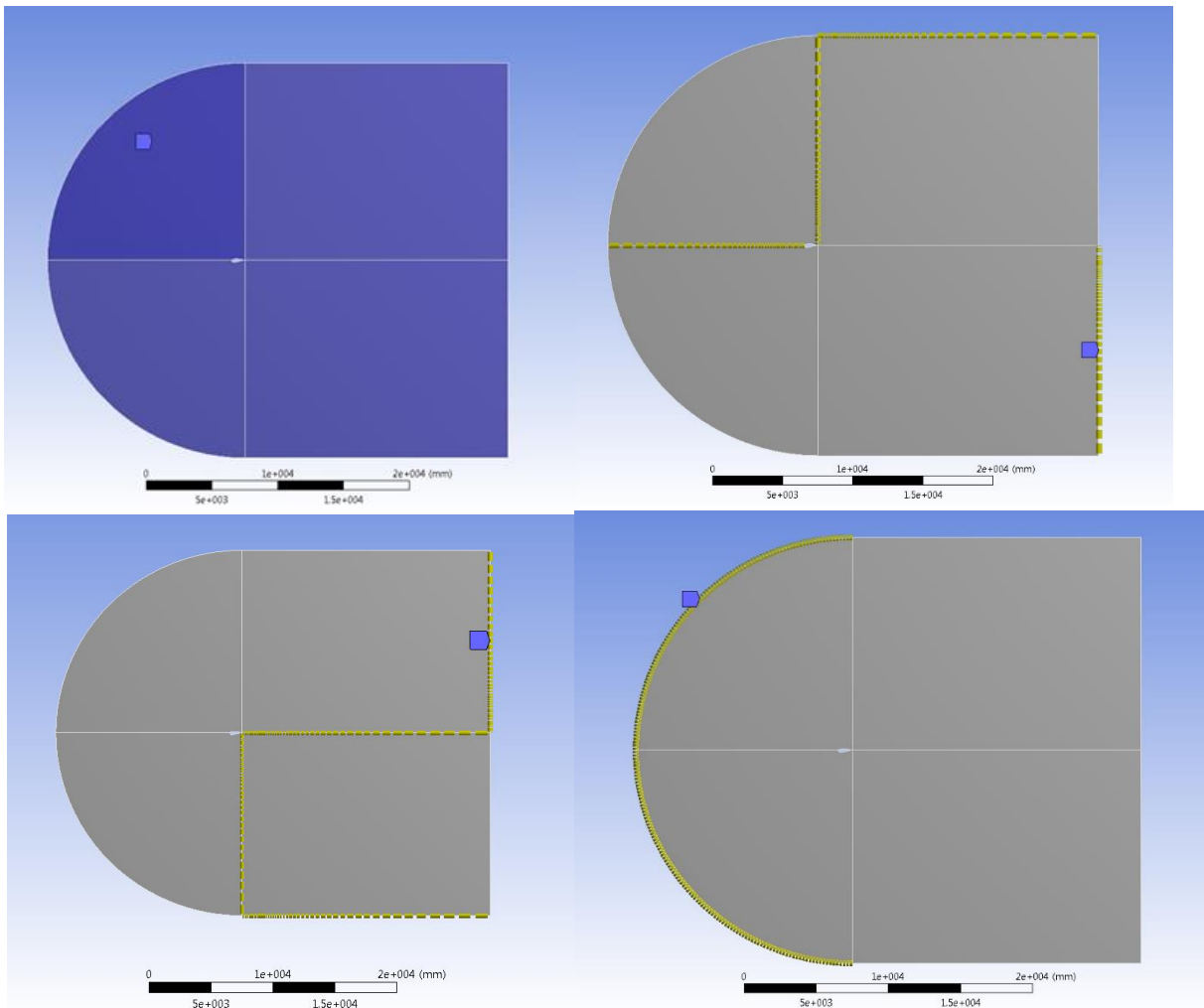
Figure 20: Schematic of Grid Sizing and Biasing for Airfoils
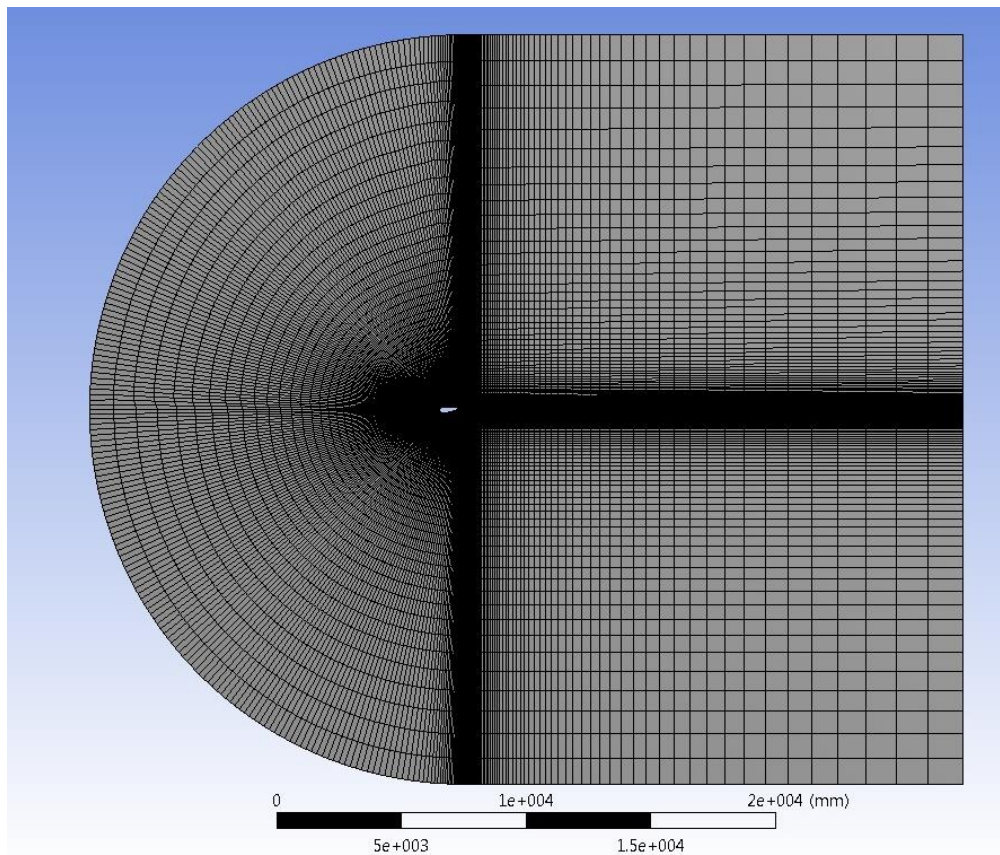
Figure 21: Far Field Grid for Airfoils
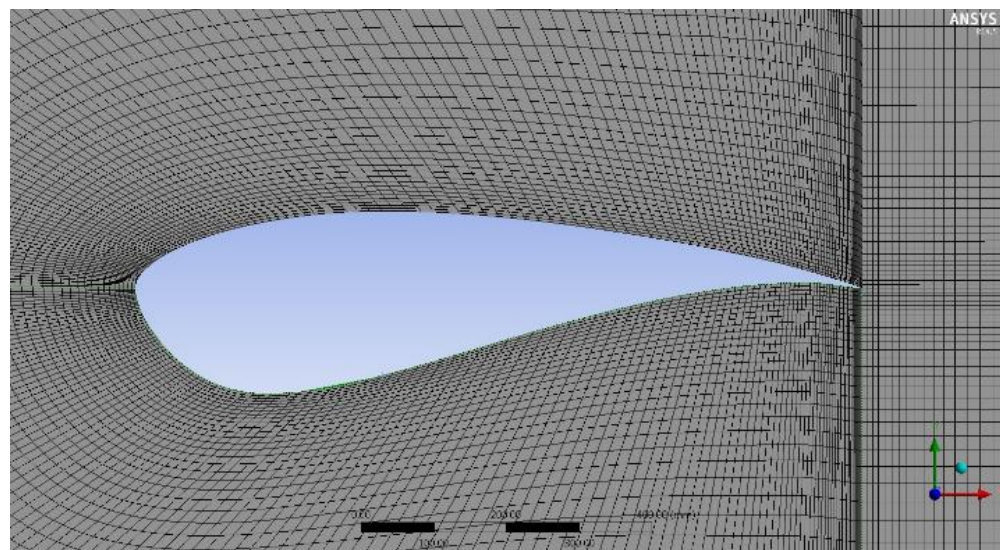
Figure 22: Near Field Grid for Airfoils

4.3.2 Flow Simulation over Airfoils

Simulations were performed with the commercial software ANSYS® Fluent, using a RANS model. A pressure based compressible flow solver with k-ω SST turbulence model was used for the flow simulation. Convergence was monitored looking at the lift and drag coefficients time histories. Also the residual tolerance of 10^{-6} was reached for all velocity and energy terms to ascertain the robustness of the obtained flow parameters. Furthermore, the difference in the mass flow at the inlet and the outlet of the computational domain showed a negligible error (order 10^{-6}). All the above three conditions were satisfied as per the best practices [44] to be followed in ANSYS® Fluent for obtaining an accurate and converged solution.

Table 1: Table of CFD Solver Settings for Airfoils

Airfoils	SERI 819, SERI 820 and SERI 821
Solver	Pressure-based
Velocity Formulation	Absolute
Time	Steady
Turbulence Model	k-ω SST
Fluid	Air at STP
Velocity	8.03 m/s
Pressure-Velocity Coupling Scheme	SIMPLE
Spatial Discretization & Interpolation Scheme	Gradient: Least Squares Cell Based Pressure: STANDARD Momentum: Second Order Upwind Turbulent Kinetic Energy: Second Order Upwind Specific Dissipation Rate: Second Order Upwind

The k-ω SST Turbulence Model

Menter's [45] *k-ω* SST turbulence model is a two equation model. One flow equation to be solved is for the kinetic turbulent energy *k*, while the second equation is for the specific turbulent dissipation rate *ω*. This is a robust eddy-viscosity turbulence model widely used in CFD, combining the k-omega turbulence model and k-epsilon turbulence model such that the k-omega is used in the inner region of the boundary layer and switches to the k-epilson in the free shear flow. The foundation and formulation of the *k-ω* SST model is based on physical experiments and attempts to predict solutions to typical engineering problems. The concept of Reynolds averaged eddy-viscosity is a pseudo-force and is not physically present in the system on which the CFD analysis is being conducted.

Results for Flow Simulation over Airfoils

The aerodynamic performance of airfoil sections can be studied by the distribution of pressure over the airfoil pressure and suction surface. This distribution is usually expressed in terms of the pressure coefficient:

$$C_p = \frac{P - P_0}{\frac{1}{2}\,\rho\,v_0^2}$$

(7)

C_p is expressed as the difference between local static pressure and freestream static pressure, non-dimensionalized using the free-stream dynamic pressure. Computational results from the above flow simulation for SERI 819, SERI 820 and SERI 821and experimental data from "The S819, S820, and S821 Airfoils" by D.M. Somers [19], were used for validation. There is very good

agreement between the C_p values predicted by ANSYS® Fluent and the experimental data. These are plotted in Figures 23, 24 & 25 as shown below. The discrepancies in the plots near the trailing edge of the airfoils sections are due to the modelling imperfections due to airfoil co-ordinates importing error. Also it can be attributed to the highly skewed cells present in the grid due to the sharp trailing edge of the various airfoil sections. It would not be out of the context here to state that this error could also be possible due to the difference in the manufactured trailing edge radius of the various airfoil sections used in the real time wind tunnel testing of the three airfoil sections as compared to the CAD model used in the computational study.
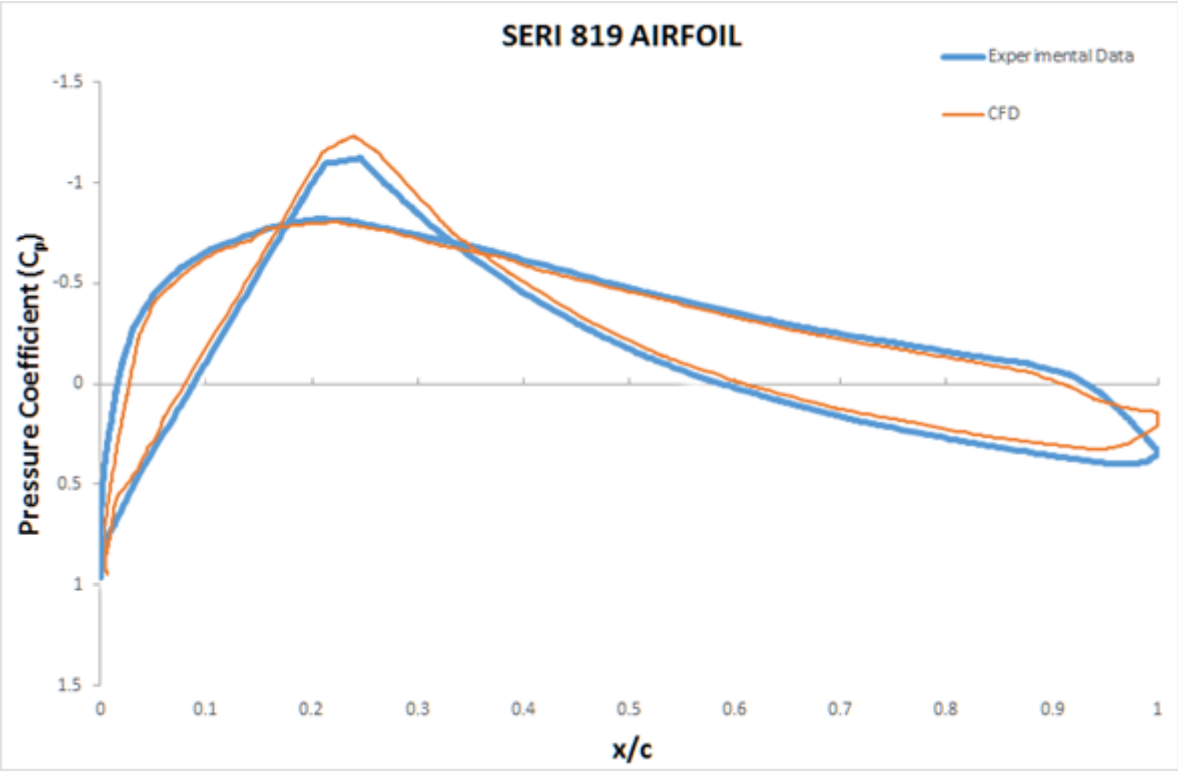
Figure 23: C_p Plot for S819 Airfoil
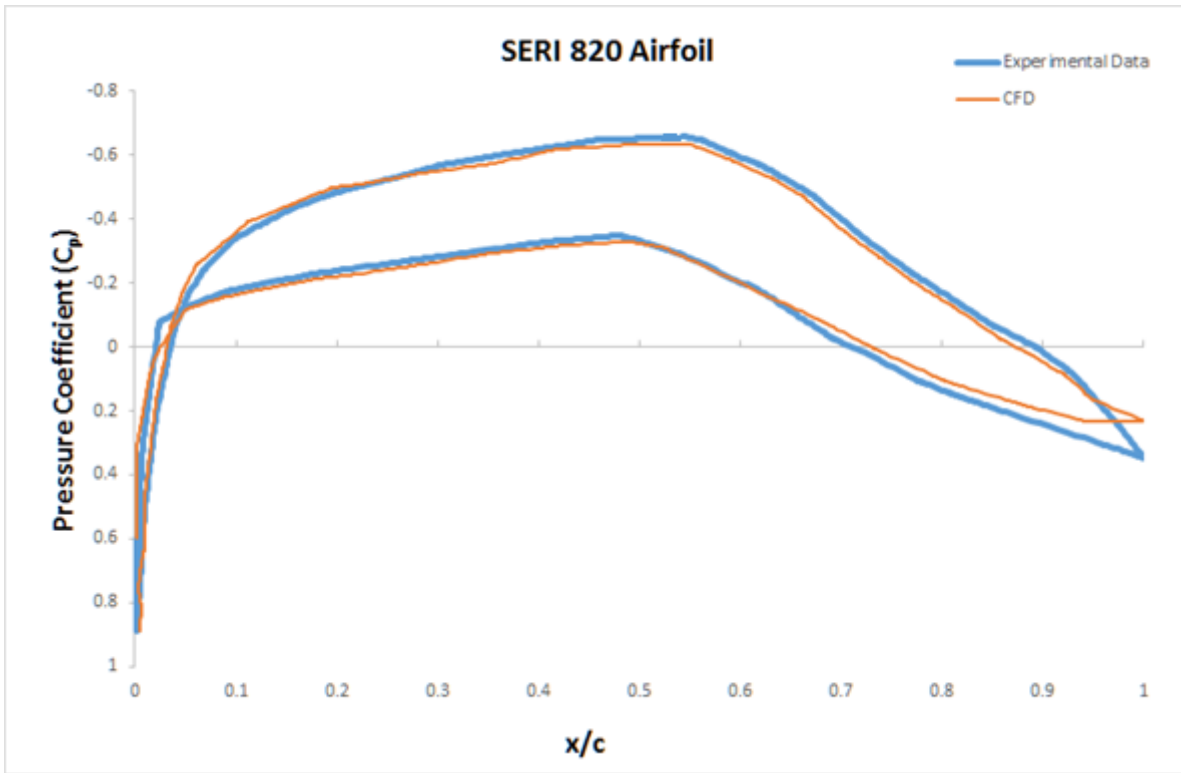
Figure 24: C_p Plot for S820 Airfoil
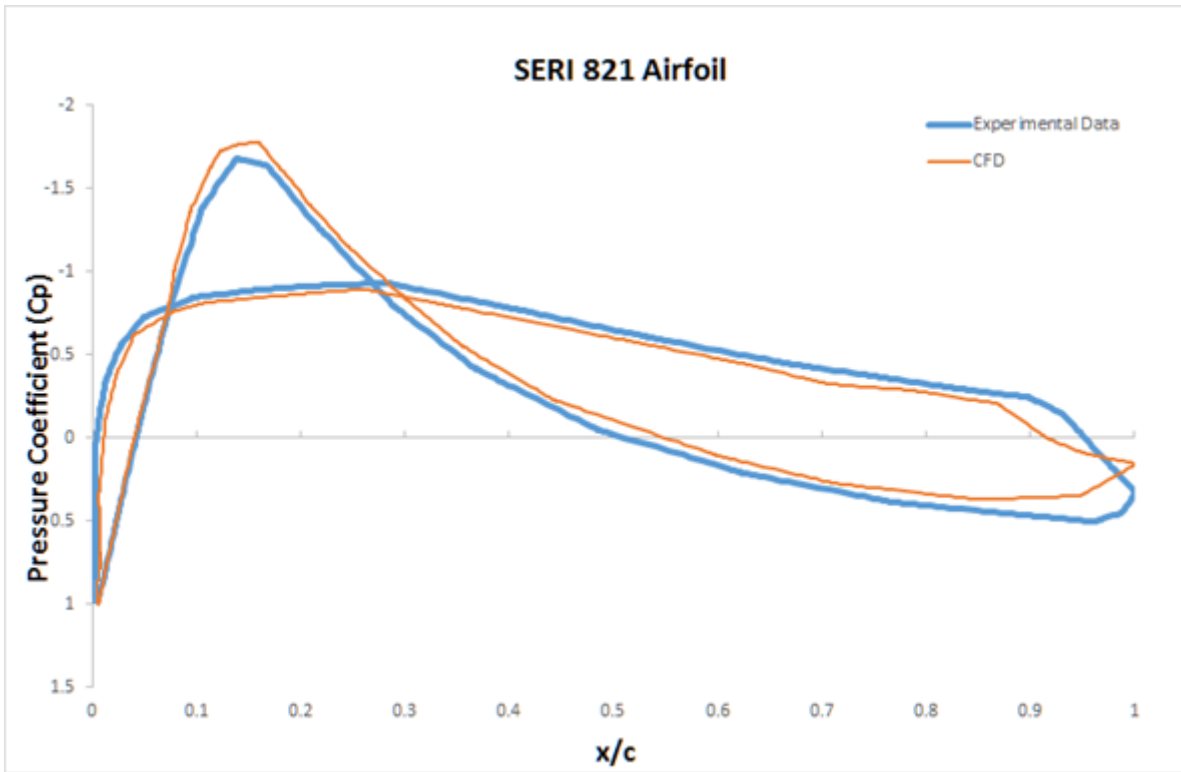
Figure 25: C_p Plot for S821 Airfoil

4.4 CFD Analysis on the AOC 15/50 HAWT Blade

Physical flow analysis of turbine rotor blades using wind tunnel would be possible for small scale rotors, but the increase in diameters has called for the use of computational fluid dynamics for fluid flow over blades and predication of loads. In this research work, a compressible Navier-Stokes (N-S) solver ANSYS® Fluent was used to predict the aerodynamics of the blade. The main aim of this research is to develop and validate a numerical methodology for predicting the torque on the AOC 15/50 HAWT blade. Simulations were performed with the commercial software ANSYS® Fluent, using a k-ω SST turbulence model.

4.4.1 CFD Domain Mesh and Numerical Model for Rotating Bodies

This subtopic gives an insight into the CFD numerical models for turbo-machinery applications. The aim of this paragraph is providing the numerical basis to perform CFD simulation of rotating bodies.

The main challenge in turbo-machinery applications is the introduction of a rotating body to apply forces on the fluid (e.g. compression or expansion). From an analytical point of view the rotation should be introduced into constitutive equations of motion, and there are mainly two approaches: the Moving Reference Frame (MRF) and the Sliding Mesh (SLM). The first one consists of rewriting N-S equations in a rotating frame, while the second one introduces rotation assigning a rotational component of velocity to all nodes of the domain (physical grid rotation). It is immediately understandable that SLM approach is more realistic that MRF, but also more CPU-demanding as the computational model needs re-meshing at every time advancement during the simulation procedure.

Since the rotation of grid intrinsically depends on time-evolution of simulation, this approach is not recommended for steady state simulations as the solution obtained is not time-dependent. In other words, a time steady calculation performed with MRF approach according to the evidence in most of the turbo-machinery problems, does not compute a time-accurate solution.

4.4.2 Moving Reference Frame Model

Moving Reference Frame (MRF) model solves the equations of motion of a steady formulation in a moving frame. For a rotating frame with constant rotational speed, it is possible to transform the equations of motion to the rotating frame such that steady-state solutions are possible. This approach is based on the assumption that in most of cases of practical interest, steady solutions are required for rotating bodies, without taking into account the unsteady details of the flow field (e.g. vortex shedding from a bluff body). On the other hand, an unsteady solution using the MRF model can also be computed to simulate the unsteady details.

Consider a coordinate system which is rotating with an angular velocity ω relative to a stationary (inertial) reference frame, as illustrated in Figure 26. The origin of the rotating system is given by a position vector r_o.
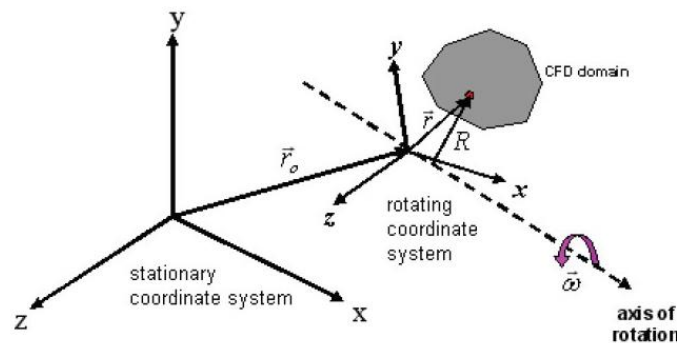

Figure 26: Rotating Body in the Inertial Reference Frame [24]

In accordance to the MRF method, the computational domain for the CFD problem can then be defined with respect to the rotating reference frame, such that an arbitrary point in the CFD domain is located by a position vector r from the origin of the rotating frame. The fluid velocities can be transformed from the stationary frame to the rotating frame using the relation,

$$v_r = v - (\omega \times r) \tag{8}$$

In the above equation, v_r is the relative velocity (the velocity as viewed from the rotating frame) while v is the absolute velocity (the velocity as viewed from the stationary frame). When the equations of motion are solved in the rotating reference frame, the acceleration of the fluid is increased by the additional terms that appear in the momentum equation. Moreover, the equations can be formulated expressing absolute or relative velocity as dependent variable of momentum equation. Constitutive N-S equations for which the solution is being calculated according to the relative velocity formulation for continuity, momentum and energy respectively are as follows:

$$
\begin{aligned}
&\frac{\partial \rho}{\partial t} + \underline{\nabla} \cdot \rho \underline{v}_r = 0 \\
&\frac{\partial}{\partial t}\left(\rho \underline{v}_r\right) + \underline{\nabla} \cdot \left(\rho \underline{v}_r \underline{v}_r\right) + \rho\left(2\underline{\omega} \times \underline{v}_r + \underline{\omega} \times \underline{\omega} \times \underline{v}_r\right) = -\underline{\nabla} p + \underline{\nabla} \cdot \underline{\underline{\tau}} + \underline{F} \\
&\frac{\partial}{\partial t}\left(\rho E_r\right) + \underline{\nabla} \cdot \left(\rho \underline{v}_r H_r\right) = \underline{\nabla} \cdot \left(k\underline{\nabla} T + \underline{\underline{\tau}} \cdot \underline{v}_r\right) + S_H
\end{aligned} \tag{9}
$$

The momentum equation formulated above contains two additional acceleration terms, the Coriolis component of acceleration $(2\,\omega \times v_r)$ and the centripetal acceleration $(\omega \times \omega \times v_r)$. In addition, viscous stress tensor does not change with respect to the MRF equation, except for the introduction of the relative velocity. Energy equation is written in the form of internal energy E_r, introducing the total enthalpy H_r of the system in consideration.

$$E_r = h - \frac{p}{\rho} + \frac{1}{2}\left(v_r{}^2 - (\omega r)^2\right) \qquad\qquad H_r = E_r - \frac{p}{\rho} \qquad\qquad (10)$$

MRF model can be applied to different zones in the domain (both rotating and nonrotating), solving RANS formulation of equations. Moreover translational or rotational periodic boundaries can be applied wherever periodic surfaces are present in the domain. For these reasons MRF model is widely used for industrial applications, being one of the most versatile and low CPU-demanding approaches for turbo-machinery simulation.

4.4.3 Computational Domain (Grid) for the Turbine Blade Model

The meshing is performed in the ANSYS® Meshing module after importing the respective blade geometry and creating a flow domain around the airfoil cross section by using the *boolean* feature for the volume extraction. The full rotor three bladed model can be reduced to a symmetric model of a single blade with a 120 degree rotational symmetry along the global Y-axis. In order to simply our CFD model and save computational resources, simulations are performed on a wedge shaped computational domain (120º periodicity) with rotational periodic boundary conditions applied to the wedged faces of the domain. It implies that the velocities going out from the left symmetry boundary can enter the right boundary on the other side in an infinite loop. It was further assumed that the flow conditions on either side of the 120º wedge are fully symmetric (Figure 27).
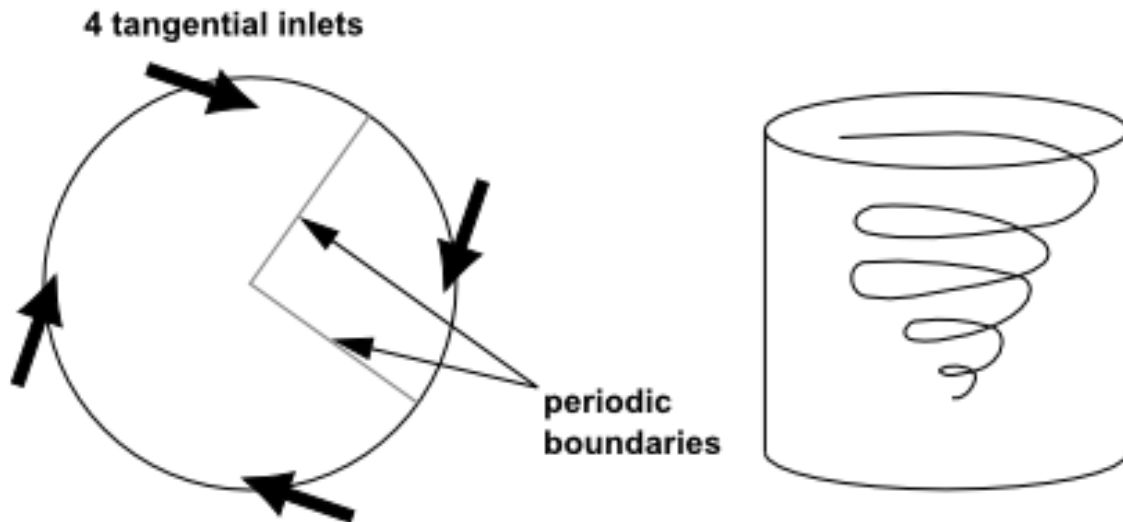
Figure 27: Periodic Boundary Conditions Representation [24]

A three dimensional model of the computational domain is shown in the Figure 28. A hybrid mesh topology is used as the computational domain around the blade which extends to 10 times the blade length in the upstream direction and 30 blade lengths in the downstream direction, as measured from the global origin. Figure 29 shows the rotational periodic boundary conditions applied to the wedged faces of the computational domain. The grid (Figure 30) thus obtained is a combination of structured grid with hexahedral elements in the far-field region and tetrahedral elements in the near-field region of the blade (Figure 31). An inflation layer of 25 structured prismatic cells stacked one on another is used to capture the boundary layer effects. The thickness of the first cell to the wall was kept at 6.3×10^{-5} m so that the y^+ value falls between 1 and 3. Patch dependent geometry controls were set for the meshing algorithm to make sure that during successive meshing iterations, the mesh grows outward from the blade surface and fully captures the geometric details of the blade. The overall mesh has a geometric grid growth rate of 1.20. A sequence of 20 smoothing iterations were carried out post meshing to repair the grid and bring down the average skewness to 0.88. The grid points are clustered in the proximity and the wake region of the blade to capture the flow physics accurately.
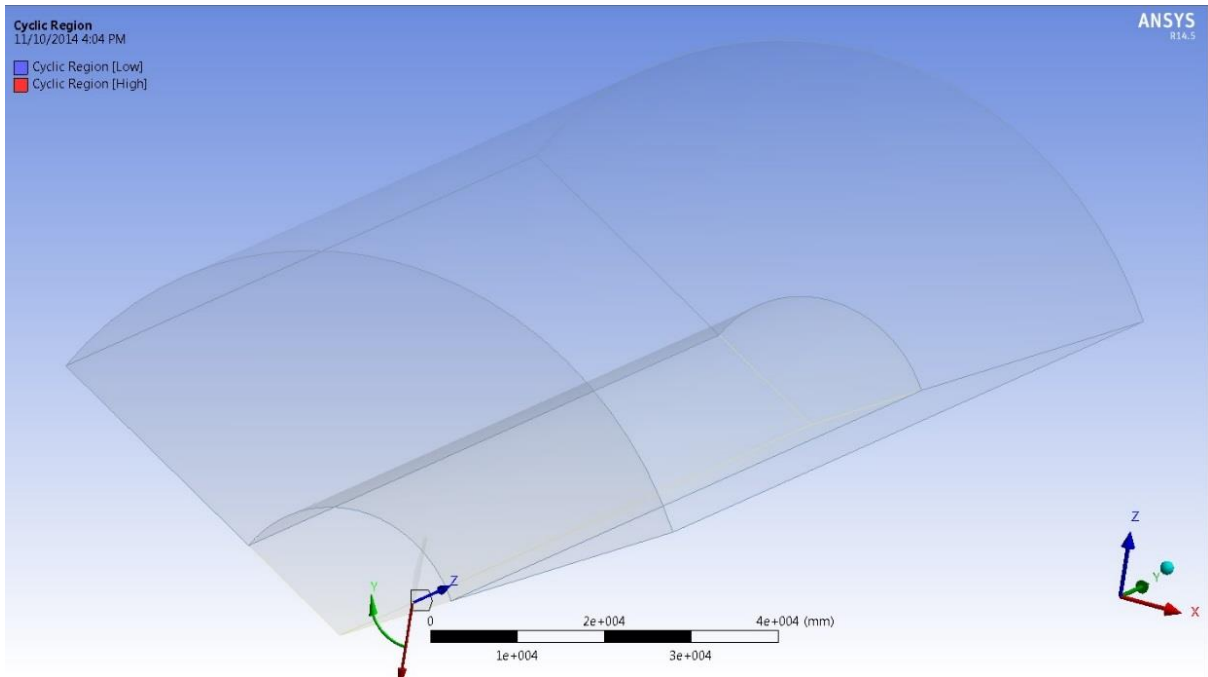
Figure 28: Full Computation Domain
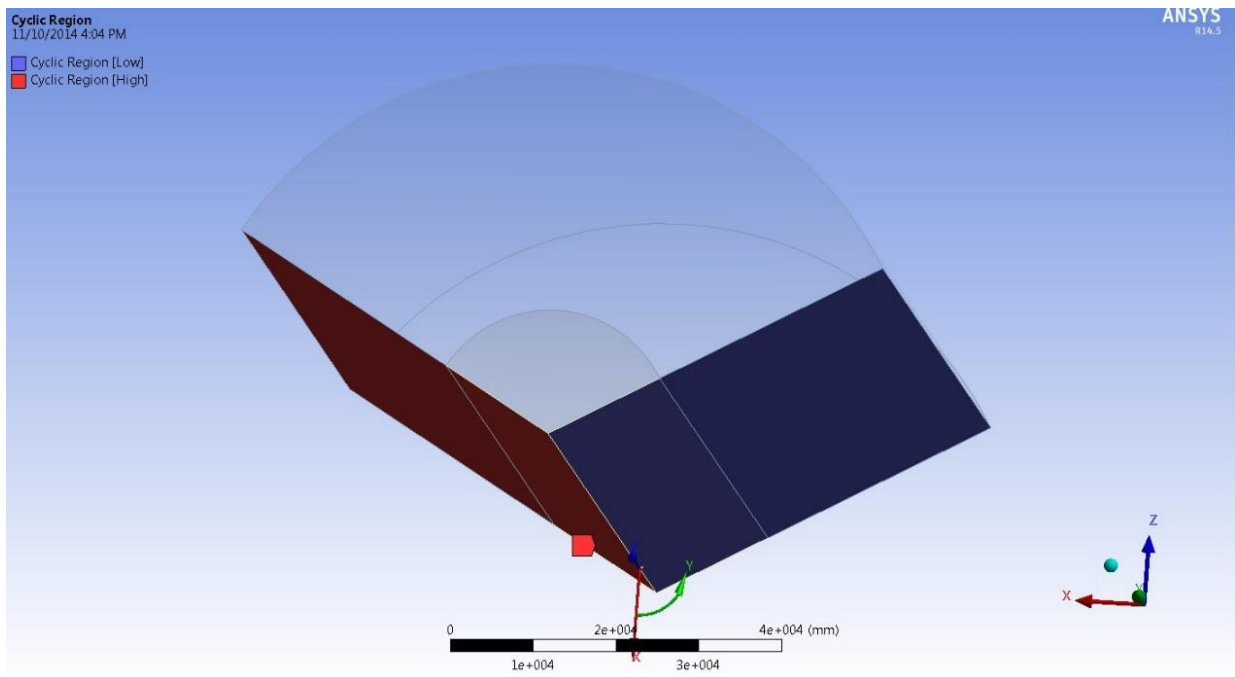
Figure 29: Periodic Boundary Setup for the Computational Domain
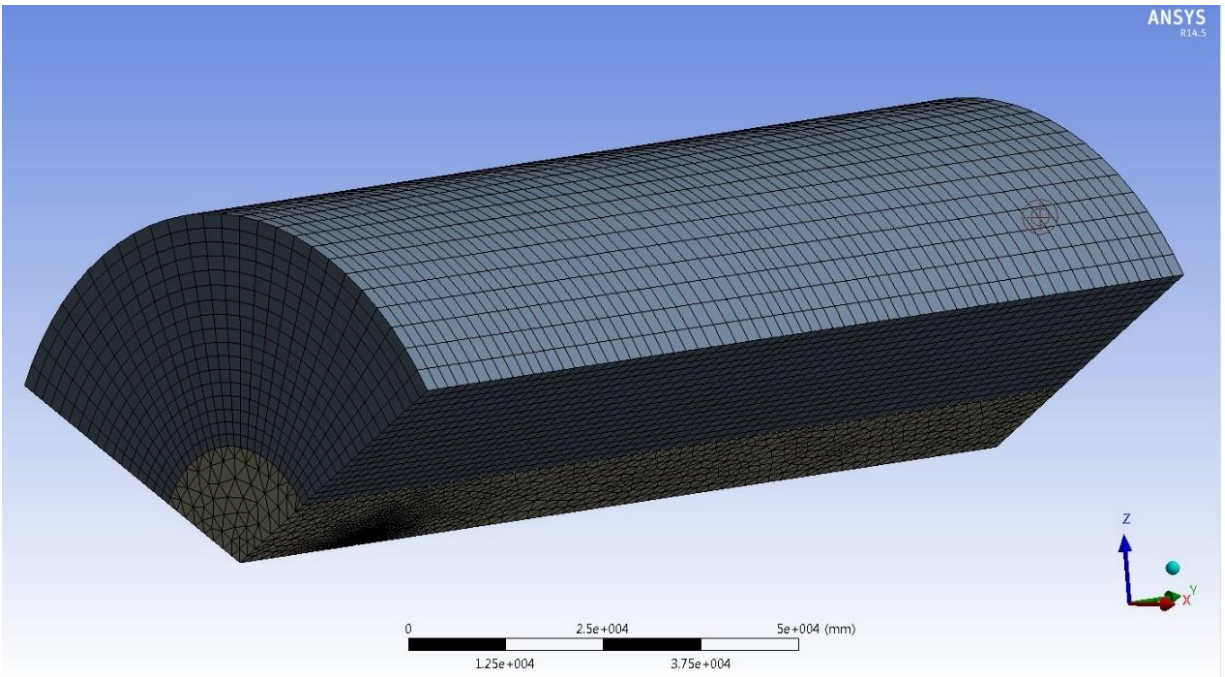
Figure 30: Far-Field Grid
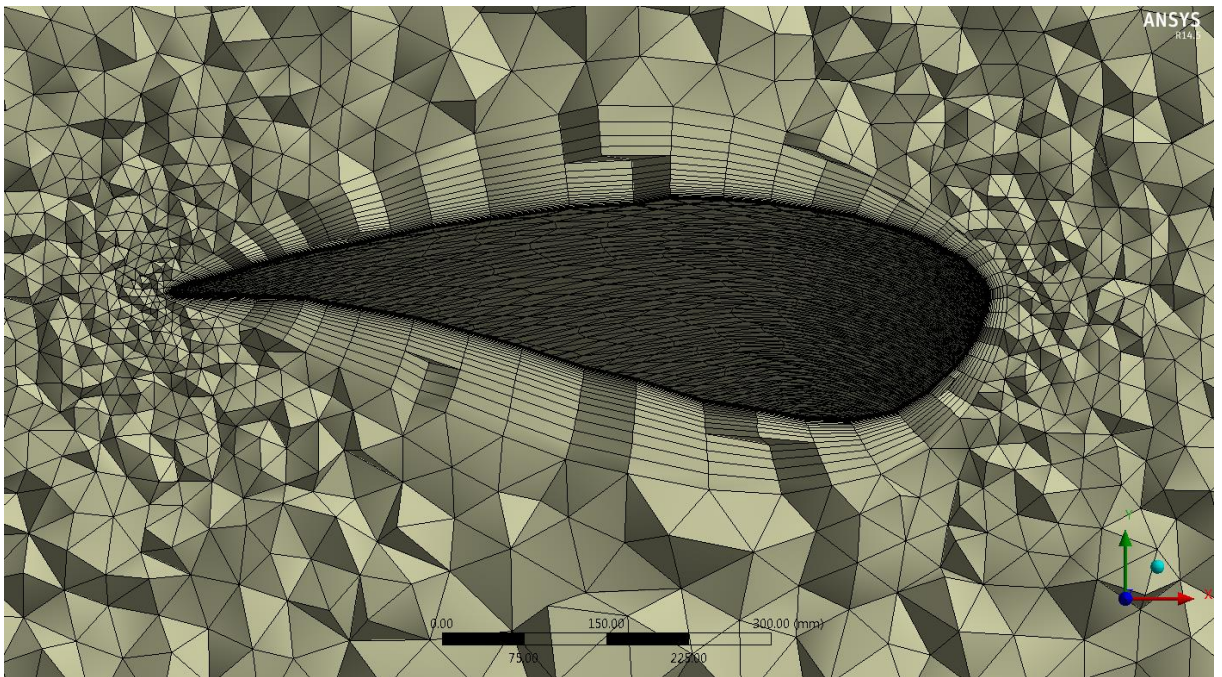
Figure 31: Near-Field Grid with Prismatic Layer

47

The boundary conditions for the computational domain are set as listed below;

a) Velocity Inlet – The upstream surface of the domain is set to the *velocity inlet* condition as the free stream velocity to be simulated in the computational domain is known beforehand.

b) Wall – The blade upper and lower surfaces are selected as *wall* with no-slip condition.

c) Periodic Boundary – The edges of the computational domain on either side of the wedge are selected to be the *periodic boundaries*. The velocities going out from the left symmetry boundary can enter the right boundary on the other side in an infinite loop.

d) Pressure Outlet – The surface of the computational domain downstream from the blade is set to a *pressure outlet* condition. This gives a better prediction of the exit pressure distribution and thus results in better accuracy of the overall solution. The pressure at the outlet was set to be atmospheric pressure.

e) Symmetry – The curved surface of the computational domain is selected to be the *symmetry* type. This just means that these boundaries do not affect the flow in any possible way.

4.4.4 Grid Independence Study

An initial grid independence study was performed in order to be sure that the flow solutions obtained in the later sensitivity analysis were consistent and independent of the grid used for discretizing the flow domain. Three grid topologies; coarse (3.9 million elements), medium (6.6 million elements) and fine (9 million elements) were used for obtaining the initial solution. The cell count was differed by clustering more prismatic cell layers near the blade surface where the boundary layer effects take place. The thickness of the first cell to the wall was kept at 6.3 x 10^{-5} m so that the y$^+$ value falls between 1 and 3. Such range of y$^+$ is suitable for the tested turbulence models. Since torque acting on the blade is of primary concern for this study, the torque on the blade was the deciding factor for finding the optimum grid for this flow problem. Medium grid quality was chosen to be the best candidate as it exhibited grid independence to the next iteration towards a finer grid, as seen from Figure 32.
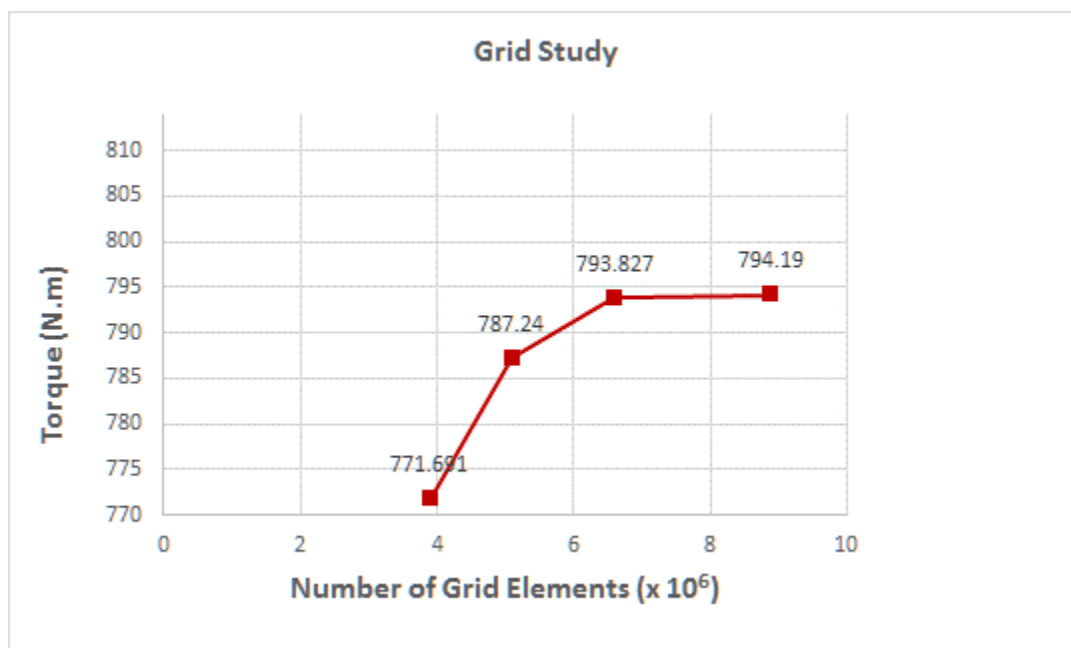

Figure 32: Plot Showing Grid Independence Study

4.4.5 Flow Simulation over the Rotor Blade

Simulations were performed with the commercial software ANSYS® Fluent, using a RANS model. A pressure based compressible flow solver with k-ω SST turbulence model was used for the flow simulation. For simplifying the computational model, the atmospheric boundary layer effects in the inflow, the near and the far wake modelling and their subsequent interactions with the mean flow were neglected in the simulations. Since the study focusses on the dependence of blade geometry on the torque produced, a uniform inflow velocity profile was modelled for all CFD simulations for parametric study and sensitivity analysis. All simulations were computed in steady state until convergence or till the end of prescribed iterations to allow developed flows in the domain. Then in order to maintain computational stability, the simulations were switched to transient solver.

Convergence was monitored looking at the thrust force time histories over different revolutions and reached in a few cycles (about 2 to 3) for all wind conditions tested. Also the residual tolerance of 10^{-6} was reached for all velocity and energy terms to ascertain the robustness of the obtained flow parameters. Furthermore, the difference in the mass flow at the inlet and the outlet of the computational domain showed a negligible error (order 10^{-6}). Additionally, a vertex point (Figure 33) was created on the symmetry axis at one blade length downstream of the blade to track the history of average velocity at the vertex point over the course of simulations. The simulations were stopped when the average velocity at this vertex was fairly constant and did not show any appreciable change. All the above four conditions were satisfied as per the best practices to be followed in ANSYS® Fluent for obtaining an accurate and converged solution.
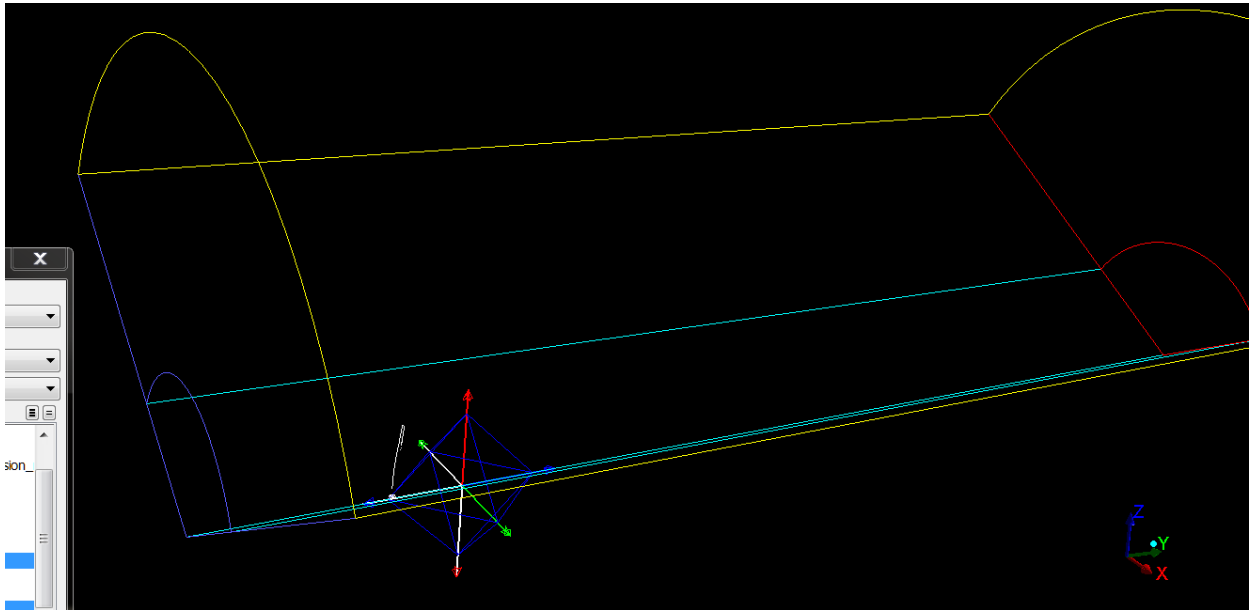
Figure 33: Wake Point for Average Velocity Monitoring

Table 2: Table of CFD Solver Settings

Blade	AOC 15/50 Atlantic Orient Corporation
Solver	Pressure-based
Transient Formulation	Second Order Implicit
Velocity Formulation	Absolute
Time	Steady and Unsteady
Time Step Size	0.01 sec
Time Stepping Method	Fixed
Turbulence Model	k-ω SST
Fluid Material	Air
Moving Reference Frame (Frame Motion)	Symmetric about global Y-axis Rotational Velocity: 65 rpm ≈ 6.8067 rad/s (clockwise)
Wall Condition	Blade is set as moving wall with 0 rad/s and no-slip shear condition.
Temperature	288.16 K

Velocity	5.96, 7.0, 8.03, 10.98, 12.02 m/s
Density	1.225 Kg/m^3
Pressure	101325 Pa
Dynamic Viscosity (μ)	1.7894e-05 Kg/m-s
Ratio of Specific Heats (γ)	1.4
Pressure-Velocity Coupling Scheme	SIMPLE
Spatial Discretization & Interpolation Scheme	Gradient: Least Squares Cell Based
	Pressure: STANDARD
	Momentum: Second Order Upwind
	Turbulent Kinetic Energy: Second Order Upwind
	Specific Dissipation Rate: Second Order Upwind

Results for Flow Simulation over Rotor Blade

Flow simulations were carried at five different wind speeds: 5.96, 7.0, 8.03, 10.98 and 12.02 m/s. Figure 34, displays the power curve obtained from the CFD simulation. The power obtained is calculated from the product of torque (τ) and angular velocity (ω).

$$Power = \tau \cdot \omega \tag{20}$$

Table 3: Power Output Table

Wind Speed	Obtained Power (kW) from CFD
5.96	2.7855
7	7.1425
8.03	16.2099
10.98	38.895
12.02	40.374

Figure 34: Power Output Curve
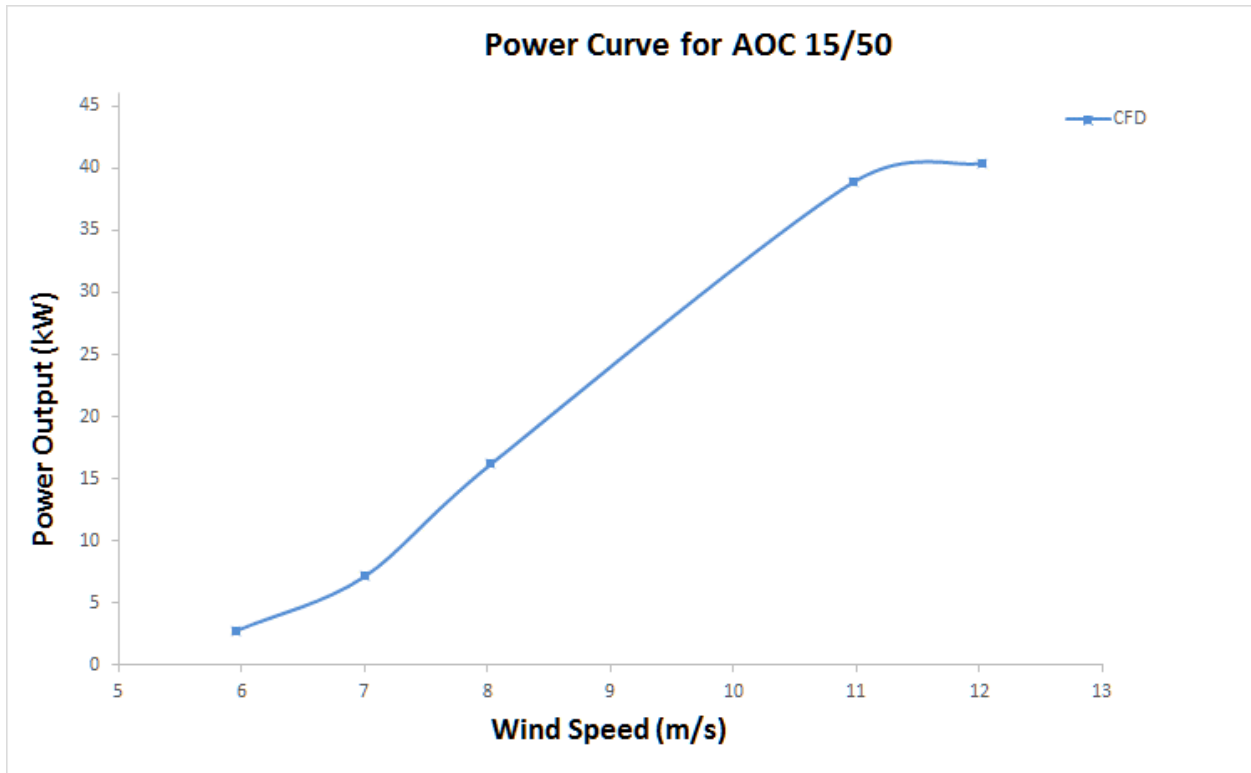
Coefficient of power, a measure of how efficiently a wind turbine converts the energy available in the wind to electricity, is shown in Figure 35.

Table 4: Coefficient of Power Table

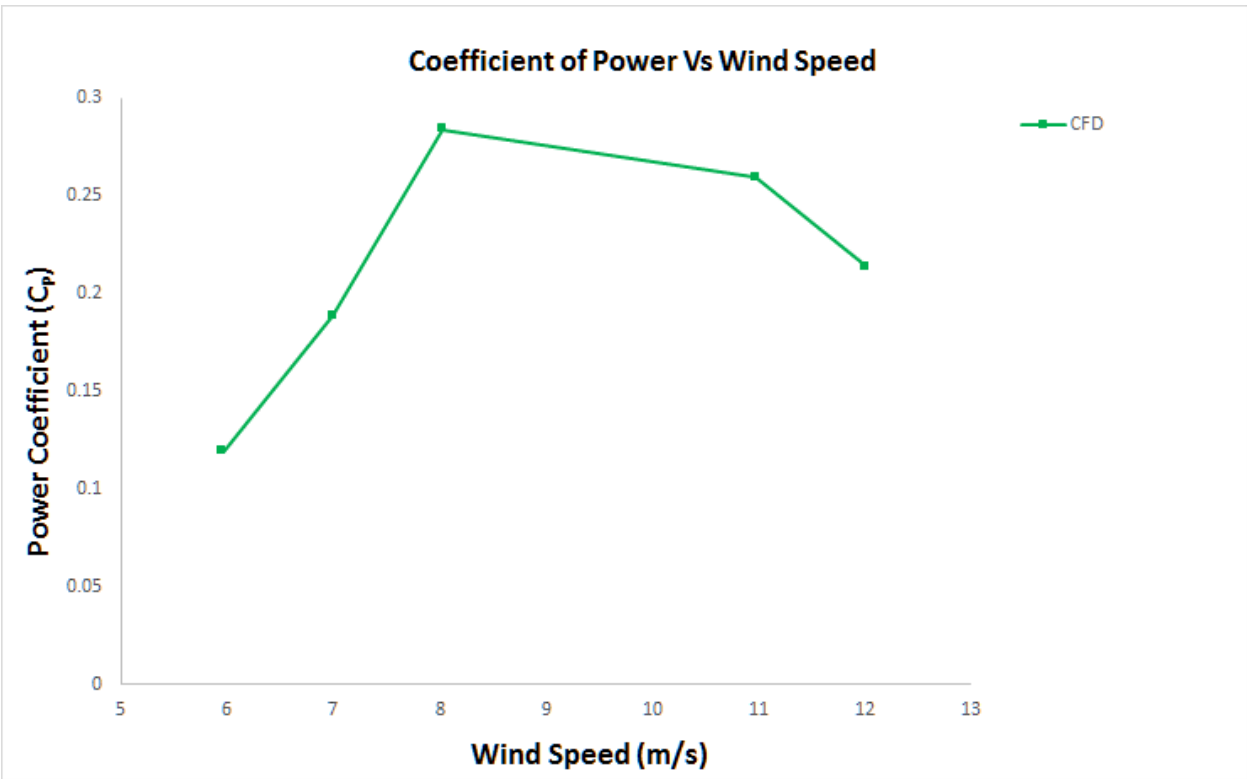| Wind Speed	Obtained Co-efficient of Power (C_P) from CFD
5.96	0.1193
7	0.1888
8.03	0.2839
10.98	0.2597
12.02	0.2139

Figure 35: Power Coefficient Curve

CHAPTER-5

Aerodynamic Optimization

The focus of CFD applications recently has shifted from mere analysis to aerodynamic shape design and optimization. This shift has been mainly motivated by the availability of high performance computing platforms and by the development of new and efficient design and analysis algorithms. Automated design procedures, which use CFD coupled with gradient-based optimization techniques, have had a tremendous impact on the design process by mitigating difficulties in the designing process faced by the engineers.

The recent research and code development efforts in the area of CFD, has proven to be useful in supporting product design and development in many industrial applications. For many product designs where fluid flow simulations are needed, CFD analyses have proven to be quite useful in predicting the flow pattern for a given set of design parameters.

Aerodynamic shape optimization procedures integrated with CFD solvers usually come into play at the preliminary design phase. Shape optimization strategies usually involve the integration of a CFD code with an optimization algorithm. The CFD code performs the flow analysis on a specific shape and provides the optimization algorithm with values of the required components that make up the objective function. The optimization algorithm, based on the evaluation of the objective function value, remodels the geometry in a direction of decreasing or increasing objective function gradients. The new geometry is then re-analyzed and the process is repeated till an optimum shape or configuration is reached.

Optimization of wind turbines is a multidisciplinary process including optimization of aerodynamics, structure, electronics and economics. For the wind turbine blades, the aerodynamics optimization is the major concern.

The aim of this study module is to:

1. Evaluate the dependence of the blade geometric parameters on the power output.

2. Identify the most sensitive geometric parameters by doing a correlation and sensitivity analysis, and;

3. Optimize the wind turbine blade of AOC 15/50 turbine blade for maximum power output.

The objective of optimization is to define and validate a methodology to find a design configuration with increased torque on the blade at the wind speed of 8 m/s. Wind speed of 8 m/s is simulated thorough out the correlation study and optimization routine. Since power is directly proportional to the torque, there would be a consequent increase in the overall blade power output. The optimization routine is carried out by coupling the CFD solver results to the inbuilt optimization module in ANSYS® Workbench called the DesignXplorer®. The optimization process starts with a CFD loop which includes four processes; blade geometry generation, mesh generation for flow domain, CFD simulation and post-processing the CFD data. An approximate output model is built based on the CFD solver result database to evaluate the necessary design iterations required for achieving the objective of optimization. The objective function or output depends on certain characteristics of the system, called *variables* or *unknowns*. The goal is to find values of the variables that optimize the objective. Often the variables are restricted, or rather *constrained*, in some way within given limits.

Mathematically, optimization is the minimization or maximization of a function subject to constraints on its variables. The optimization problem can be written as follows:

Min (**X**)   subject to $g(\mathbf{X}) = 0$, $i=1,2,\ldots m$
$x \in R^n$ $h(\mathbf{X}) \leq 0$, $k=1,2,\ldots p$

- **X** is the vector of variables, also called unknowns or input parameters;

- *f* is the objective function, a scalar function of **X** that has to be optimized.

- g_i and h_k are the constraint functions, which are scalar functions of **X** that define certain equalities and inequalities that **X** must satisfy.

- m and p are the number of equalities and inequalities constraints.

5.1 Parametric Correlation Study

A Parameteric Correlation study feature in ANSYS® Design Exploration bench allows one to:

a. Determine which input parameters have the most (and the least) impact on your design.

b. Identify the degree to which the relationship is linear/quadratic.

It also provides the following visual tools to assist in assessment of parametric impacts:

- Correlation Matrix and Chart

- Determination Matrix and Chart

- Correlation Scatter Plot

- Sensitivity Chart

5.1.1 Spearman's Rank Correlation

This correlation method is used for this parametric study as it has the following advantages over Pearson's Linear Correlation model:

I. Uses ranks of data.

II. Correlation coefficients are based on the rank of samples.

III. Recognizes non-linear *montonic* relationships (which are less restrictive than linear ones). In a *monotonic* relationship, one of the following two things happens:

   - As the value of one variable increases, the value of the other variable increases as well.

   - As the value of one variable increases, the value of the other variable decreases.

IV. Deemed the more accurate method.

The advantage of using a parametric correlation and sensitivity study approach is to find the most important variables and excluding the lesser important ones to reduce the generation of unwanted sampling space without much effect on the objective outcome. Parameter correlation thus helps in identifying the effect of input variables to the outcome and also determines how sensitive these variables are which govern the objective function.
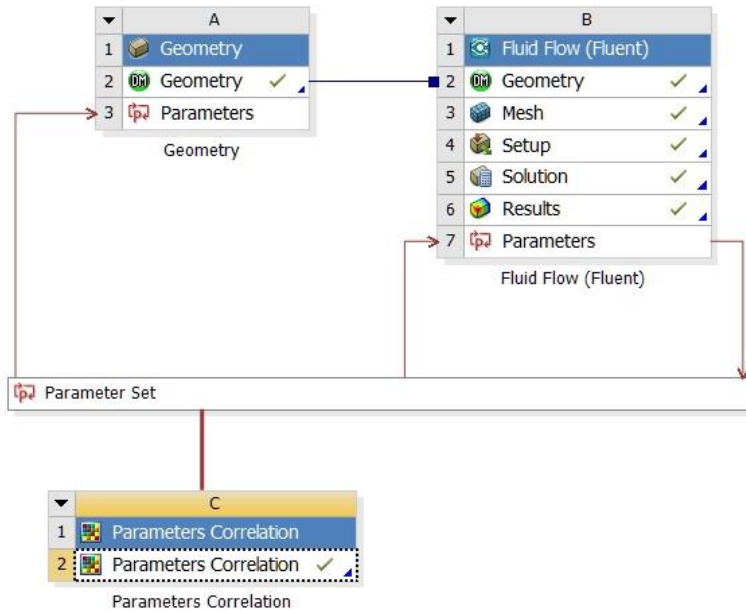
Figure 36: Parametric Correlation Project Schematic

1	ID	Parameter Name	Value	Unit
2	☐ Input Parameters			
3	☐ 🛢 Geometry (A1)			
4	🔩 P1	Chord_Station2	0.749	
5	🔩 P2	Chord_Station3	0.5469	
6	🔩 P3	Chord_Station4	0.406	
7	🔩 P4	Radius_Station4	4.74	
8	🔩 P5	Radius_Station3	2.826	
9	🔩 P6	Radius_Station2	1	
10	🔩 P7	Attach_Angle	1.54	
11	🔩 P8	Twist_Station2	0	
12	🔩 P9	Twist_Station3	0	
13	🔩 P10	Twist_Station4	-1.54	
14	🔩 P11	Cone_Angle	6	
*	🔩 New input parameter	New name	New expression	
16	☐ Output Parameters			
17	☐ 🟢 Fluid Flow (Fluent) (B1)			
18	🔩 P12	Torque	841.1	J

Figure 37: Input and Output Parameters Outline

Figures 36 and 37 depict the parametric correlation schematic and parametric outline respectively.

A total of 128 design points were generated by the algorithm to generate the parametric correlation
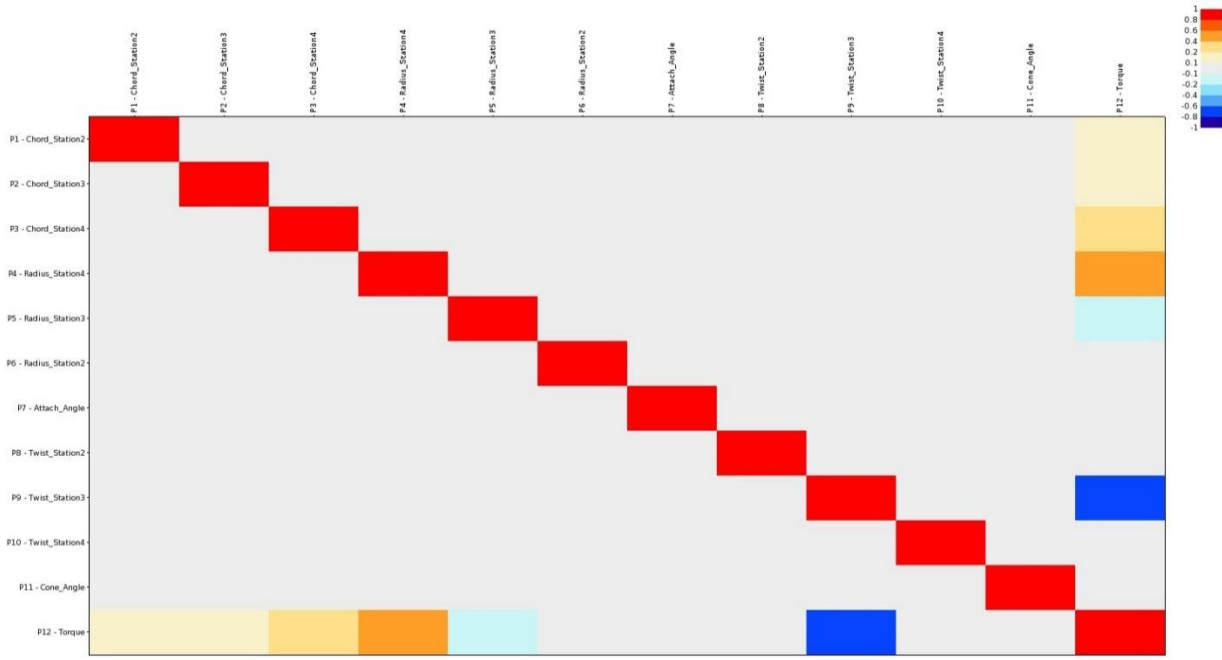
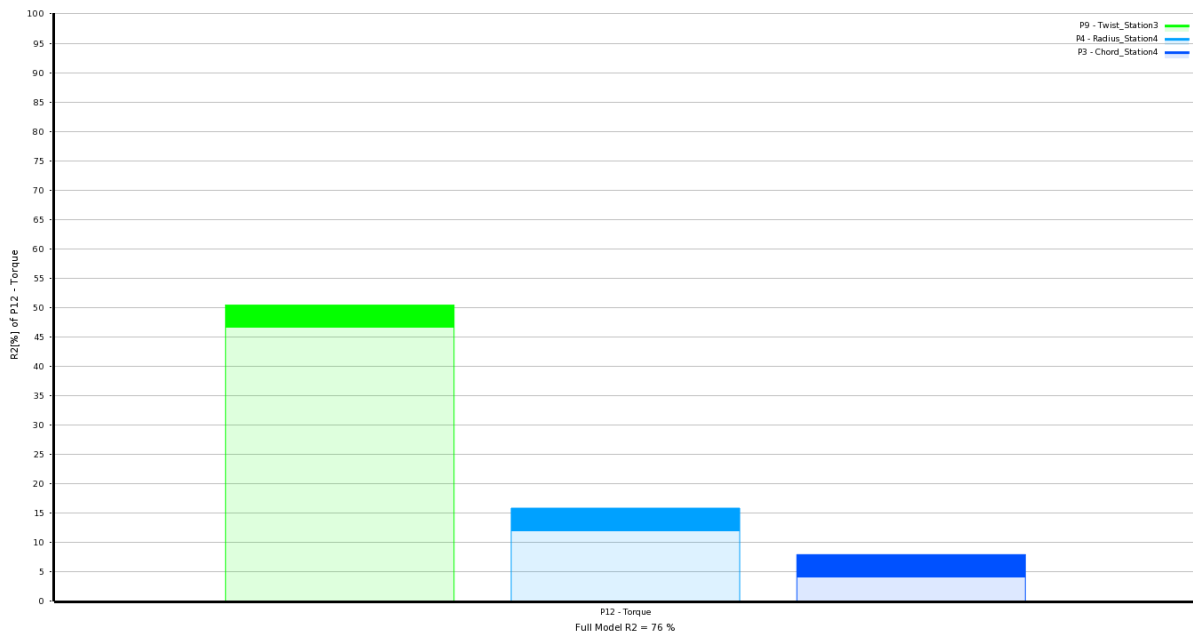results.

59

Figure 38: Linear Correlation Matrix

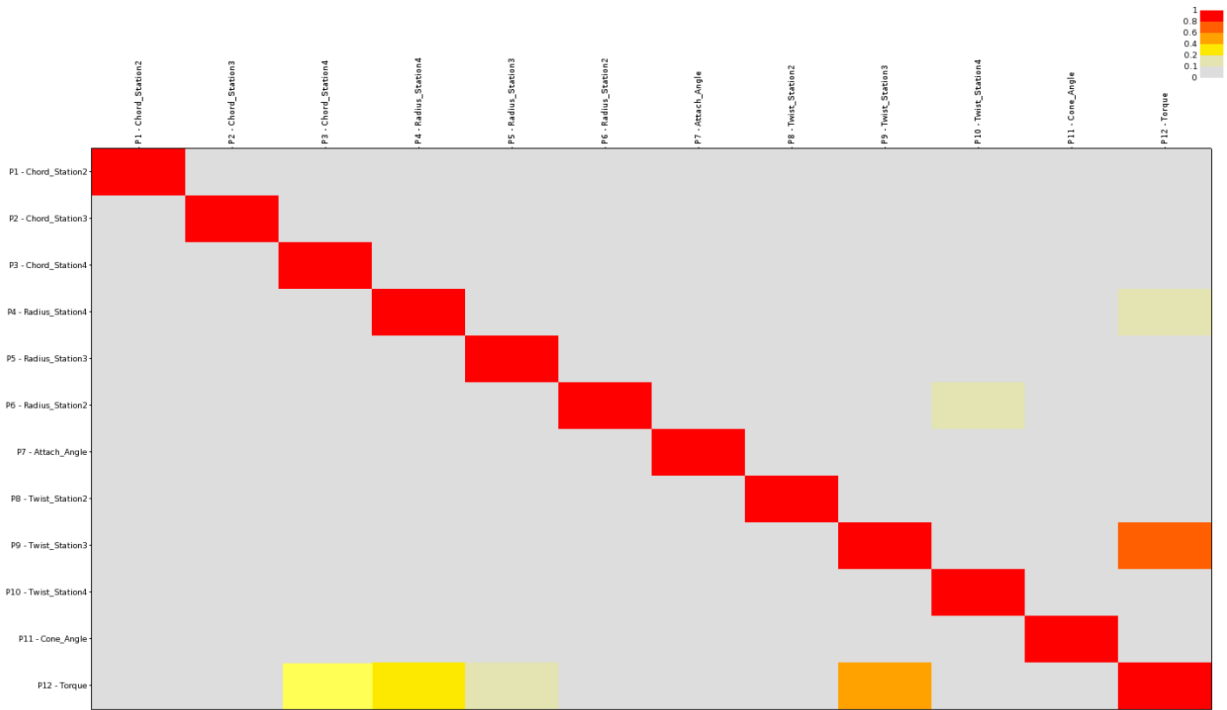*Figure 39: Coefficient of Determination (Linear) Model*

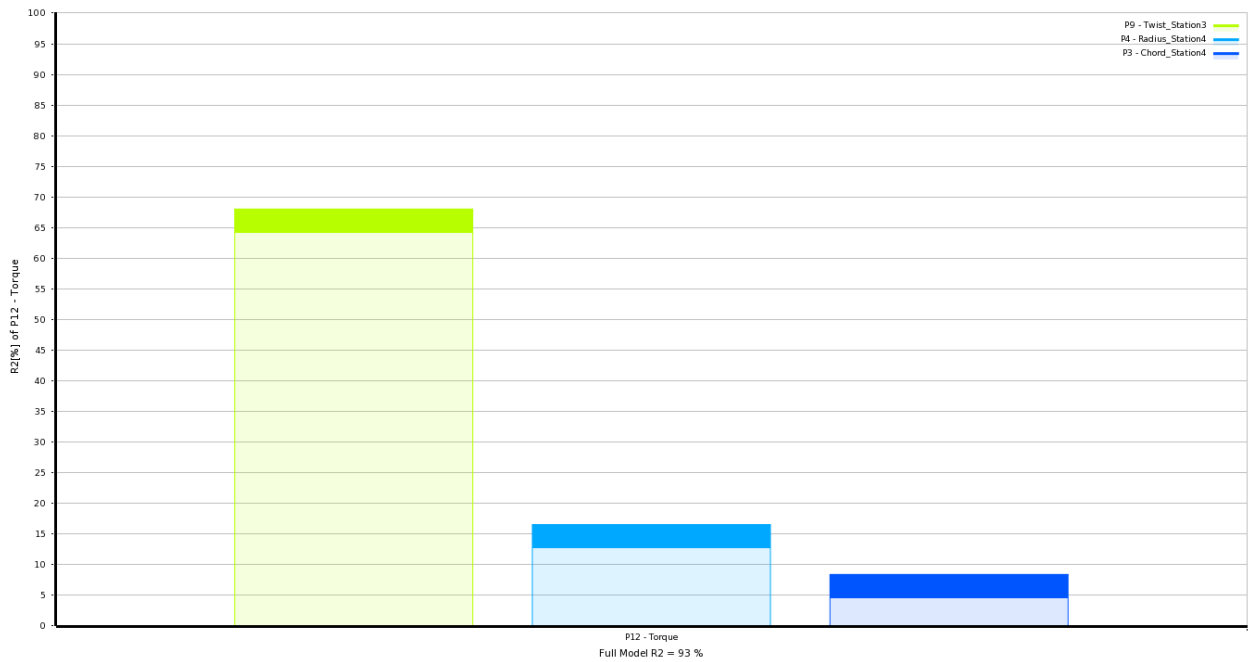*Figure 40: Quadratic Determination Matrix*

Figure 41: Coefficient of Determination (Quadratic) Model

As seen from the Figures 38-41, it can be concluded that input parameters P3 (Chord_Station 4), P4 (Radius_Station 4) and P9 (Twist_Station 3) have the most impact on the output parameter P12 (Torque). The same can also be corroborated from the determination histogram charts as shown in Figure 39 & 41. The *Determination Histogram* chart allows one to see what inputs drive a selected output parameter. From the Figures 39 and 41, one can see that input parameters P3 (Chord_Station 4), P4 (Radius_Station 4) and P9 (Twist_Station 3) affect output P12 (Torque). It can also be inferred that of the three inputs, P9 (Twist_Station 3) has by far the greatest impact.

The *Full Model Coefficient of Determination*, R2 (%) value also shows how well output variations are explained by input variations. The closer this value is to 100%, the more certain it is that output variations result from the inputs. The lower the value, the more likely that other factors such as noise, mesh error, or an insufficient number of points may be causing the output variations.

In our case, the coefficient of determination of the Linear Model ($R2_{Linear}$) = 76% and the coefficient of determination of the Quadratic Model ($R2_{Quad.}$) = 93%. In some cases, the relationship between parameters may be more complex and cannot be explained completely with a linear or quadratic correlation.

From the above results, unlike the *Linear Correlation*, the strong *Quadratic Correlation* indicates the optimization problem statement as more quadratic. Determination histogram supports that objective function is greatly dependent on the design variables and correlation scatter of the variable parameters in Appendix C supports this claim with more number of DoE points lying along the quadratic trend line.
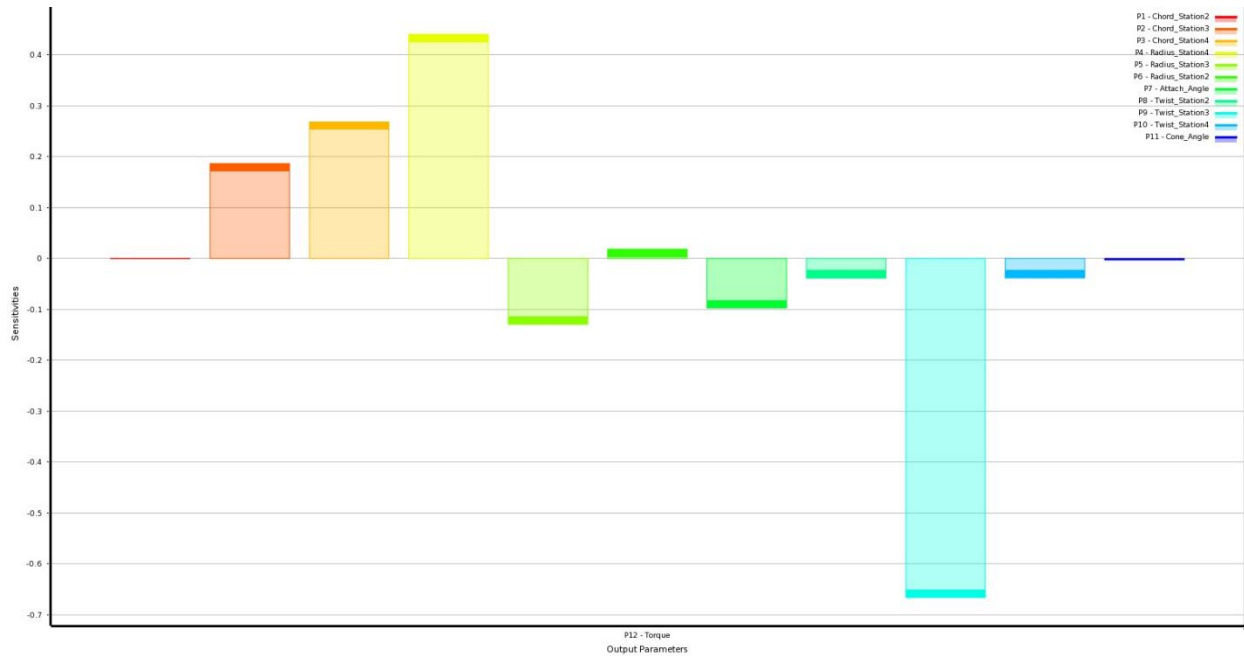
Figure 42: Global Sensitivity Plot for Input and Output Parameters

The *sensitivity* chart in Figure 42 shows global sensitivities of the output parameters with respect to the input parameters. Positive sensitivity occurs when increasing the input increases the output. Negative sensitivity occurs when increasing the input decreases the output. Again, from the above chart we can conclude that input parameters P3 (Chord_Station 4), P4 (Radius_Station 4) and P9 (Twist_Station 3) have the strongest influence on the output P12 (Torque). Also, P3 (Chord_Station 4) and P4 (Radius_Station 4) have a positive sensitivity, while P9 (Twist_Station 3) exhibits a strong negative sensitivity from the full model of the optimization problem.

5.2 Introduction to Response Surface Based Optimization

The evaluation of aerodynamic designs often consists of long running and computationally intensive CFD simulations. Unlike the earlier engineering methodologies adopted to design aerospace systems, in which predominantly hand calculations and wind tunnel tests were used in a cut-and-try fashion, engineers lately have resorted to Computer Aided Engineering (CAE) of which CFD is an important part.

CFD, as discussed previously, has evolved from a mere flow analysis tool to an important design tool. However, even with the ever expanding computational resources, it has widely been regarded as a computationally expensive platform, especially when it comes to very high-fidelity flow simulations. The use of long running expensive computer simulation in design, therefore leads to a fundamental problem when trying to compare and contrast various competing options, there are never sufficient resources to analyze all of the combinations of variables that one would wish. This problem is particularly acute when using higher optimization schemes. All optimization methods depend on some form of internal model of the problem space they are exploring. To build such a model when there are many variables can require large numbers of analysis to be carried out, particularly if using finite difference methods to evaluate gradients.

Objective function and constraints in aerodynamic shape optimization involving flow numerical simulation, such as CFD, may be non-smooth and noisy. Non-smoothness is created by the presence of flow discontinuities such as shock waves. Noise can be caused either by the changes in computational mesh geometry due to free boundaries or by poor convergence of numerical schemes. Although these features account for a small change in some design parameters, it could lead to a huge ramification in the objective function or constraints.

These non-smoothness and noise issues of the objective function become more serious in gradient-based optimization methods (GBOMs), where the objective function value as well as its gradient information is used. In multidisciplinary design optimization (MDO) problems, which usually have objective functions coupled with numerous constraints, it is significantly difficult to formulate the design problem with GBOMs. Because the optimization depends greatly on the formulation of the design problem, the process of searching for the optimum is likely to render just a local value. Another shortcoming of GBOMs is that because many analysis programs were not written with an automated design process in mind, the subsequent adaptation of these programs to an optimization code may need significant reprogramming in the analysis routine.

5.2.1 Response Surface Optimization (RSO) Methodology

In general, *response surface methodology* explores the relationships between several input variables and one or more response variables. The method was introduced by *G. E. P. Box* and *K. B. Wilson* in 1951 [46]. The main idea of response surface methodology is to use a sequence of designed experiments to converge to an optimal response. Incorporating this routine in the context of design optimization falls into the category of *Surrogate* or *Response Surface Optimization* (RSO). It has emerged as an effective approach for the design of computationally expensive models such as those found in aerospace systems, involving aerodynamics, structures, and propulsion.

For a new or a computationally expensive design, optimization based on an inexpensive surrogate, such as *Response Surface Model* (also known as surrogate or approximation models), is a good choice. RSO helps in the determination of an optimum design candidate, and also aids by providing

insight into the workings of the design. A response model not only provides the benefit of low-cost for output evaluations, it also helps revise the problem definition of a design task. Furthermore, it can conveniently handle the existence of multiple desirable design points and offer quantitative assessments of trade-offs as well as facilitate global sensitivity evaluations of the design variables.

Thus, the use of *Response Surface Models* (RSM) in optimization is becoming increasingly popular. The RSM is not in itself an optimizer, but instead a helper tool for increasing the speed of optimization. Instead of making direct calls to a computationally expensive numerical analysis code, such as CFD, an optimization routine takes values from a cheap surrogate model, that is formulated using a specific set of responses obtained from the numerical code. The popularity of such methods has probably increased due to the development of approximation methods which are better able to capture the nature of a multi-modal design space.

The main objective behind creating an RSM is to be able to predict the response of a system for an operating point without actually performing a simulated analysis at that point. The response of the system can then be predicted just by inputting the operating point values into the RSM and obtaining the value of the response. The RSM basically takes the shape of a mathematical equation ($\mathbf{x}$), essentially a quadratic polynomial, which takes the values of the design variables $\mathbf{X}$ as an input, and returns an approximated value of the system response. Various optimization methodologies can then be employed to optimize this computationally cheap response model in order to obtain the best operating point.

Some of the other benefits of using RSM include -

- It smoothens out the high-frequency noise of the objective function and is, thus, expected

to find a solution near the global optimum.

- Various objectives and constraints can be attempted in the design process without

additional numerical computations.

- It does not require a modification in analysis codes.

RSO is composed of four phases as show in the process flowchart in Figure 43:

I. *Sampling (Design of Experiments)* - this basically involves testing or obtaining actual values of the system response, by performing simulations for a select set of points within the design space.

II. *Response Surface Construction* - based on the responses obtained for the sampling points, a RSM is constructed. The RSM is an approximation of the system response.

III. *RSO* - Optimization algorithms are used to optimize the RSM and obtain the best operating point values of the system.

IV. *RSM improvement* - The RSM approximation is improved by training it further by including additional simulated responses.
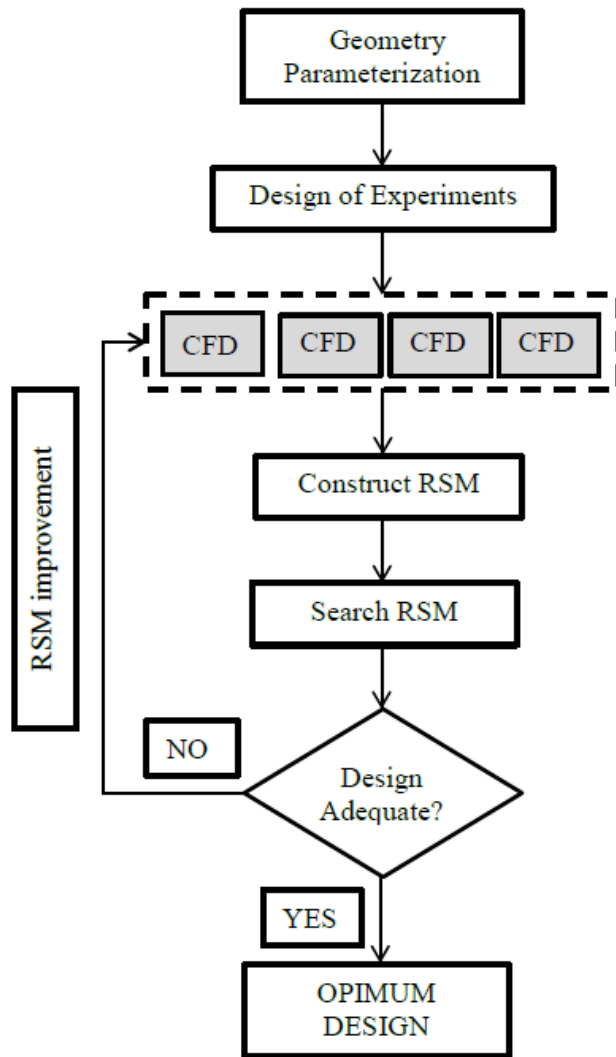
Figure 43: General RSO Procedure Flowchart

5.2.2 Design Variables

From an aerodynamic shape optimization point of view, the *system* is basically the blade geometry that has to be optimized for a specific operating condition (wind speed). The *design points* are the design variables that completely define the blade geometry. In this problem formulation, there are 11 design variables, namely: radial sectional fraction (r/R) of three airfoil

sections, chord length (c) of the three airfoil sections, twist angle (θ) of the three airfoil sections from which the entire blade is lofted span-wise. The blade cone angle (φ) is the tenth and the attach angle (α) also called as the pitch angle is the eleventh design variable.

5.2.3 Design Space

The design space is the region bounded by the upper and lower limits of the design variables. This implies that the design variables are allowed to vary only within the limits defined by the design space. It is defined such that, overly unusual or unrealistic shapes are not attained.

Table 5: Table Showing Design Space

Design Variable	Design Variable Base Value	Design Variable Lower Bound	Design Variable Upper Bound
Chord_Station 2 **(P1)**	0.749 m	0.6741 m	0.8239 m
Chord_Station 3 **(P2)**	0.5469 m	0.49221 m	0.60159 m
Chord_Station 4 **(P3)**	0.406 m	0.3654 m	0.4466 m
Radius_Station 4 **(P4)**	4.74 m	4.266 m	5.214 m
Radius_Station 3 **(P5)**	2.826 m	2.5434 m	3.1086 m
Radius_Station 2 **(P6)**	1 m	0.9 m	1.1 m
Attach_Angle **(P7)**	1.54°	-3°	3°
Twist_Station 2 **(P8)**	0°	-5°	10°
Twist_Station 3 **(P9)**	0°	-5°	10°
Twist_Station 3 **(P10)**	-1.54°	-3°	3°
Cone_Angle **(P11)**	6°	0°	10°

5.2.4 Design of Experiments

In the Design of Experiments (DoE) phase of the RSM, the design space is systematically explored using the DoE technique, which generates the test matrix of design points to be computed in each computational experiment. The aim of DoE is to discretize the entire design space in a way such that a matrix of design variable values is obtained. This is done by discretizing the variation range of each design variable into N_s levels. Combining the values of all the design variables at a specific level yields one experiment. Combining all the above yielded experiments therefore forms a set of N_s experiments, which is thereby referred to as a DoE.

If $\mathbf{X}$ is the design vector consisting of N_{var} design variables (DV), and if each design variable is split into N_s levels, the DoE matrix is given by Figure 44,

$$\mathbf{X}_{DoE} = \underbrace{\begin{bmatrix} \mathbf{X}_{11} & \mathbf{X}_{12} & \cdots & \mathbf{X}_{1N_{var}} \\ \mathbf{X}_{21} & \mathbf{X}_{22} & \cdots & \mathbf{X}_{2N_{var}} \\ \vdots & \vdots & \ddots & \vdots \\ \mathbf{X}_{N_s 1} & \mathbf{X}_{N_s 2} & \cdots & \mathbf{X}_{N_s N_{var}} \end{bmatrix}}_{Design\ Variables\ DV\ 1\ to\ DV\ N_{var}} \begin{matrix} \leftarrow Experiment-1 \\ \leftarrow Experiment-2 \\ \vdots \\ \leftarrow Experiment-N_s \end{matrix}$$

Figure 44: Design of Experiments (DoE) Matrix Representation

Latin Hypercube Sampling (LHS)

In this study, Latin Hypercube Sampling (LHS) methodology has been used to generate the RSM. It is a statistical method for generating a distribution of plausible collections of design variable values from a multidimensional distribution. This method is often used as a DoE technique.

In geometry, a *hypercube* is an *n*-dimensional analogue of a square ($n = 2$) and a cube ($n = 3$). It is a closed, compact, convex figure whose one-skeleton consists of groups of opposite parallel segments aligned in each of the space's dimensions, perpendicular to each other and of the same length. A *hyperplane* is also a concept which is a generalization of the plane into a different number of dimensions spread in *n*-dimensional space. A *hyperplane* of an *n*-dimensional space is a flat subset with dimension $n - 1$.

In the context of sampling in statistics, a square grid containing sample positions is a Latin square if (and only if) there is only one sample in each row and each column of the design matrix. A Latin Hypercube is nothing but the generalization of this concept to an arbitrary number of dimensions, whereby each individual sample point is the only one in each axis-aligned *hyperplane* containing it.

When sampling a function of N_{var} variables, the range of each variable is divided into equally probable intervals. The N_s sample points are then placed to satisfy the Latin Hypercube requirements; doing so forces the number of divisions N_s, to be equal for each variable. It should be noted that this sampling scheme does not require more samples for more dimensions (variables); this independence is one of the main advantages of this sampling scheme. For example, for $N_{var} = 4$ (4 design variables), and $Ns=4$ (4 levels), a Latin Hypercube Sampling may take the form as shown in Figure 45 below:

2	1	3	4	← Level − 1
3	2	4	1	← Level − 2
1	4	2	3	← Level − 3
4	3	1	2	← Level − 4

↑ DV 1   ↑ DV 2   ↑ DV 3   ↑ DV 4

Figure 45: Latin Hypercube Sample

Building a *Latin hypercube*, that is the multidimensional, can be done in a similar way. The design space of each dimension is split into equal number of levels and the points are placed in the levels such that any arbitrary vector emerging from the points in a direction parallel to any of the dimensional axes does not encounter with any other point in its way.

This is achieved using the following technique. If $\mathbf{X}$ denotes the $N_s \times N_{var}$ the DoE matrix N_s points in N_{var} dimensions (each row represents a point), then each column of $\mathbf{X}$ is filled with random permutations $(1, 2, \ldots, N_s)$ and stratified such that no specific point in any row is repeated in more than one column. This set is then normalized such that values lie within $[0,1]^{N_{var}}$ (Figure 46).
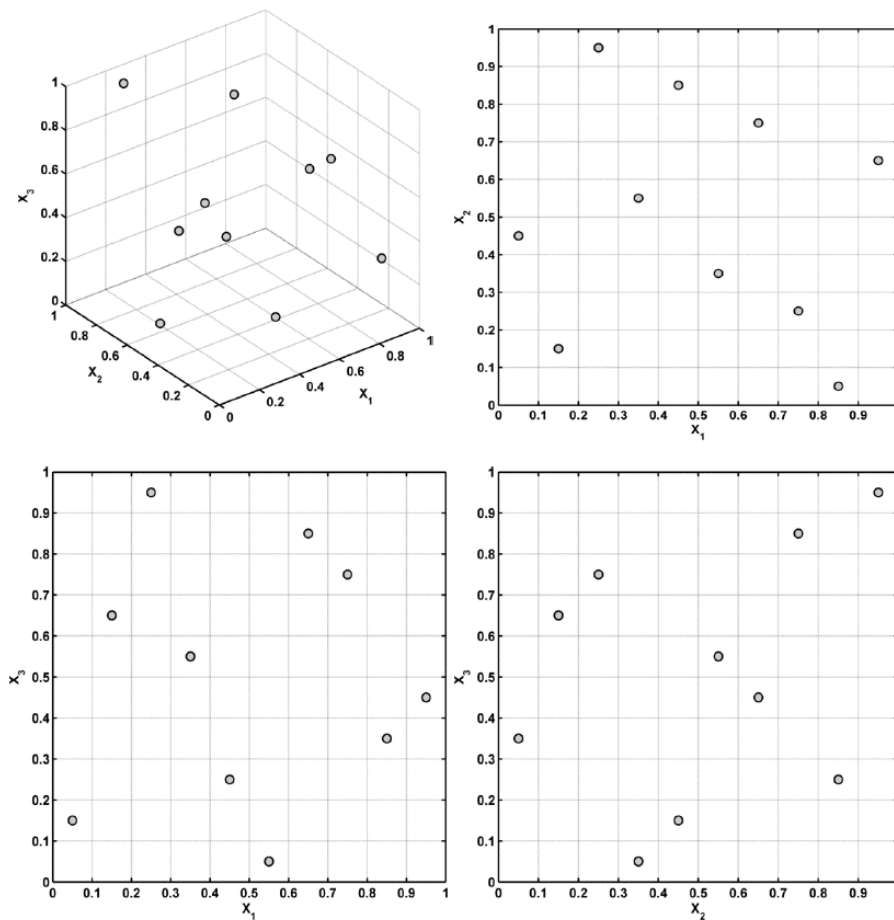
Figure 46: Three Variable, 10 Point LHS Plan in Three Dimensions, Along with the Two-Dimensional Projections [14]

Design Matrix

The design matrix is formed by concatenating the values of the design variables at all levels. In order to do so, the design space needs to be discretized into levels which are equal to the desired number of computer simulations to be performed. The design space as described above is the region bounded by the upper and lower limits of the design variables.

The range of each of the design variables DV_{Range} (the design space) is the difference between the upper, DV_{Upper}, and lower limits, DV_{Lower}, of the design variable. This range is discretized into equal number of levels N_s which is equivalent to the number of experiments (computer simulations) to be performed. To obtain the values of the design variables at each level, first a LHS plan is generated for the 10 design variables and N_s levels. This generates a matrix L of size (N_s x 10), with the N_s values in each of the 10 columns varying from 0 to 1 in a LHS pattern.

The values of the design variables at each level are then obtained based on the following equation:

$$\mathbf{X}_{DoE}(i,) = DV_{Lower}(j) + [DV_{Range}(j) \times L(i,j)] \qquad \text{For } i=1,2,\ldots, N_s$$

$$\text{For } j=1,2,\ldots,10. \qquad (21)$$

The matrix thus formed, describes the set of blade geometries for which the CFD simulations are to be performed in order to construct the RSM. The DoE algorithm generated 151 design points to obtain a fully trained RSM based on the 2^k factorial design.

Constructing the RSM

RSM builds a response model by calculating data points with experimental design theory to prescribe a response of a system with independent variables. The relationship can be written in a general form as follows:

$$y = F(\mathbf{X}) + \epsilon \tag{22}$$

where ϵ represents the total error, which is often assumed to have a normal distribution with a zero mean. Consider a sampling plan $\mathbf{X}$ and a set of N_s observed values comprising the responses obtained from the computer simulations:

$$\mathbf{X} = \mathbf{X}_{DoE} = \begin{bmatrix} x_{11} & x_{12} & \cdots & x_{1N_{var}} \\ x_{21} & x_{22} & \cdots & x_{2N_{var}} \\ \vdots & \vdots & \ddots & \vdots \\ x_{N_s1} & x_{N_s2} & \cdots & x_{N_sN_{var}} \end{bmatrix} \begin{array}{c} \rightarrow \\ \rightarrow \\ \vdots \\ \rightarrow \end{array} \begin{bmatrix} y_1 \\ y_2 \\ \vdots \\ y_{N_s} \end{bmatrix} \tag{23}$$

The polynomial approximation of order m (degree $m-1$) of a function f is, essentially, a Taylor series expansion of f truncated after $m-1$ terms. This suggests that a higher order expansion will usually yield a more accurate approximation. However, the greater the number of terms, the more flexible the model becomes and there is a danger of over-fitting the noise that may be corrupting the underlying response values, thereby introducing truncation errors in the predicted output function value.

A full quadratic polynomial (degree 2, order 3) approximation of F can be written as:

$$\hat{y} = \hat{f}(\mathbf{x}, \boldsymbol{\beta}) = \beta_1 + \sum_{i=1}^{N_{var}} \beta_i x_i + \sum_{j=1}^{N_{var}} \beta_{jj} x_j^2 + \sum_{i=1}^{N_{var}-1} \sum_{j=i+1}^{N_{var}} \beta_{ij} x_i x_j \qquad (24)$$

Here $\beta 0$, βi, βij etc. are the regression coefficients of the polynomial. The total number of these coefficients is $n_t = (N_{var}+1)(N_{var}+2)/2$. These values can be determined using the standard least-square fitting regression of an over determined problem:

$$\mathbf{y} = \boldsymbol{\Phi}\boldsymbol{\beta} \qquad (25)$$

Here $\mathbf{y}$ is the initial response matrix $[y_1, y_2,\ldots,]^T$ and $\boldsymbol{\Phi}$ is the Vandermonde matrix of size ($N_s \times N_{var}$) given by:

$$\boldsymbol{\Phi} =$$

$$\begin{bmatrix} 1 & x_{11} & x_{12} & \cdots & x_{1N_{var}} & x_{11}^2 & x_{12}^2 & \cdots & x_{1N_{var}}^2 & x_{11}x_{12} & x_{11}x_{13} & \cdots & x_{1N_{var}-1}x_{1N_{var}} \\ 1 & x_{21} & x_{22} & \cdots & x_{2N_{var}} & x_{21}^2 & x_{22}^2 & \cdots & x_{2N_{var}}^2 & x_{21}x_{22} & x_{21}x_{23} & \cdots & x_{2N_{var}-1}x_{2N_{var}} \\ \vdots & \vdots & \vdots & \cdots & \vdots & \vdots & \vdots & \cdots & \vdots & \vdots & \vdots & \cdots & \vdots \\ 1 & x_{N_s1} & x_{N_s2} & \cdots & x_{N_sN_{var}} & x_{N_s1}^2 & x_{N_s2}^2 & \cdots & x_{N_sN_{var}}^2 & x_{N_s1}x_{N_s2} & x_{N_s1}x_{N_s3} & \cdots & x_{N_sN_{var}-1}x_{N_sN_{var}} \end{bmatrix} \qquad (26)$$

$$\text{And } \boldsymbol{\beta} = \begin{bmatrix} \beta_1 \\ \beta_2 \\ \vdots \\ \beta_{n_t} \end{bmatrix}$$
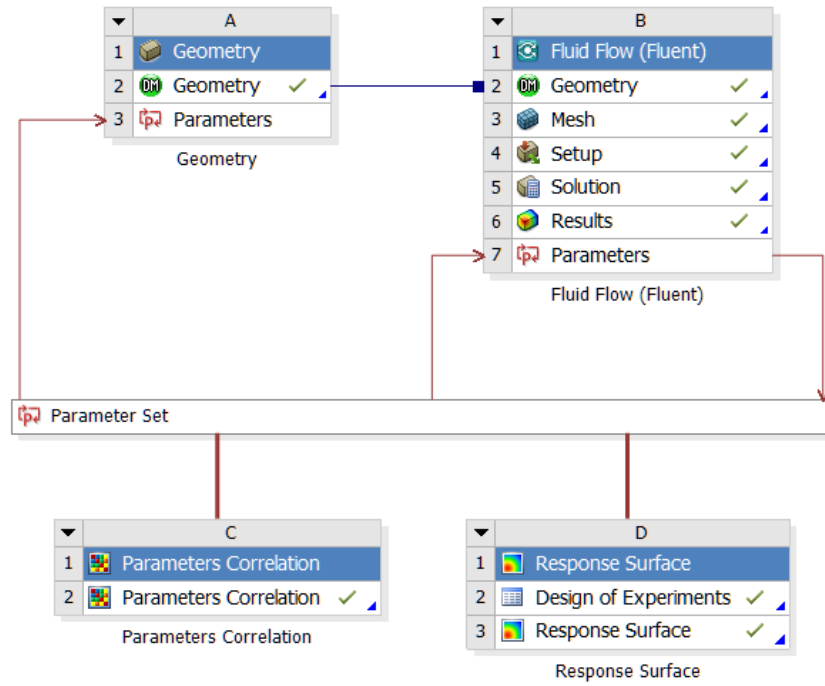
Figure 47: Design of Experiments & Response Surface Generation Project Schematic
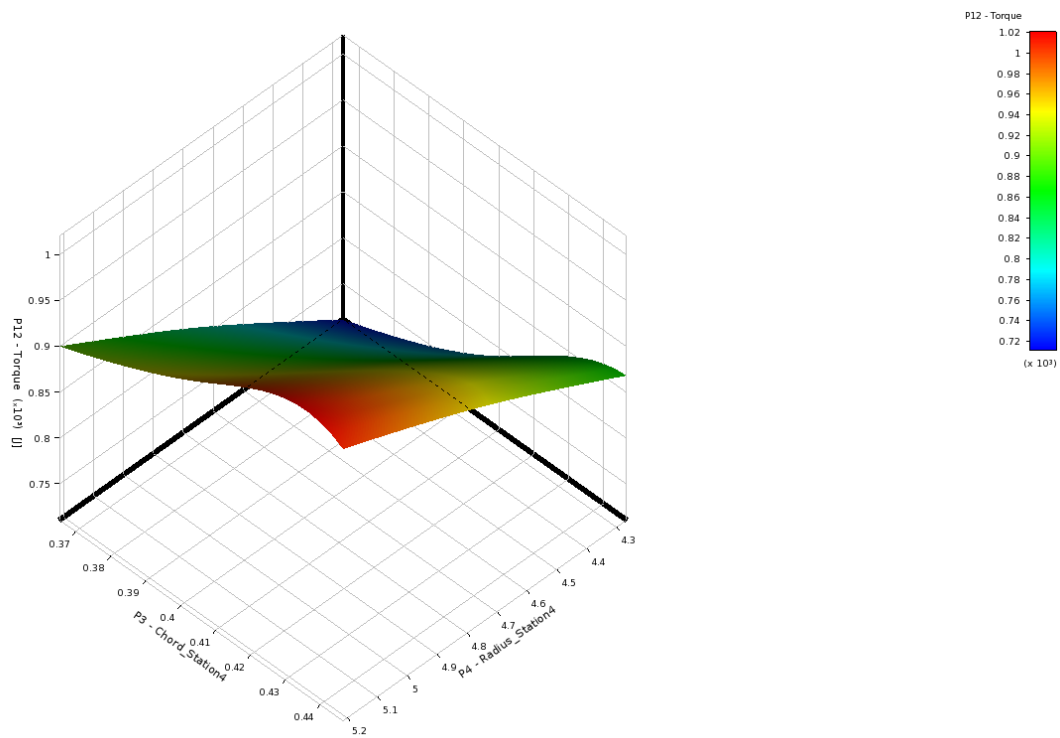
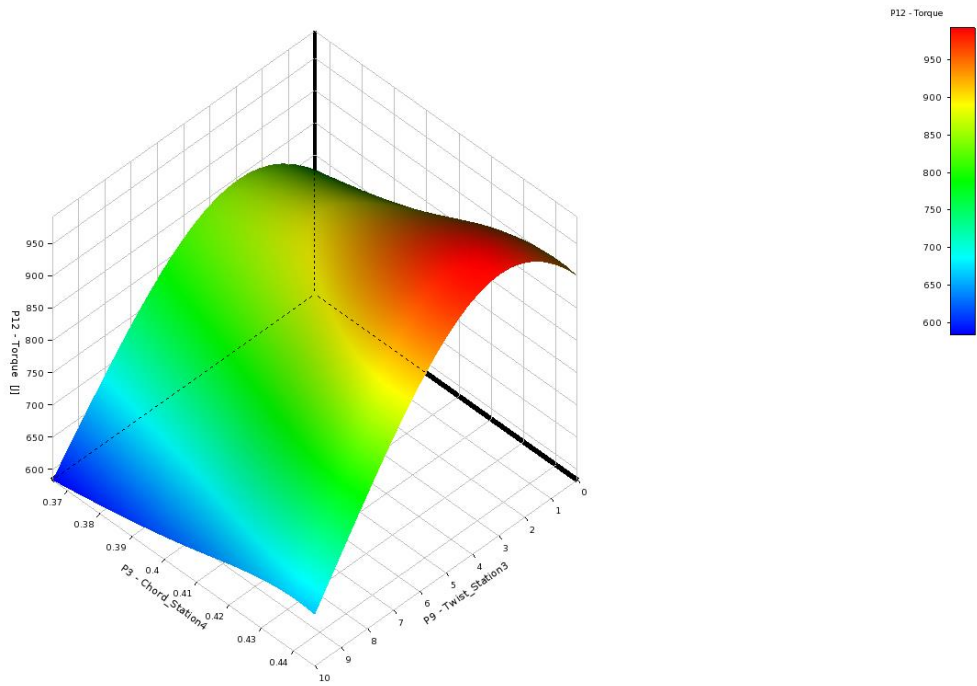*Figure 48: Response Surface Showing Variation of P3, P4 with respect to P12 (Output)*

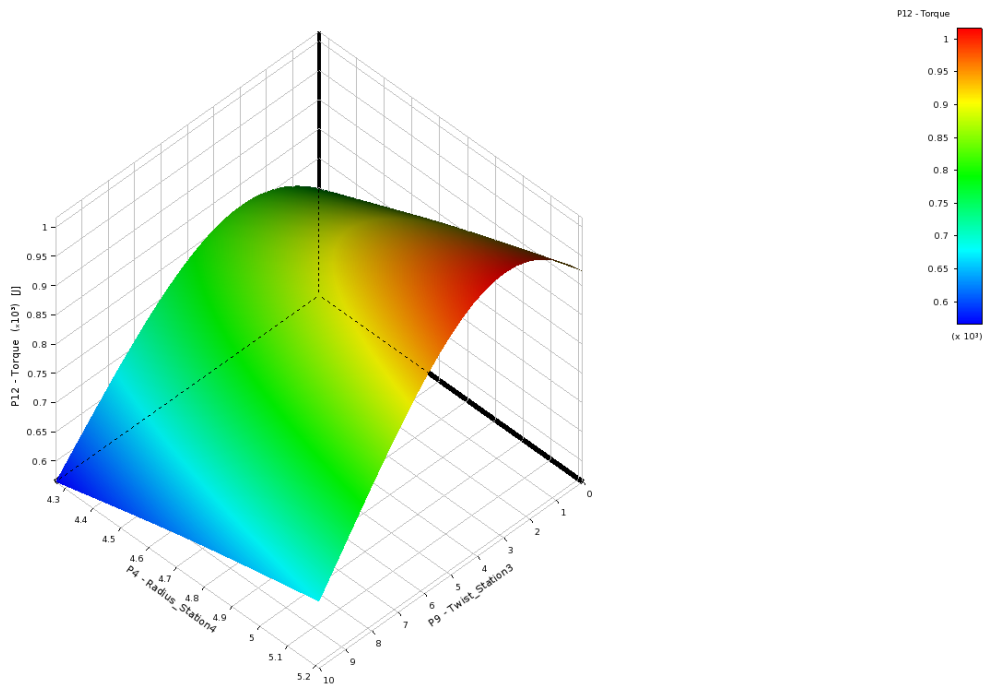*Figure 49: Response Surface Showing Variation of P3, P9 with respect to P12 (Output)*

Figure 50: Response Surface Showing Variation of P4, P9 with respect to P12 (Output)

77

Testing the RSM Model

Once the RSM is available, it is equally important to establish the predictive capabilities of the surrogate model in deviation from the available data. In the context of an RSM, several measures of predictive capability are available:

Adjusted root mean square error:

The error ε_i at any point i is given by

$$\varepsilon_i = y_i - \hat{y}_i \tag{27}$$

where y_i is the actual value and $\hat{y}_i$ is the predicted value.

Hence the adjusted root mean square error σ_a is given by;

$$\sigma_a = \sqrt{\frac{\sum_{i=1}^{N_s} \varepsilon_i^2}{(N_s - n_t)}} \tag{28}$$

For a good fit, RMS error (σ_a) should be small compared to the data.

Coefficient of multiple determination:

The adjusted coefficient of multiple determination R^2_{adj} defines the prediction capability of the RSM as:

$$R^2_{adj} = 1 - \left(\frac{\sigma_a^2 (N_s - 1)}{\sum_{i=1}^{N_s} (y_i - \bar{y})^2} \right), \qquad \text{where } \bar{y} = \frac{\sum_{i=1}^{N_s} y_i}{N_s} \tag{29}$$

For a good fit, R^2_{adj} should be close to 1.

Coefficient of Determination (Best Value = 1)	★★	0.97069
Adjusted Coeff of Determination (Best Value = 1)	★	0.96468
Root Mean Square Error (Best Value = 0)	★	2.2129
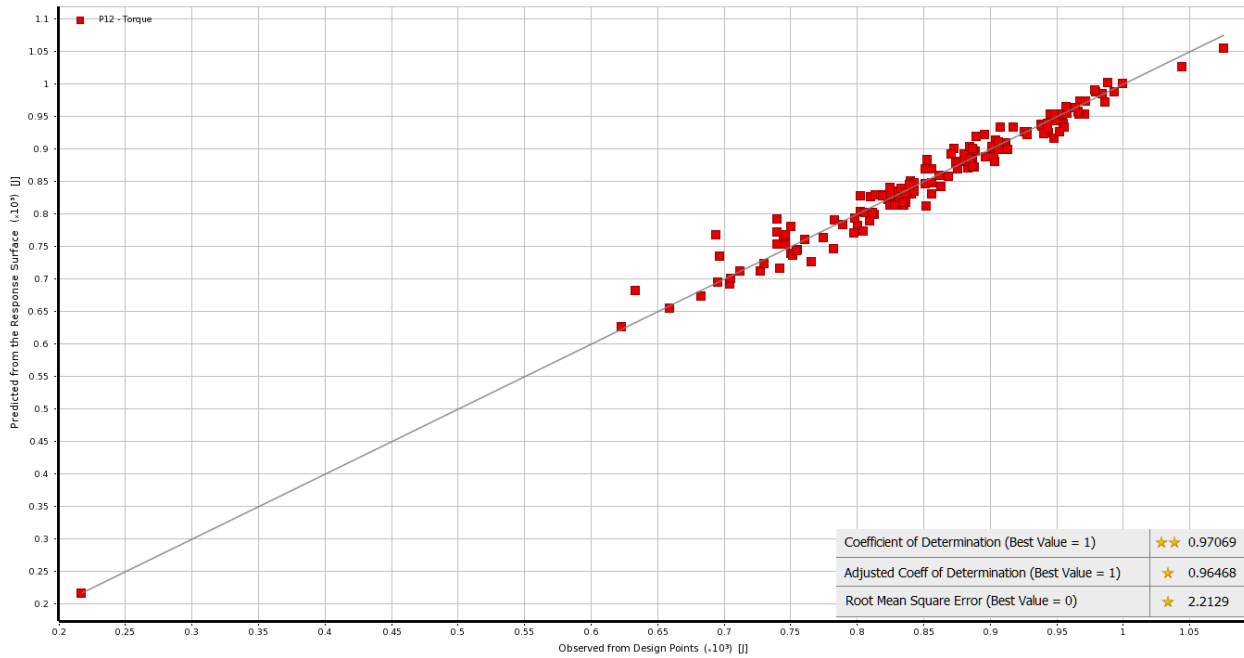
Figure 51: RSM Error and Coefficient of Determination Statistics

The *coefficient of determination* is 0.97069 and the *root mean square error is* 2.2129 as seen from

Figure 51 above. Since the computed values from the generated response surface are in a close

proximity to the best values, the response surface thus generated can be expected to predict a fairly

good trend for the objective function value. In other words, the model represented by the response

surface would predict the objective value (torque) within an error of 3.532%.

5.3 Optimization Method

The optimization algorithm used in this study employs Nonlinear Programming by

Quadratic Lagrangian (NLPQL) technique based on *Latin Hypercube Sampling* and *Kriging*

Response Surface. This is a gradient based algorithm to provide a refined, global optimization

result. Since, we have a single objective to achieve, this technique is best as it can deal with multiple constraints and aims at finding the global optimum.

Our optimization problem is now reduced to:

Objective: Maximize Torque

Two optimization routines are carried out as following:

Routine 1: The total length of the blade (7.5 m) and the maximum chord (0.749 m) occurring at Station 2 are kept a constant (constrained) with an aim to optimize the existing blade within the length requirements. Figure 51 shows the optimization routine 1 framework.

Table of Schematic F4: Optimization						
A	B	C	D	E	F	G
Name	Parameter	Objective		Constraint		
		Type	Target	Type	Lower Bound	Upper Bound
3 Maximize P12; P12 >= 793.82 J	P12 - Torque	Maximize ▾		Values >= Lower Bound ▾	793.82	

Figure 52: Objective Function and Constraints Settings

Statistics of Optimization are as follows:

Number of LHS Initial Samples = 157

Number of Screening Samples = 157

Number of Starting Points = 157

Maximum Number of Evaluations = 279

Maximum Number of Candidates = 3

Routine 2: The starting point of this routine is taken as the best candidate point of Routine 1 to

begin the search on the response surface. The constraints applied are bounded by the

design space spanning (+ -) 10% from the base value of the design variables P3, P4

and P9. Figure 53 shows the design space for optimization routine 2.

Table of Schematic F4: Optimization				
	A	B	C	D
1	Optimization Domain	Lower Bound	Upper Bound	Starting Value
2	P3 - Chord_Station4	0.3654	0.4466	0.406
3	P4 - Radius_Station4	4.266	5.214	4.74
4	P9 - Twist_Station3	0	10	5

Figure 53: Schematic of Design Space for Optimization Routine 2

Optimization Results

Routine 1: There is no change in the values of design variables P3 and P4 after the

optimization routine 1. But the optimized value of P9 turns out to be 2.66° instead of the baseline

value of 0°. This essentially means that the 7.85% increase in power output from the blade is solely

the result of optimum value of the twist at station 3 (SERI 819 airfoil). As evident from the

optimization results (Figure 54), the baseline design of the blade is highly engineered for maximum

power output.

	A	B		C		D		E		F	G
1	Reference	Name	▼	P3 - Chord_Station4 ▼		P4 - Radius_Station4 ▼		P9 - Twist_Station3 ▼		P12 - Torque (J)	▼
2										Parameter Value	Variation from Reference
3	◉	Starting Point		0.406		4.74		2.665		★★ 856.14	0.00 %
4	○	Candidate Point 1		0.406		4.74		2.6653		★★ 860.94	0.56 %
5	○	Candidate Point 2		0.406		4.74		2.6651		★★ 856.97	0.09 %
6	○	Candidate Point 3		0.406		4.74		2.665		★★ 856.14	0.00 %

Figure 54: Optimized Candidate Points for Optimization Routine 1

Table 6: Table Showing Optimized Candidate Point for Routine 1

Design Variable	Design Variable Base Value	Design Variable Optimized Value
Chord_Station 4 **(P3)**	0.406 m	0.406 m
Radius_Station 4 **(P4)**	4.74 m	4.74 m
Twist_Station 3 **(P9)**	0°	2.66°
Output		
Torque (N.m)	793.820	856.14 (+7.85%)
Power (KW)	16.2099	17.4824 (+7.85%)

The graph (obtained from what-if scenario study) in Figure 55 below is in agreement with the above optimization result. The graph clearly shows that if all the other input parameters are held constant, P9 (Twist_Station 3) at a value of approximately 2.66° gives the maximum blade torque output of about 856.14 Nm. The graph below verifies the optimization routine 1 carried out.
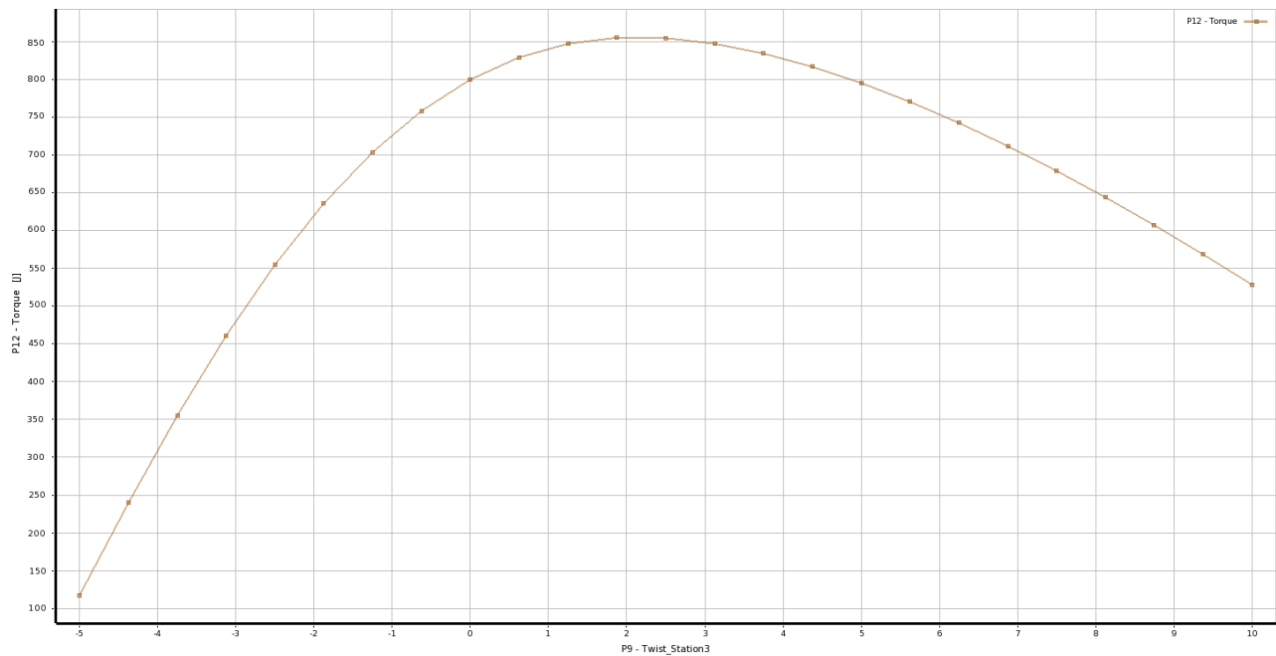
Figure 55: Torque (P12) vs Twist_Station3 (P9) for Optimization Routine 1

Routine 2: There is a change in the values of design variables P3, P4 and P9 after the optimization routine 2. The optimized value of P3 turns out to be 0.43578 m (+7.33%) instead of the baseline value of 0.406 m. Also, the optimized values of P4 and P9 are 5.214 m (+10%) and 2.9549° (+ 10.87%) respectively. This also indicates that the total blade length has been increased by 10%, which results in the augmented power of 1069.5 Nm (+25.26%). Figure 56 below shows the optimized candidate points obtained from optimization routine 2.

Figure 56: Optimized Candidate Points for Optimization Routine 2

Table 7: Table Showing Optimized Candidate Point for Routine 2

Design Variable	Design Variable Base Value	Design Variable Optimized Value
Chord_Station 4 **(P3)**	0.406 m	0.43578 m
Radius_Station 4 **(P4)**	4.74 m	5.214 m
Twist_Station 3 **(P9)**	0°	2.9549°
Output		
Torque (N.m)	853.80	1069.5 (+25.26%)
Power (KW)	17.4346	21.8392 (+25.26%)
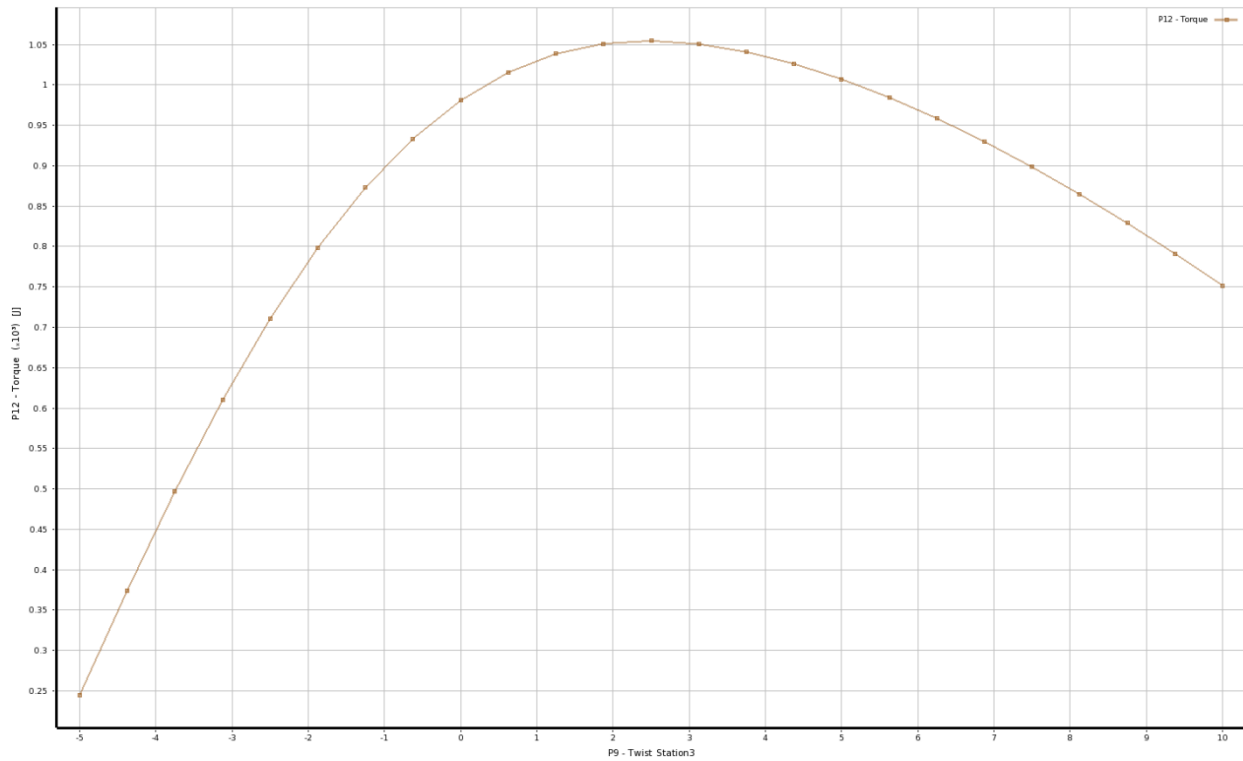
Figure 57: Torque (P12) vs Twist_Station3 (P9) for Optimization Routine 2

The graph (obtained from what-if scenario study) in figure 57 above is in agreement with the above optimization result. The graph clearly shows that if all the other input parameters are held constant, the optimum design values for P3, P4 and P9 (Twist_Station 3) at a value of approximately 2.9° gives the maximum blade torque output of about 1069 Nm. The graph also verifies the optimization routine 2 carried out.

Validation with CFD

Routine 1: The CFD computation was run automatically by the optimizer-solver coupling to gauge the correctness of the optimized candidate point (1). Figure 58 below shows the comparison between the optimized candidate point (1) and the result obtained computationally by the solver. As can be seen, the flow solver computes the torque value to be 853.8 Nm and the optimized prediction value is 856.14 Nm.

The error in the CFD prediction is of the order of 0.274%, which reiterates the robustness of our optimization algorithm in predicting the objective value.

Candidate Points		
	Candidate Point 1	Candidate Point 1 (verified)
P3 - Chord_Station4	0.406	
P4 - Radius_Station4	4.74	
P9 - Twist_Station3	2.665	
P12 - Torque (J)	856.14	853.8

Figure 58: Optimized Result from Routine 1 Verified by CFD

Routine 2: As can be seen from Figure 56, the flow solver computes the torque value to be 1069.5 Nm and the optimized prediction value is 1070.6 Nm. Error in the two values is - 0.102%.

Similar to the validation of the power generated by the baseline design for various wind speeds, the optimized blade was also simulated and the power numerically computed. Figure 59 shows the power curve comparison for the baseline design and the optimized design.

Table 8: Table for Comparison (Baseline to Optimized Results from Optimization Routine 1)

Wind Speed	Obtained Power (kW) from CFD for Baseline Blade	Obtained Power (kW) from CFD for Optimized Blade
5.96	2.7855	3.0712
7	7.1425	7.5
8.03	16.2099	17.4346
10.98	38.895	36.348
12.02	41.904	32
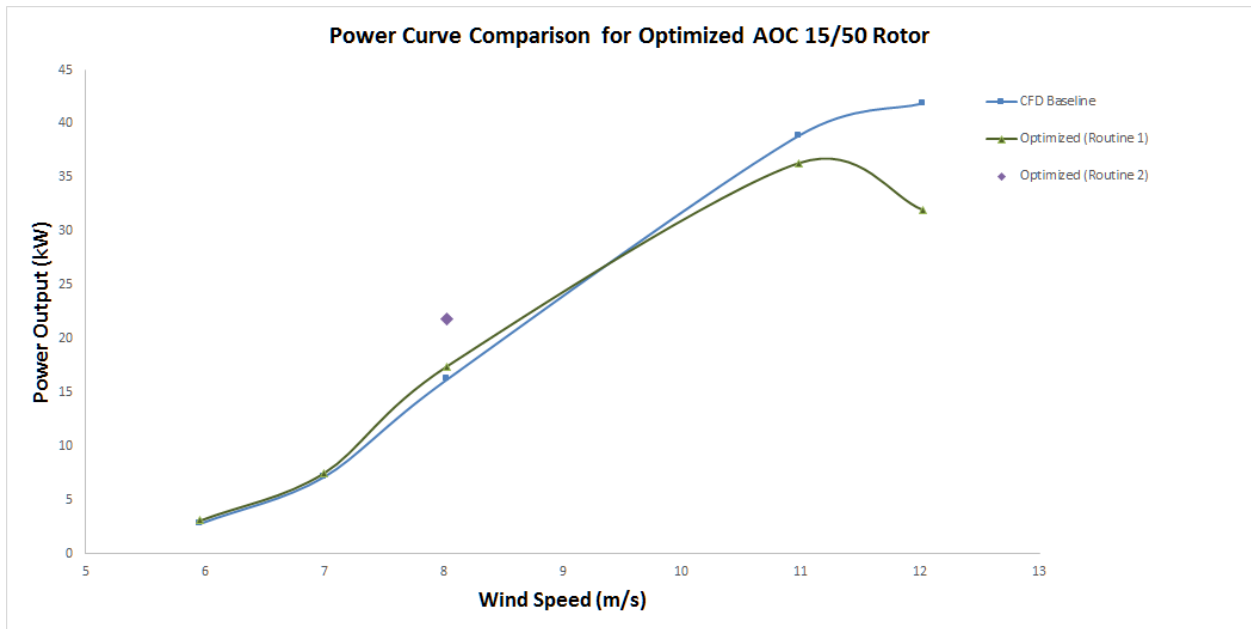
Figure 59: Power Output Curve for Optimized and Baseline Rotor Design

From the above Figure 59, it can be inferred that the optimized blade candidate point (Routine 1) only performs marginally well within the wind speed 5.96 to 7 m/s. The optimized blade design produces the highest power increment at the wind speed of 8.03 m/s, which is 7.55% more than the power of the baseline blade in consideration. The blade's performance increment decreases

further to a wind speed of 9.2 m/s and the blade then underperforms at speeds in excess of 9.2 m/s. This leads us to the conclusion that the blade was only optimized for a given operating condition wind speed of 8.03 m/s and thus is not a global optimum value. The blade optimized design was a local optimum and underperforms over the entire spectrum of wind turbine operation range. Moreover, the blade length has been increased by 10% in the optimization routine 2, hence the power increases to 1069.5 Nm (+25.26%). The chord length P3 has increased by 7.33% and radial section P4 of Station 4 has increased by 10%, thereby increasing the surface area of the blade leading to overall thrust and torque augmentation. As one can expect, the CFD validation of the optimized candidate from routine 2 would exhibit greater torque at all wind speeds.

Validation Using Blade Coefficient of Pressure (C_p) Plots:
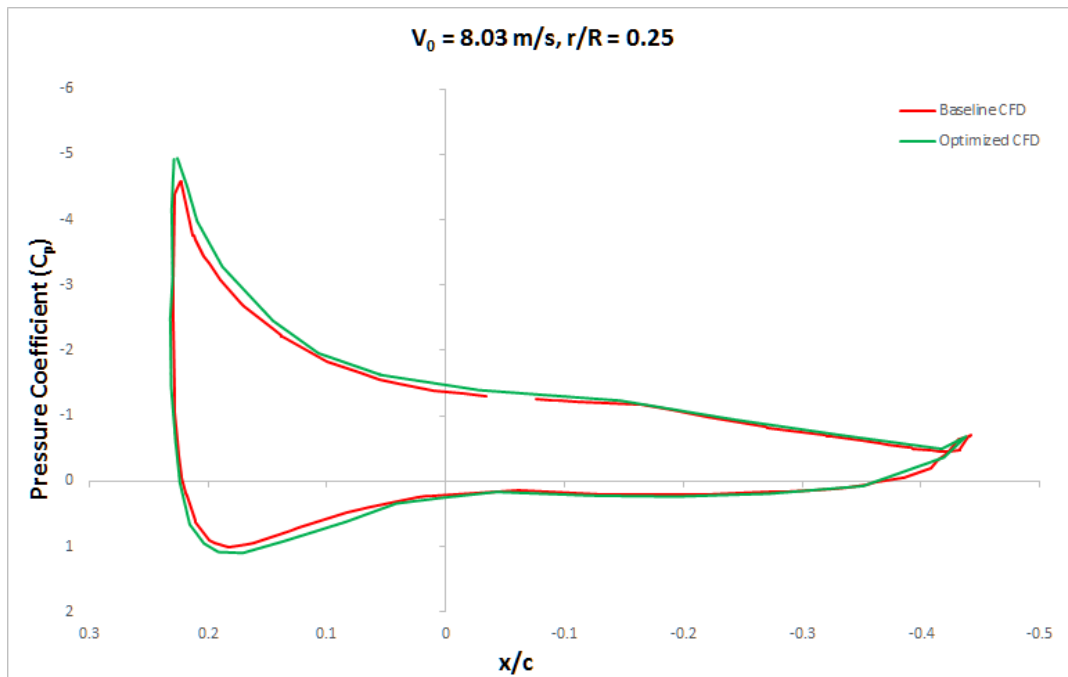
Figure 60: C_p Plot for Optimized Blade at r/R = 0.25
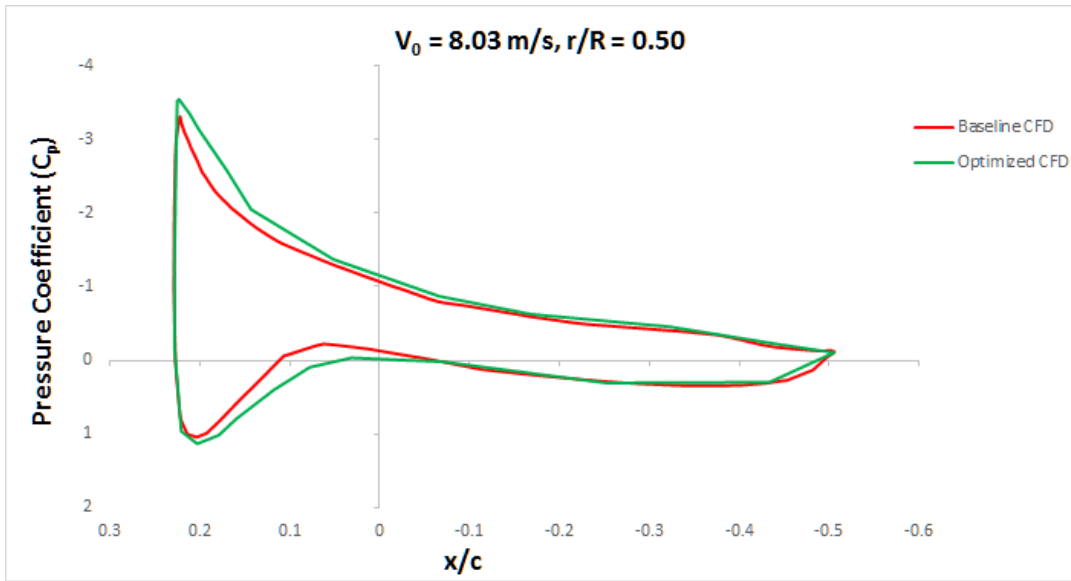
Figure 61: C$_p$ Plot for Optimized Blade at r/R = 0.50
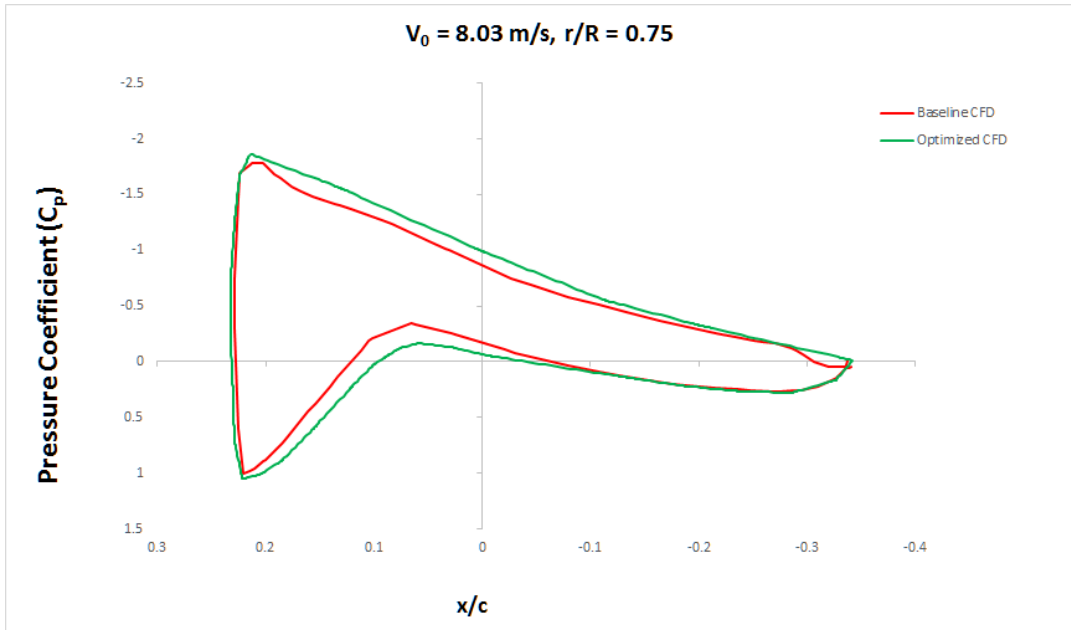
Figure 62: C$_p$ Plot for Optimized Blade at r/R = 0.25

88
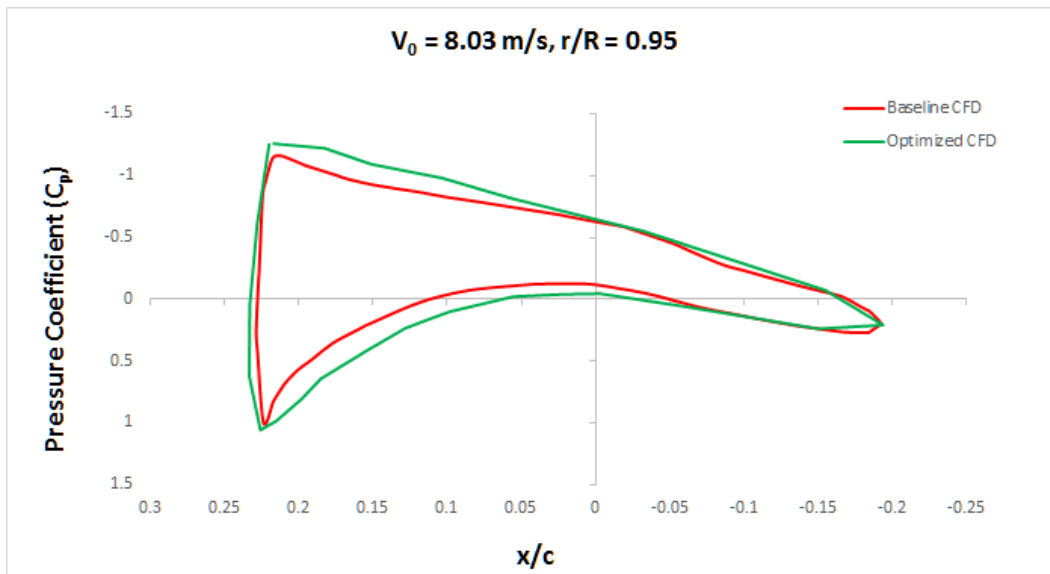
Figure 63: C$_p$ Plot for Optimized Blade at r/R = 0.95

Figures 60-63 above, depict the pressure coefficient plots at different span location over the dimensionless chord along the x coordinate. The coefficient of pressure plots in the figures 60-63 reveal that there is a definite increment in the pressure on the suction and pressure side of the rotor blade at the optimized design configuration simulated at wind speed of 8 m/s. The pressure is less at the suction side while it is more at the pressure side, resulting in increased power output. The optimized blade model seems to have increased the local flow angle of attack. This is clearly indicated at 75% and 95% span location. Finally, most of the mechanical power is produced in the outer 30-40% of the blade.

CHAPTER-6

6.1 Conclusion

In this research, the flow around the airfoils comprising the HAWT blade and the three dimensional rotor blade is established using the commercial solver ANSYS® Fluent. A pressure based compressible flow solver with k-ω SST turbulence model was used for all the flow simulations. To study the dependence (sensitivity) of blade geometric/design parameters (what-if scenario) on the power generated using ANSYS® Fluent, the Design of Experiments (DOE) approach of ANSYS® DesignXplorer was used. Parameter correlation study and sensitivity analysis conducted gave an insight to how the changes in the blade geometry would affect the power output of the blade. The blade aerodynamic optimization inclined toward the non-linear or quadratic relationship between parameters, clearly indicated by the scatter plots and the quadratic determination matrix. This parametric correlation study reveals that the blade design variables on the outer 40% of the blade span have a predominant effect on the power output of the blade. Only the most sensitive design variables are used for the blade optimization problem.

Using the results obtained from CFD simulations, a full quadratic polynomial response surface model (RSM) is constructed, which is then optimized using the Nonlinear Programming by Quadratic Lagrangian (NLPQL) technique to obtain the optimum values of the design variables. For constructing the RSM, the Latin Hypercube Sampling (LHS) design is used to obtain the Design of Experiments (DoE) plan. The main advantage of using this approach for shape optimization problems is that values obtained from commercially available flow solvers can directly be used in the optimization process, without making any changes to the solver's code. Also the noise and non-smoothness issues associated with CFD results are smoothened out by

using the RSM which is quadratic polynomial in terms of the design variables. Thus the optimization process can be performed effectively and smoothly without any sudden divergence issues associated with the CFD results. As evident from the CFD validations carried out on the optimum candidate point, the optimization algorithm generated a design configuration that resulted in a localized optimum design that had increased power output (+7.55%) at wind speed of 8.03 m/s only. The algorithm thus resulted in a local optimum solution rather than a global optimum. Achieving a global optimum solution to this problem would require several data points to be generated for obtaining a complete and well established response surface spanning the entire operating wind spectrum of the turbine, this is a costly affair in terms of the computational resources available. The C_p plots at various span locations also bolster the claim that only the outer (from tip) 30-40% of the blade contributes most towards the power output.

6.2 Recommendations and Future Work

Recommendations for future work include:

I. Grid sensitivity analysis for different turbulence models and different wind speeds. Different grids with different y+ values should be tested to decide on the best turbulence model for wind turbine simulations.

II. There remains a lot of scope for improvement in the optimization methodology that has been employed in this research work. In particular the flow solver and the turbulence model that has been used here can be replaced with higher-fidelity flow solvers that can predict the flow transition from laminar to turbulent more accurately. Laminar-turbulent flow transition prediction plays a vital role in the accuracy of the results, particularly in drag prediction.

III. Also Large-Eddy Simulation (LES), in which the large scale eddies (turbulence) are filtered and resolved, can be employed instead of the RANS equations in which the eddies are time averaged. Thus more accurate results can be obtained.

IV. For the optimization of the response surface model, Genetic Algorithms or Particle Swarm Optimization techniques can be investigated to obtain the optimum values of the design variables, instead of the gradient based optimization method (NLPQL) that has been used here. Using Genetic Algorithms and other similar techniques can improve the chances of locating a global minimum instead of the local minimum that is obtained using gradient based methods.

V. The wind turbine response can be studied throughout the entire wind turbine operating range from the cut-in to cut-out speed in order to achieve a more trained response surface towards obtaining a global optimum solution to the mathematical formulation.

APPENDIX A

CFD Results from ANSYS® Fluent
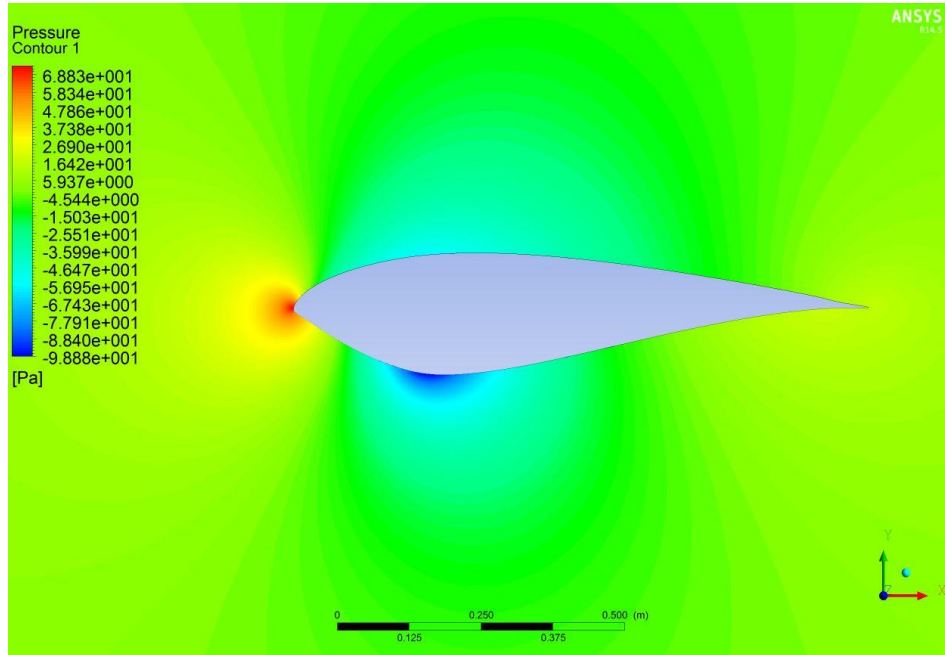
Figure 64: SERI 819 Pressure Contour (AoA 0º)
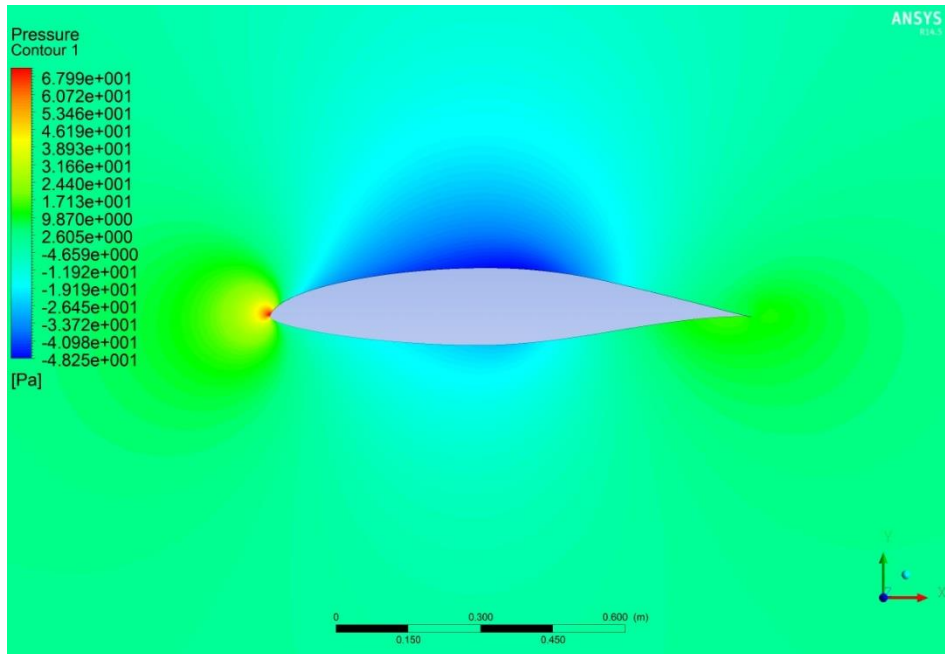
Figure 65: SERI 820 Pressure Contour (AoA 0º)
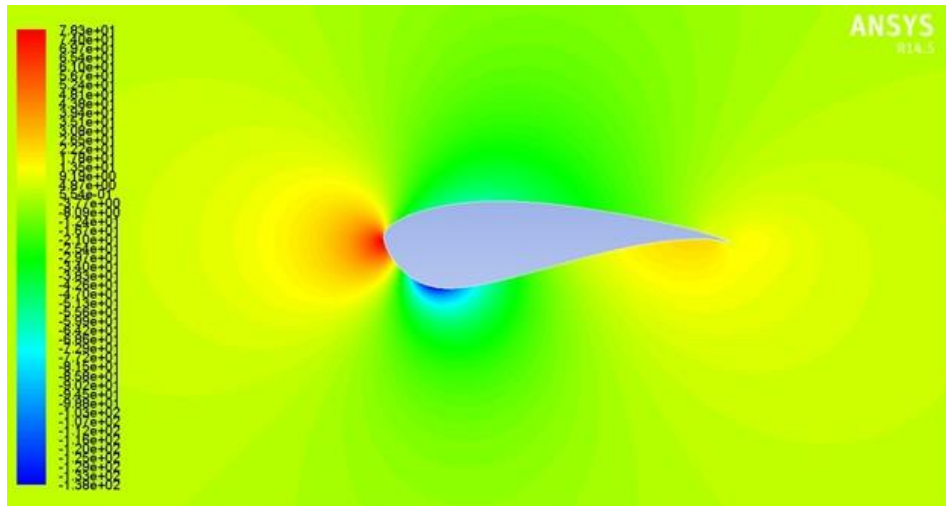
Figure 66: SERI 821 Pressure Contour (AoA 0º)
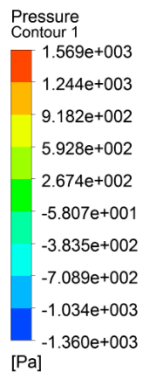
Figure 67: Pressure Side at 5.96 m/s (Baseline)
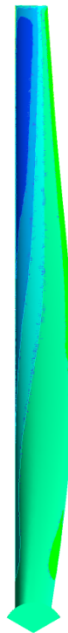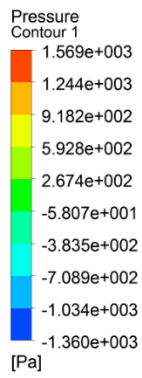
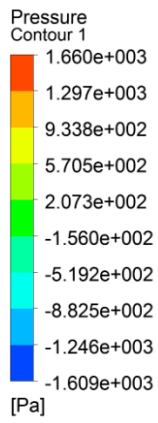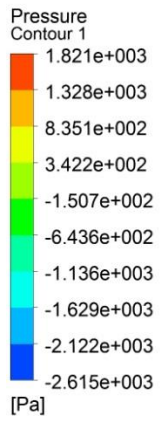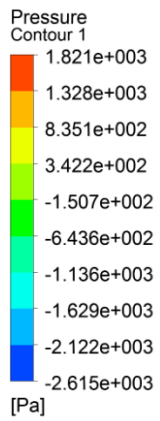*Figure 68: Suction Side at 5.96 m (Baseline)*
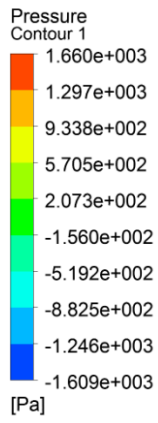
Figure 69: Pressure Side at 7 m/s (Baseline)
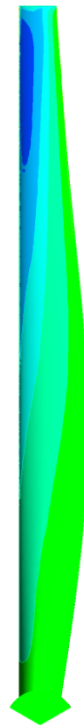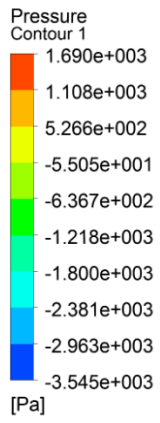

Figure 70: Suction Side at 7 m/s (Baseline)

96

Figure 71: Pressure Side at 8.03 m/s (Baseline)

Figure 72: Suction Side at 8.03 m/s (Baseline)

Figure 73: Pressure Side at 10.98 m/s (Baseline)
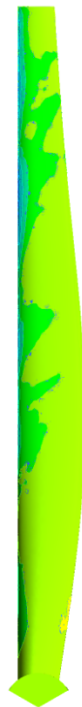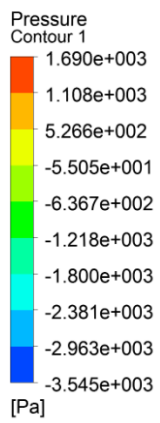
Figure 74: Suction Side at 10.98 m/s (Baseline)
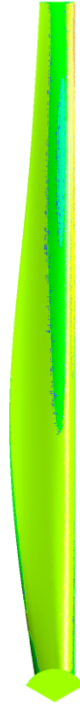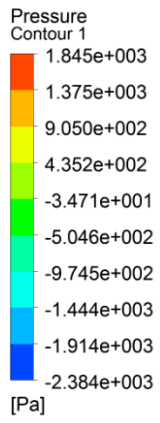
Figure 75: Pressure Side at 8.03 m/s (Optimized Routine 1)
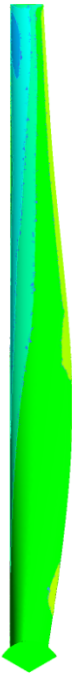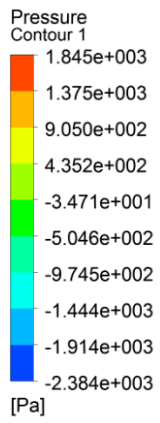
Figure 76: Suction Side at 8.03 m/s (Optimized Routine 1)

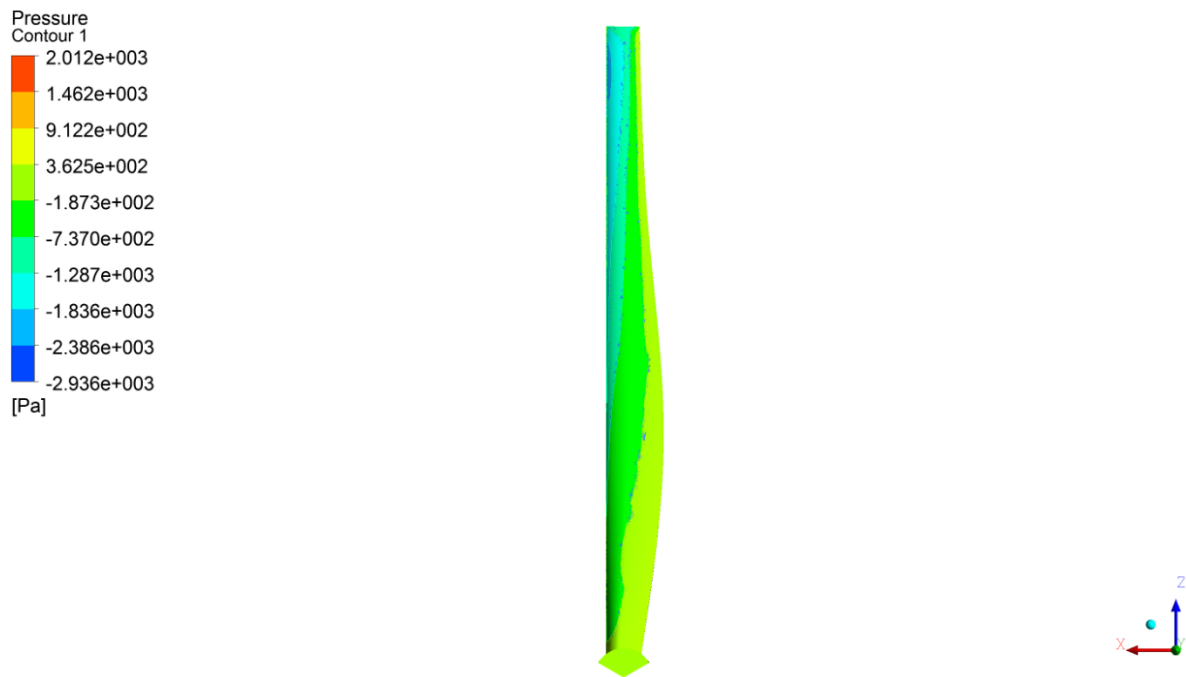*Figure 77: Pressure Side at 8.03 m/s (Optimized Routine 2)*

Figure 78: Suction Side at 8.03 m/s (Optimized Routine 2)

APPENDIX B

Correlation Scatter Plots for the DoE Process
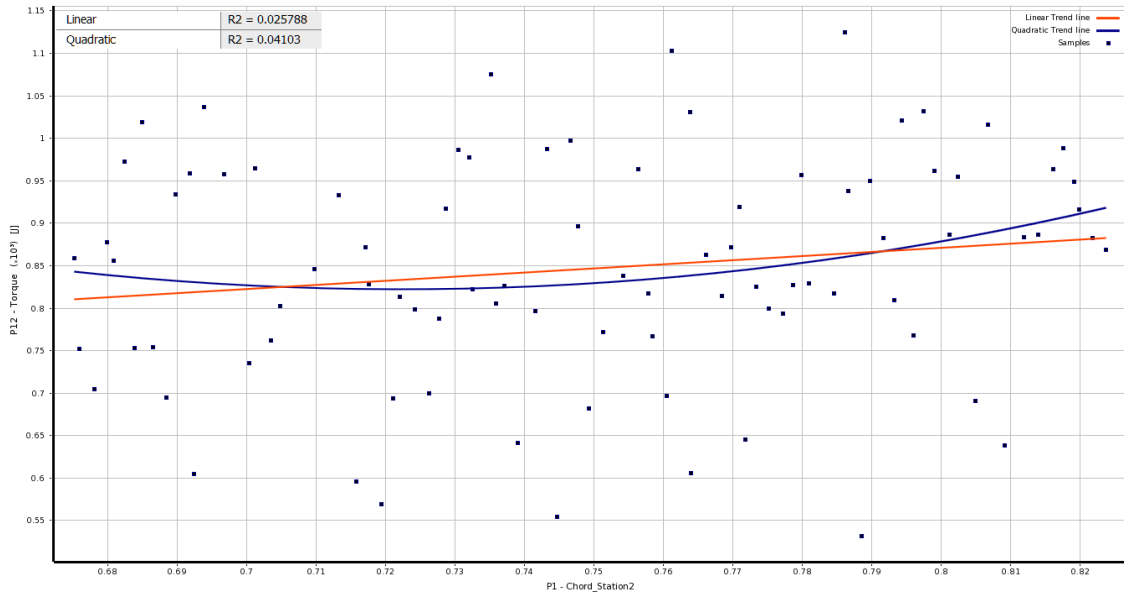

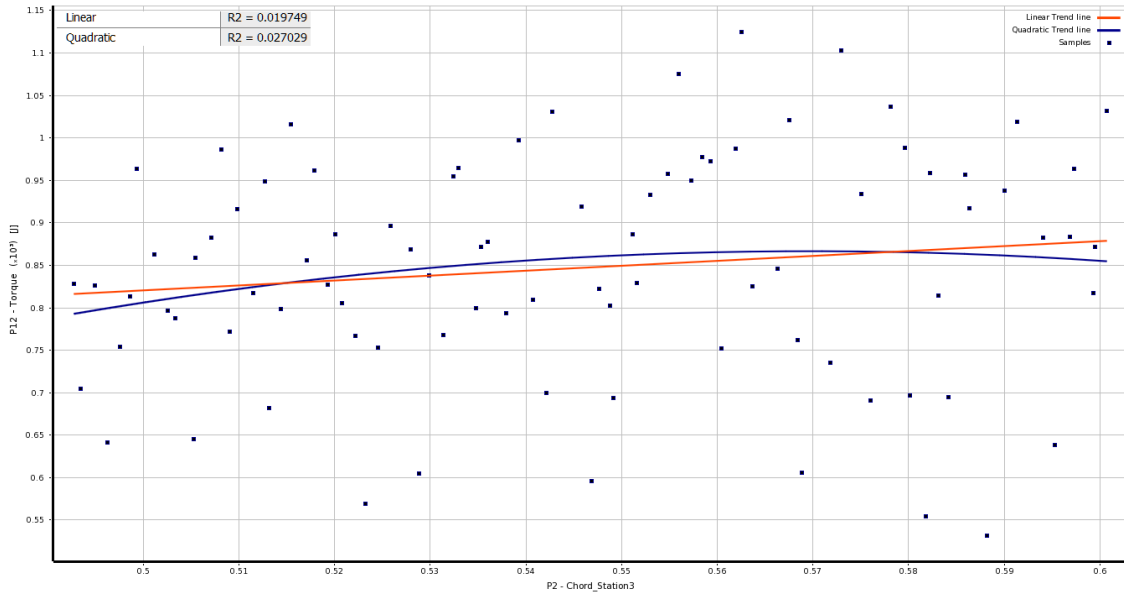*Figure 79: Scatter Plot of Torque (P12) vs Chord_Station2 (P1)*

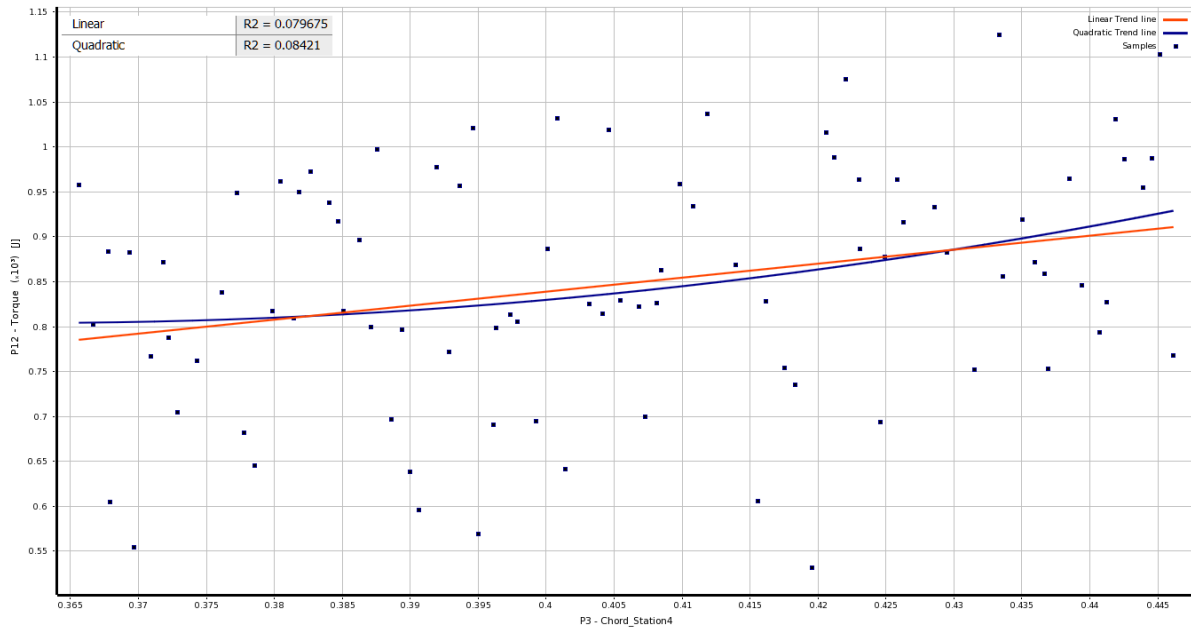*Figure 80: Scatter Plot of Torque (P12) vs Chord_Station3 (P2)*

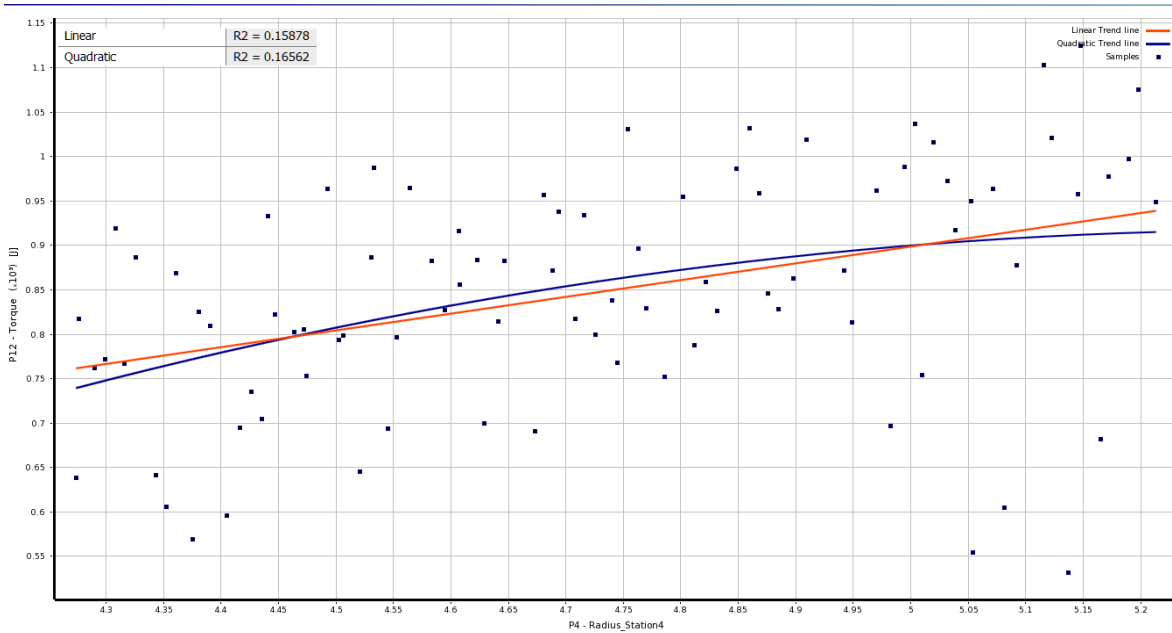*Figure 81: Scatter Plot of Torque (P12) vs Chord_Station4 (P3)*

Figure 82: Scatter Plot of Torque (P12) vs Radius_Station4 (P4)
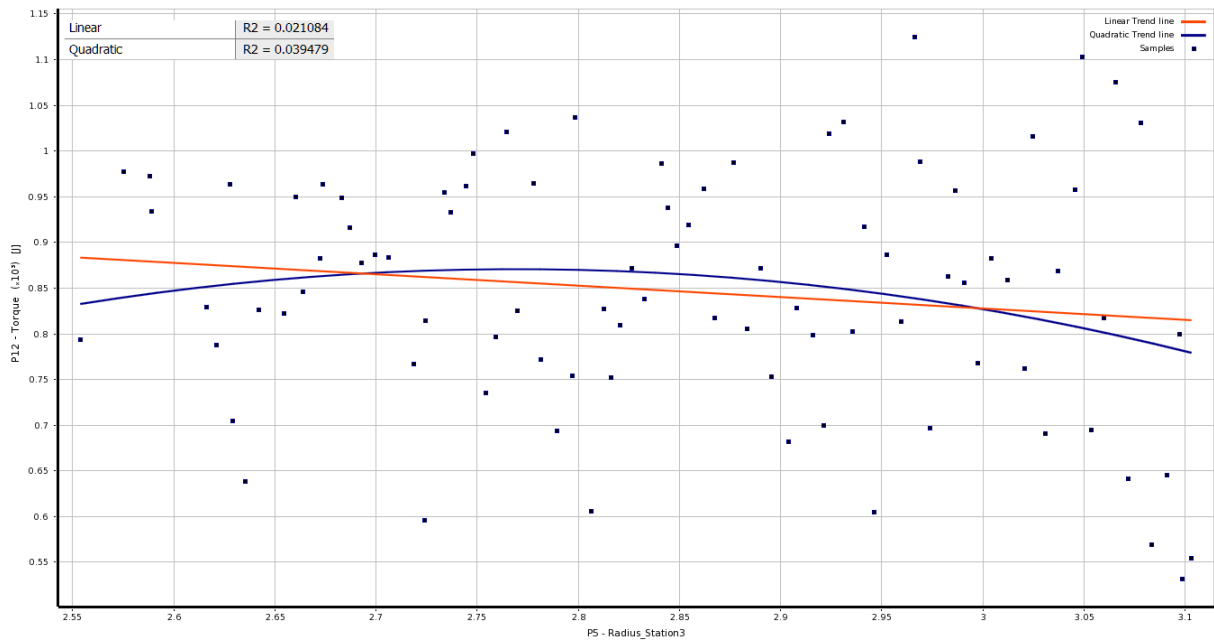
102

Figure 83: Scatter Plot of Torque (P12) vs Radius_Station3 (P5)

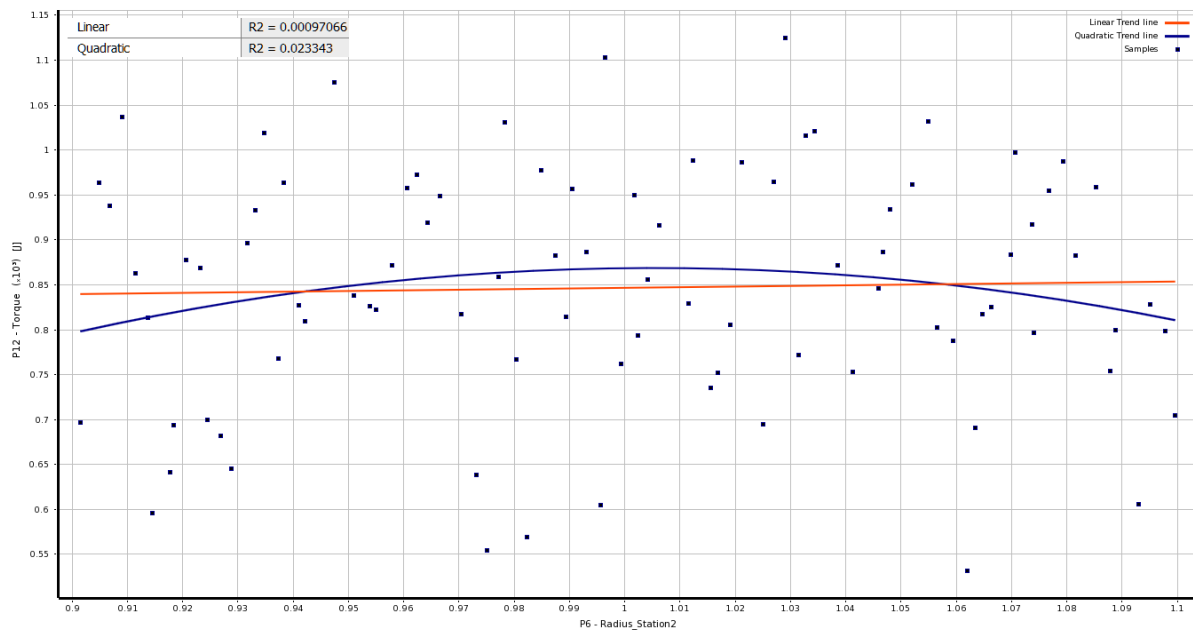*Figure 84: Scatter Plot of Torque (P12) vs Radius_Station2 (P6)*

103

Figure 85: Scatter Plot of Torque (P12) vs Attach Angle (P7)

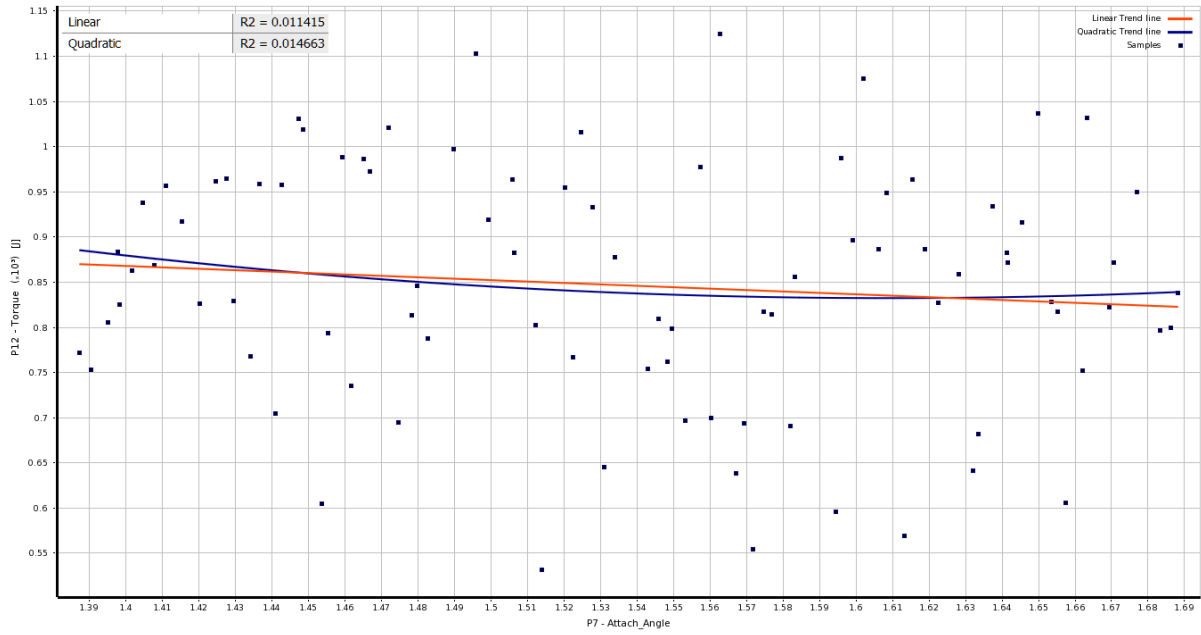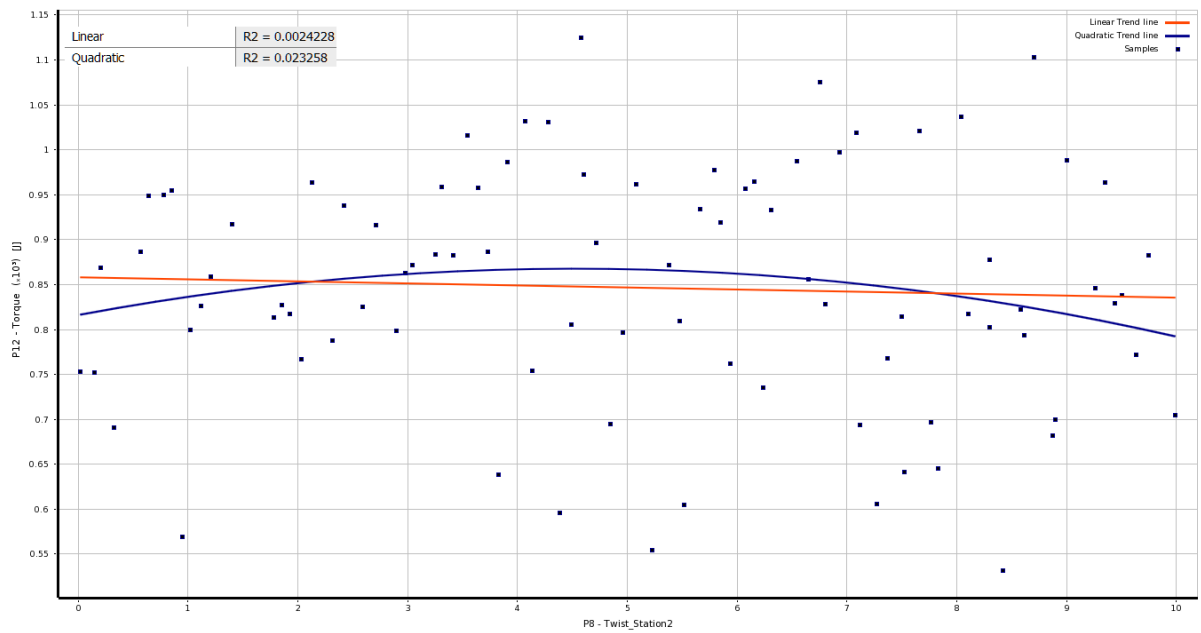*Figure 86: Scatter Plot of Torque (P12) vs Twist_Station2 (P8)*
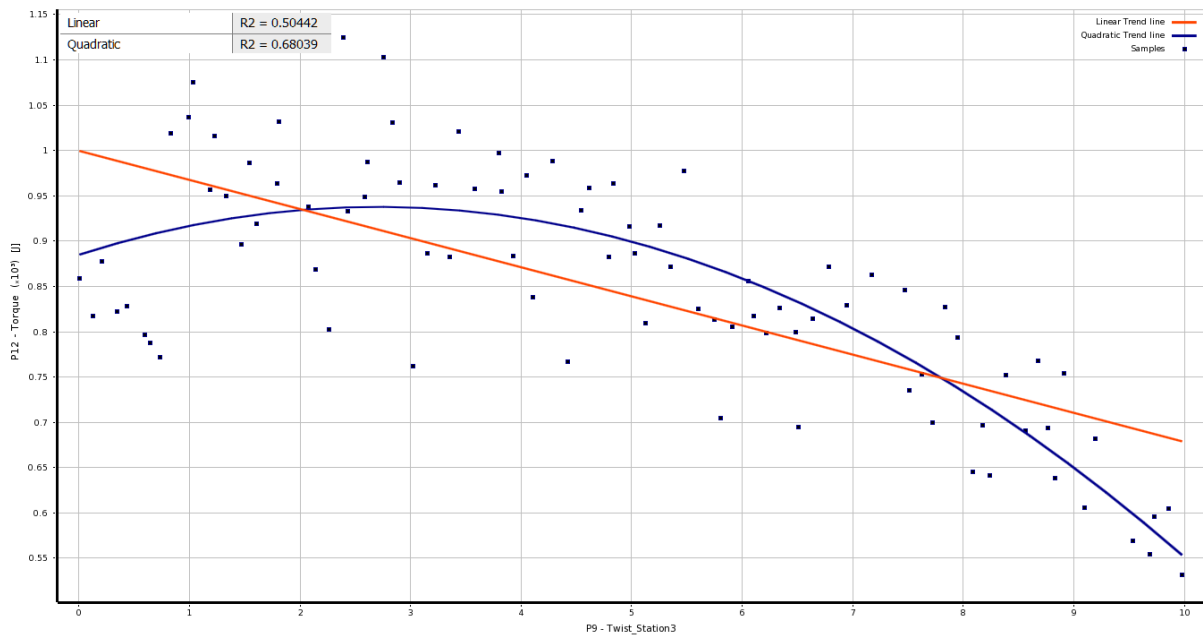
Figure 87: Scatter Plot of Torque (P12) vs Twist_Station3 (P9)
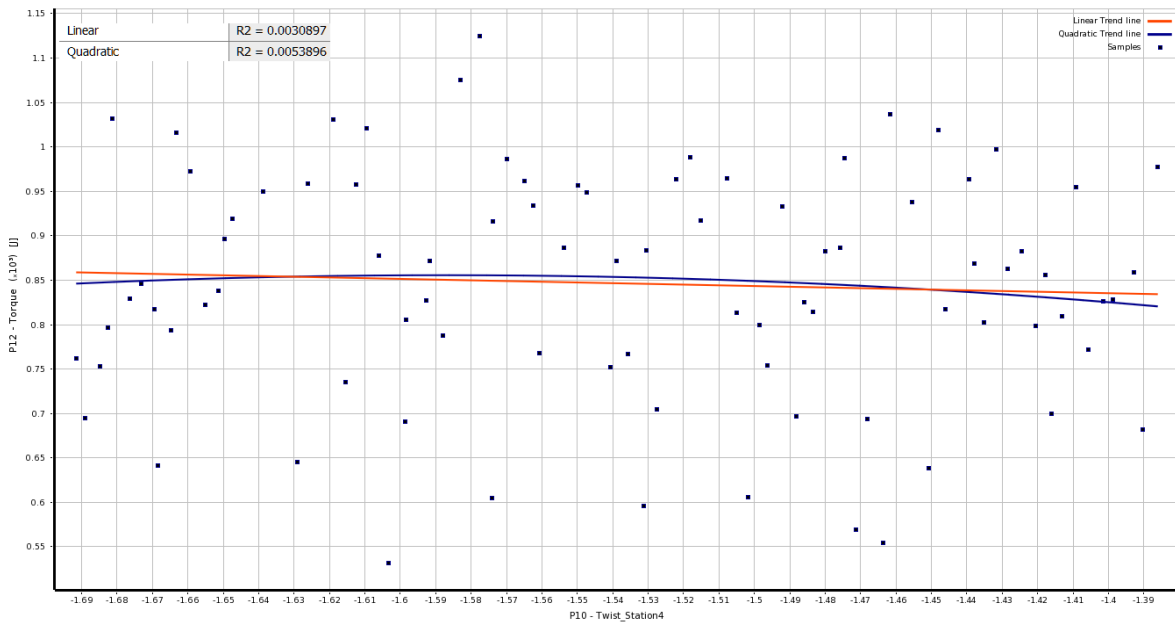
Figure 88: Scatter Plot of Torque (P12) vs Twist_Station4 (P10)
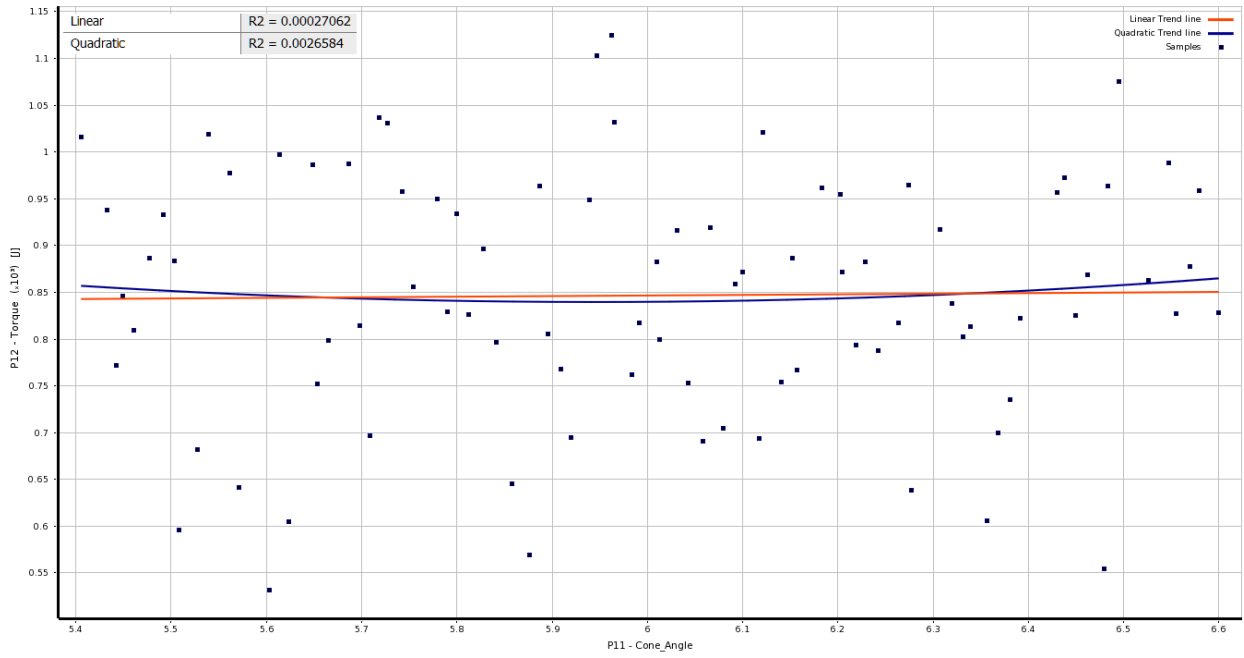
Figure 89: Scatter Plot of Torque (P12) vs Cone Angle (P11)

APPENDIX C

Output Vs Input "What If" Study Graphs
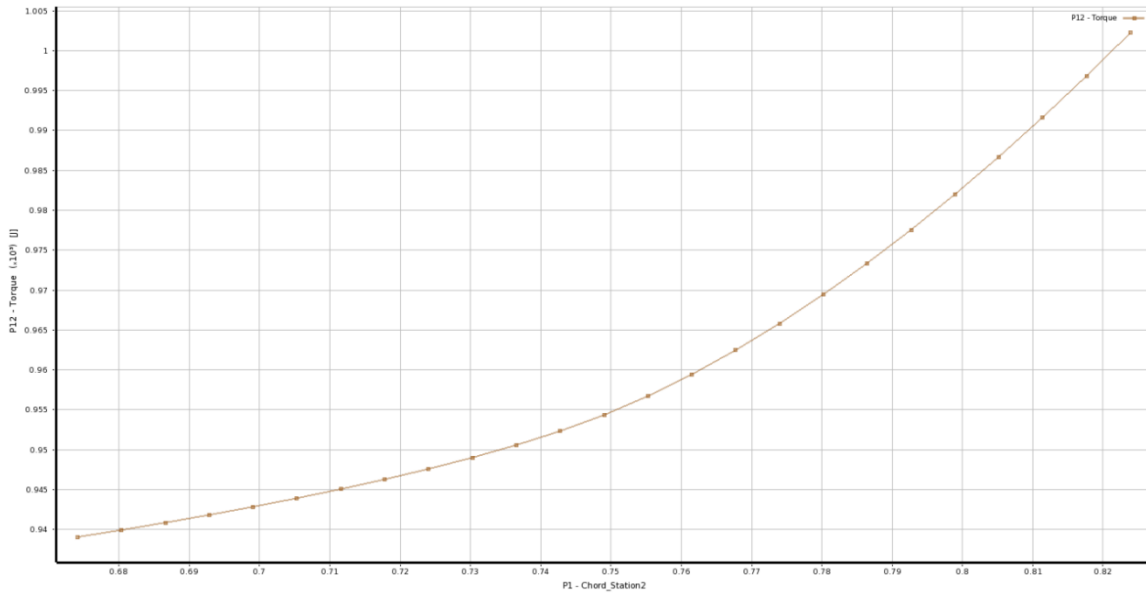
Figure 90: Torque (P12) vs Chord_Station2 (P1)
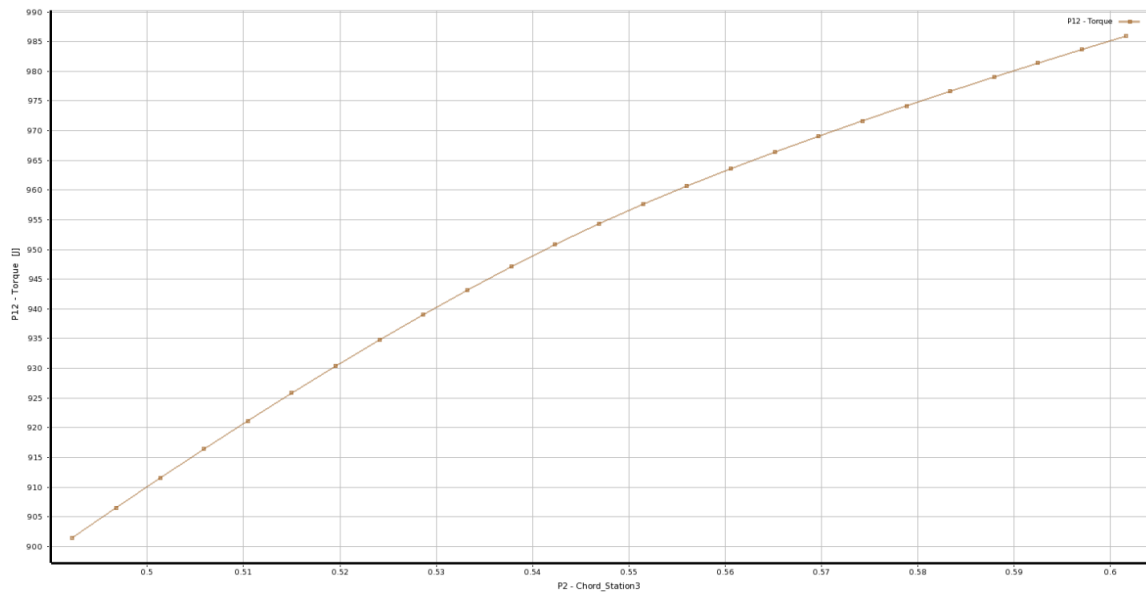
Figure 91: Torque (P12) vs Chord_Station3 (P2)

Figure 92: Torque (P12) vs Chord_Station4 (P3)

Figure 93: Torque (P12) vs Radius_Station4 (P4)

Figure 94: Torque (P12) vs Radius_Station3 (P5)
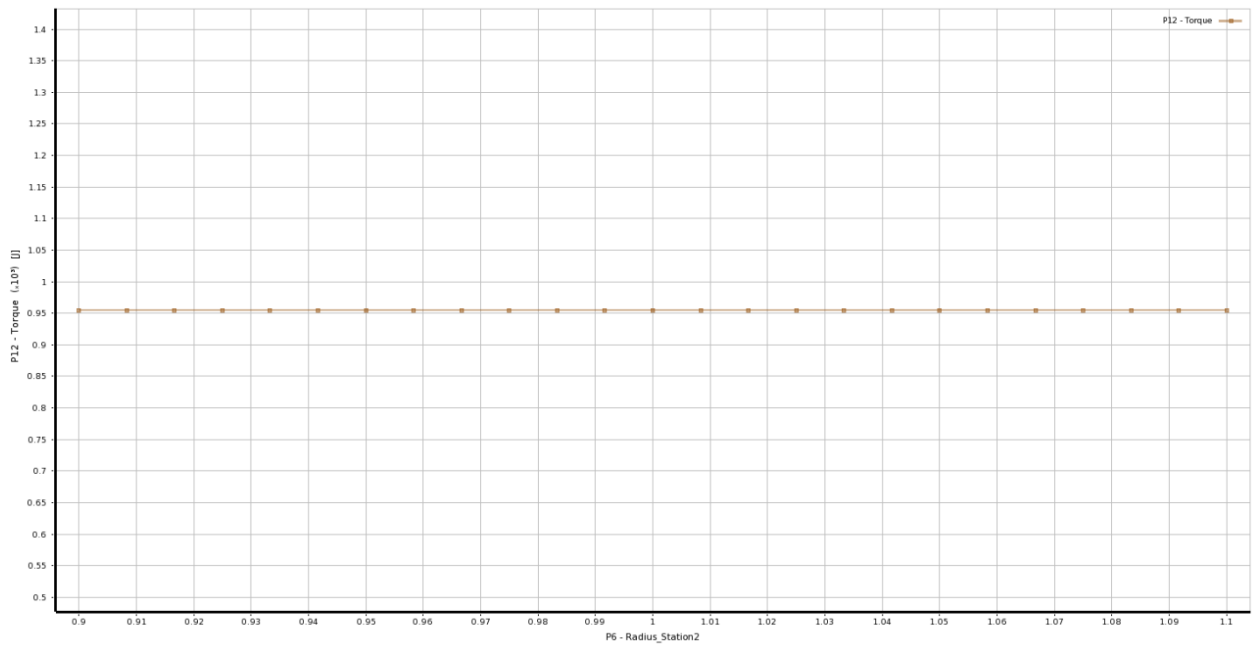
Figure 95: Torque (P12) vs Radius_Station2 (P6)
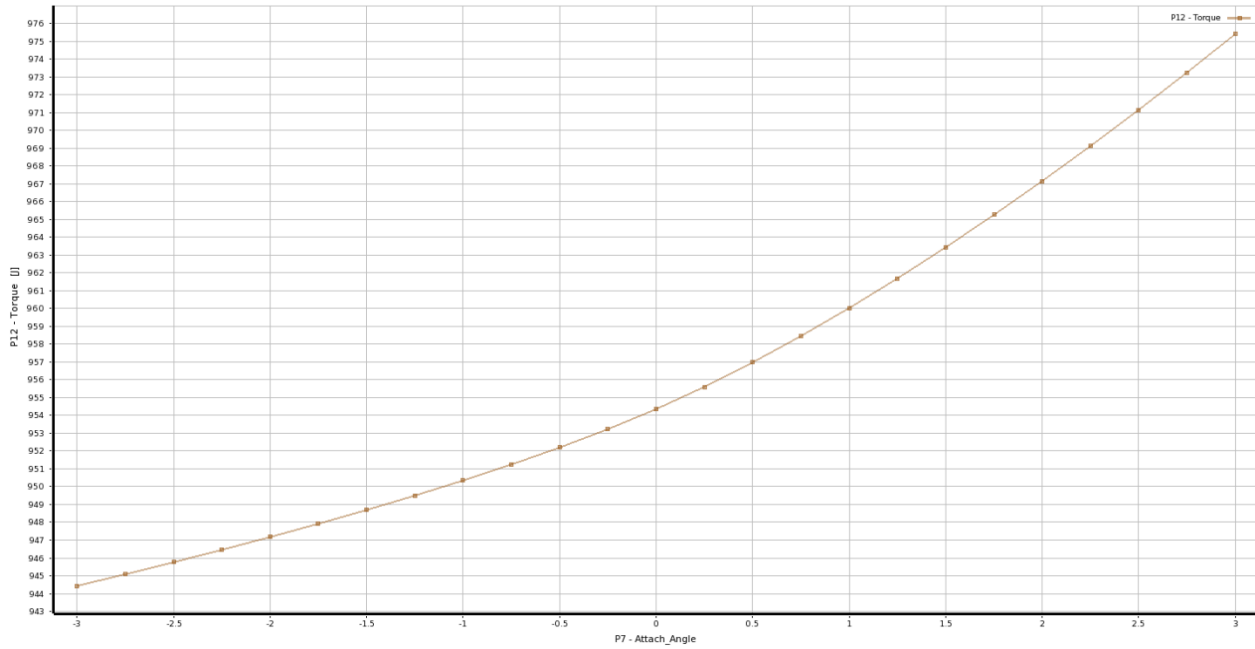
Figure 96: Torque (P12) vs Attach Angle (P7)
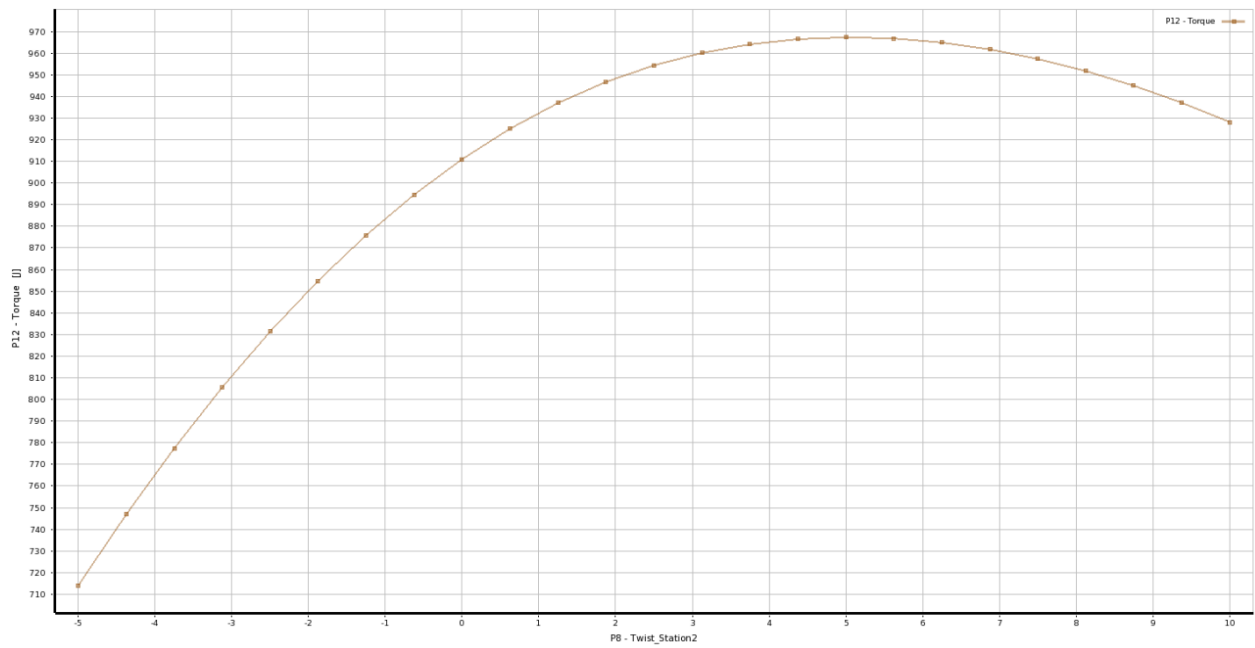
Figure 97: Torque (P12) vs Twist_Station2 (P8)

110
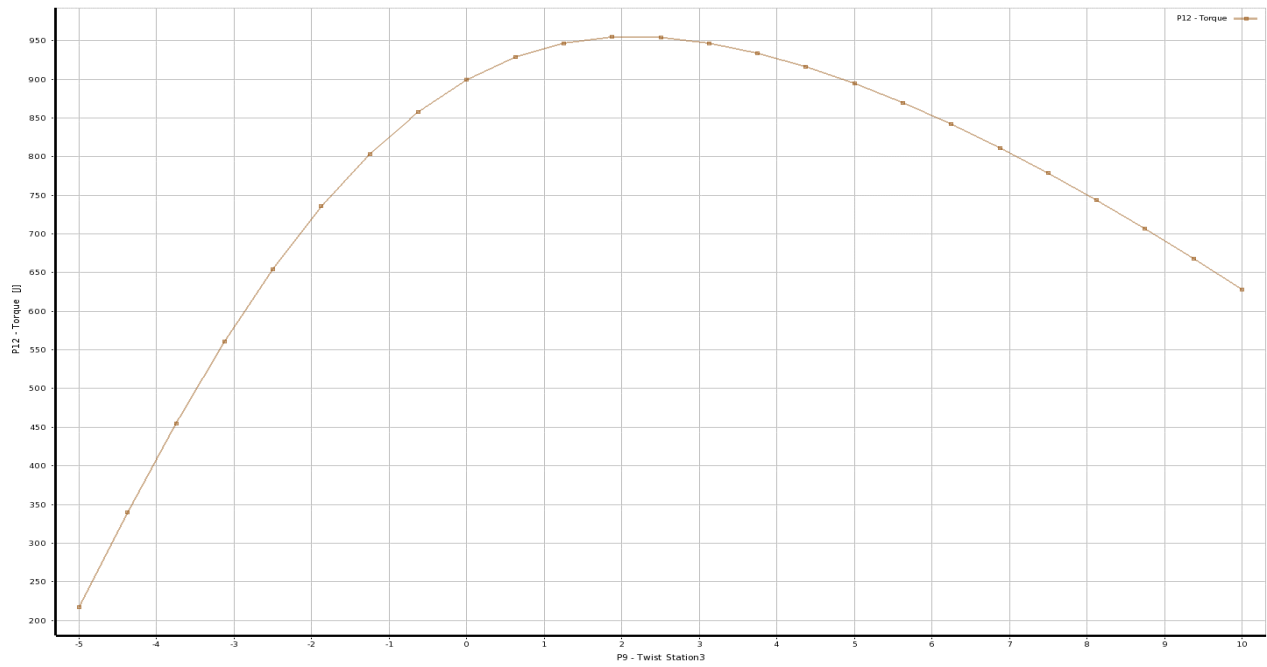
Figure 98: Torque (P12) vs Twist_Station3 (P9)
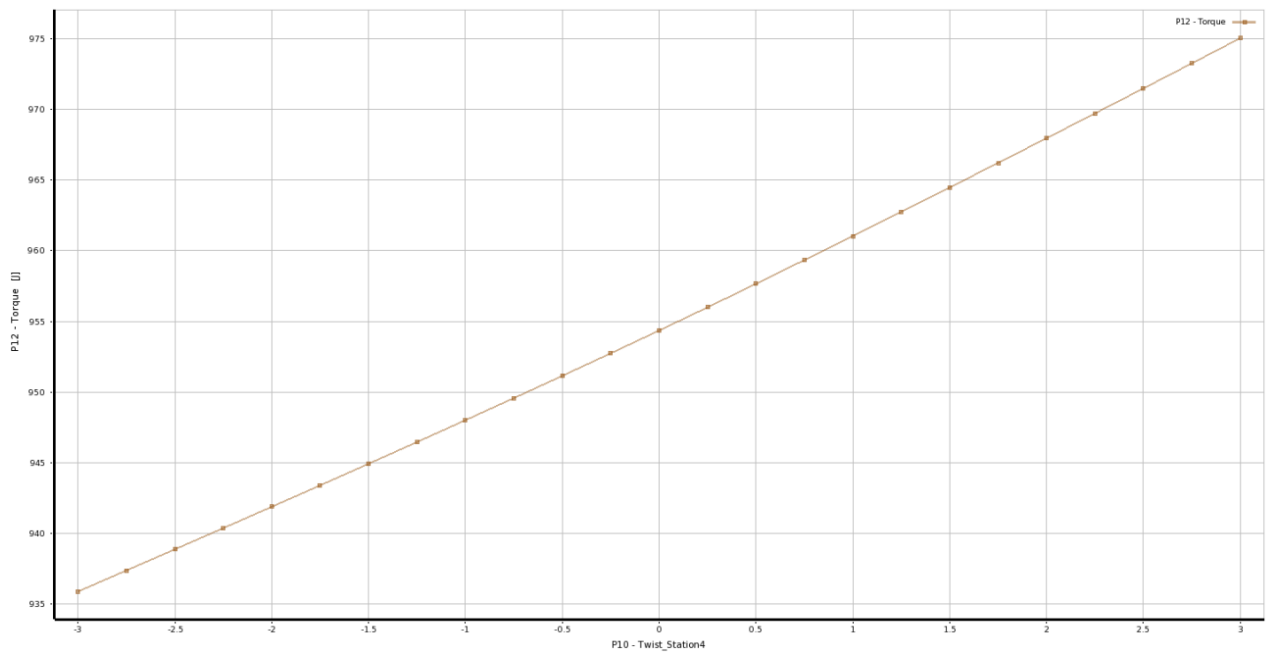
Figure 99: Torque (P12) vs Twist_Station4 (P10)

111

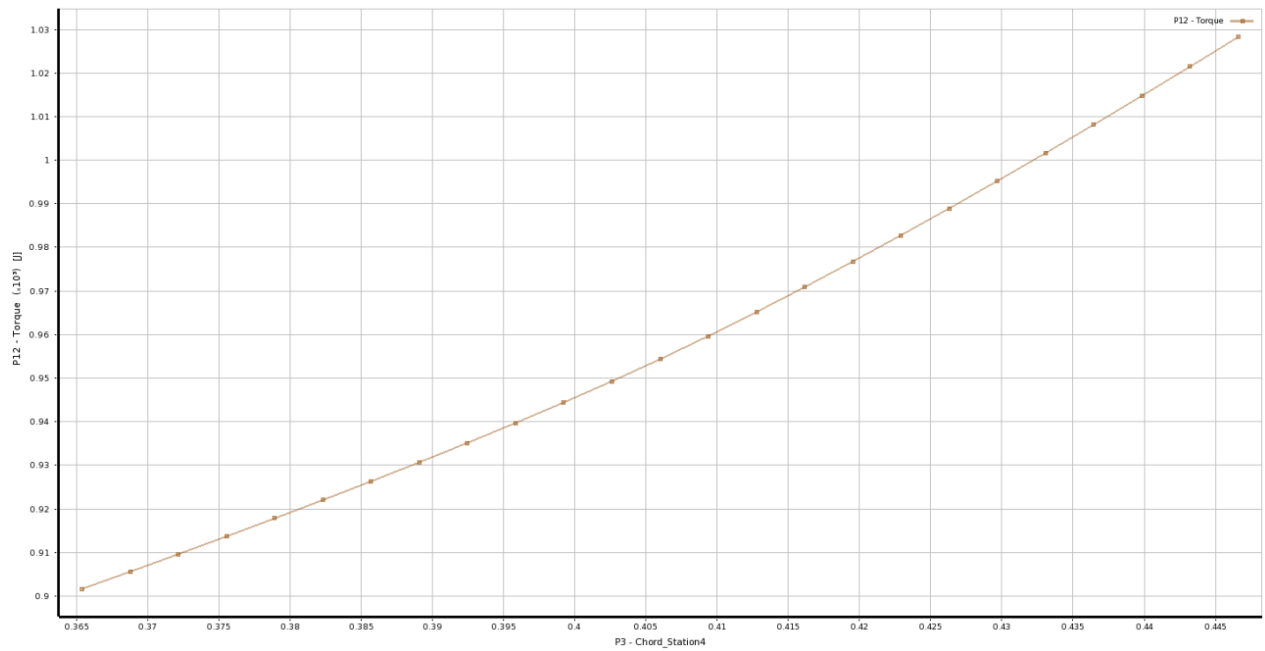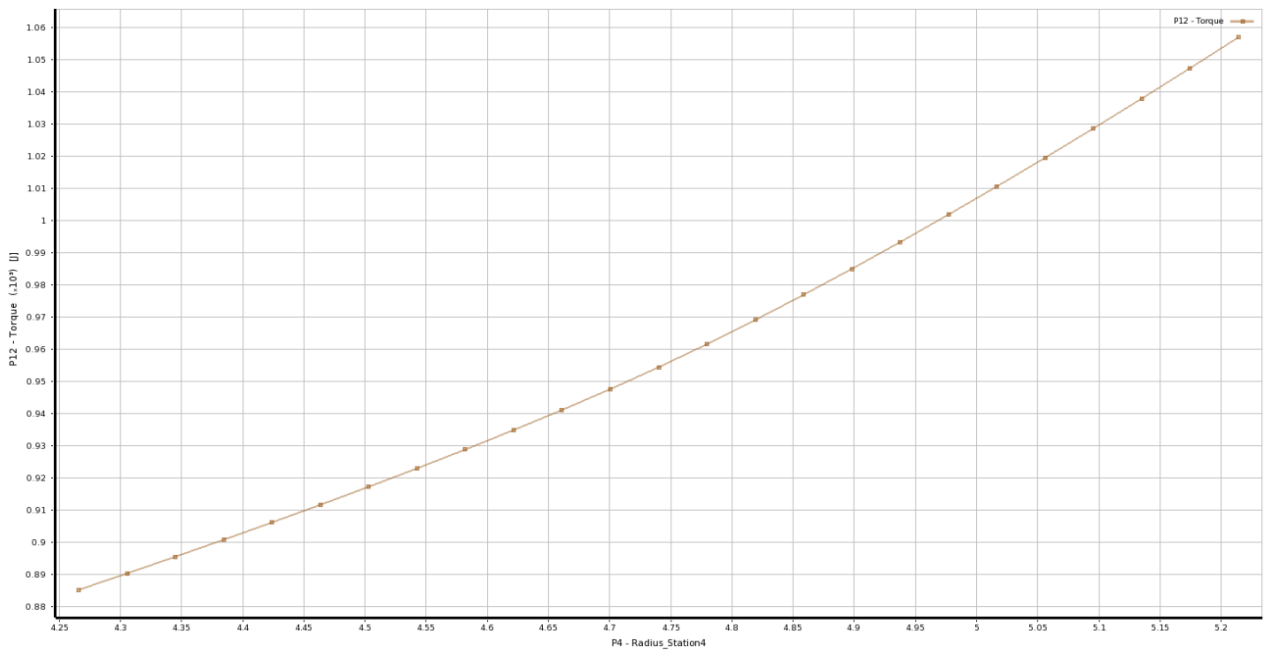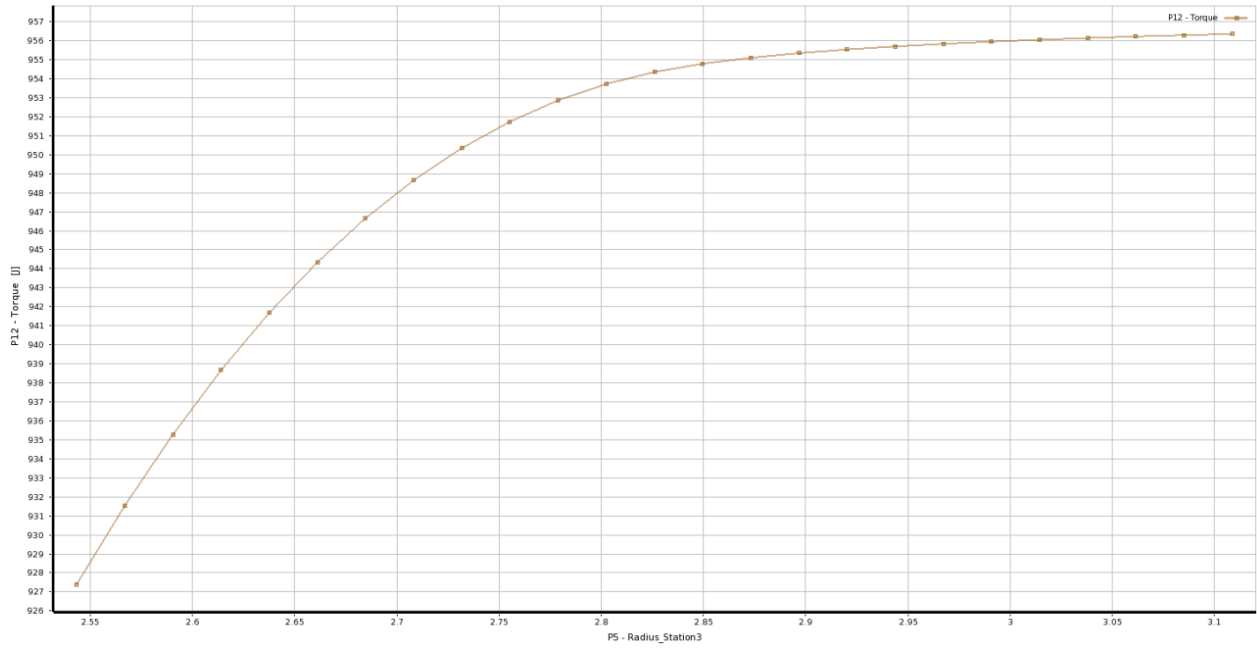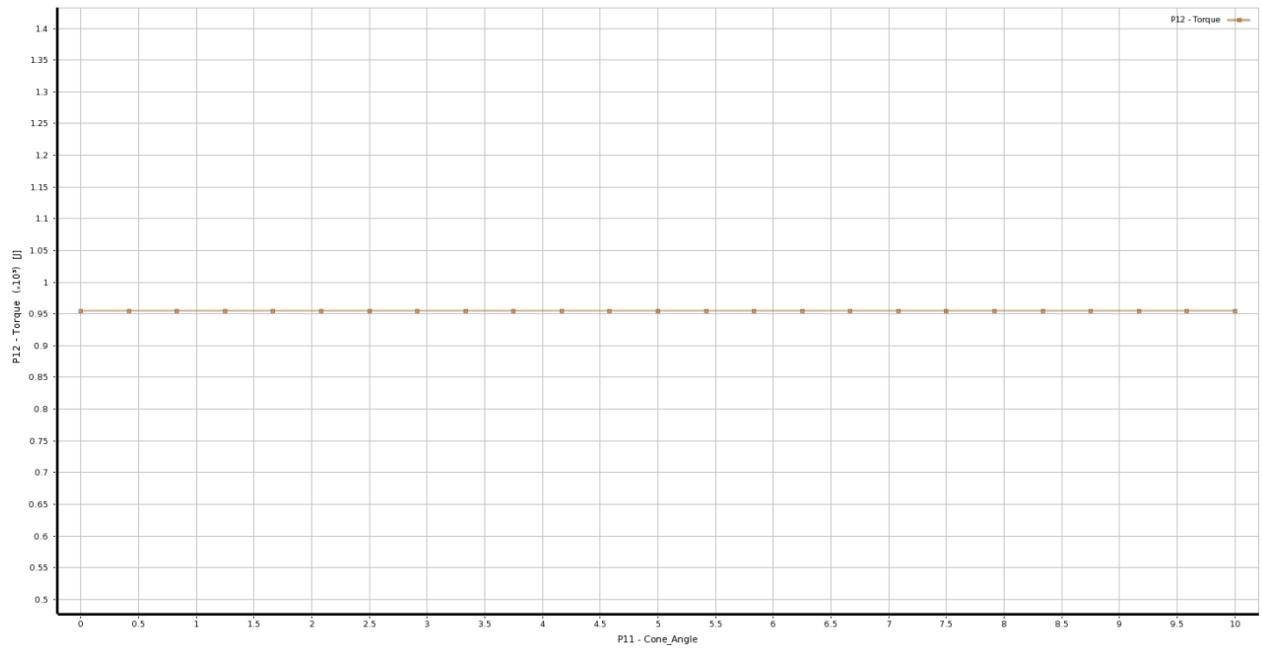*Figure 100: Torque (P12) vs Cone Angle (P11)*

APPENDIX D

S819 Airfoil Coordinate Data

Upper Surface		Lower Surface	
x/c	y/c	x/c	y/c
0.00002	0.00077	0.00006	−0.00125
.00101	.00556	.00056	−.00298
.00673	.01572	.00177	−.00455
.01719	.02663	.00372	−.00622
.03213	.03768	.00891	−.00986
.05143	.04852	.02445	−.02021
.07486	.05890	.04415	−.03323
.10216	.06858	.06692	−.04746
.13302	.07733	.09234	−.06201
.16709	.08491	.11997	−.07614
.20398	.09099	.14948	−.08914
.24355	.09516	.18049	−.10033
.28581	.09736	.21265	−.10864
.33053	.09777	.24658	−.11280
.37732	.09651	.28355	−.11284
.42580	.09369	.32385	−.10966
.47552	.08949	.36718	−.10375
.52602	.08411	.41332	−.09557
.57678	.07780	.46189	−.08562
.62723	.07078	.51244	−.07440
.67679	.06331	.56446	−.06247
.72481	.05561	.61728	−.05039
.77067	.04792	.67018	−.03869
.81370	.04039	.72231	−.02789
.85327	.03316	.77274	−.01843
.88875	.02622	.82050	−.01064
.91979	.01940	.86454	−.00473
.94642	.01282	.90387	−.00075
.96851	.00712	.93753	.00141
.98545	.00295	.96464	.00197
.99626	.00066	.98437	.00136
1.00000	.00000	.99613	.00042
		1.00000	.00000
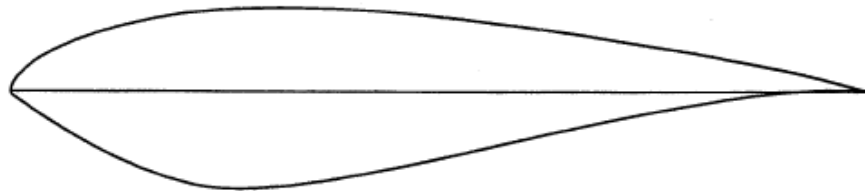
(a) S819.

S820 Airfoil Coordinate Data

Upper Surface		Lower Surface	
x/c	y/c	x/c	y/c
0.00013	0.00133	0.00001	−0.00041
.00364	.00910	.00032	−.00178
.01172	.01811	.00117	−.00300
.02425	.02758	.00258	−.00423
.04120	.03708	.01207	−.00946
.06255	.04637	.02754	−.01514
.08815	.05531	.04834	−.02097
.11774	.06379	.07403	−.02684
.15102	.07167	.10419	−.03260
.18764	.07884	.13841	−.03813
.22719	.08520	.17622	−.04330
.26923	.09063	.21715	−.04798
.31330	.09501	.26072	−.05203
.35891	.09825	.30638	−.05533
.40555	.10022	.35360	−.05772
.45272	.10079	.40183	−.05903
.49988	.09978	.45050	−.05900
.54666	.09688	.49923	−.05721
.59300	.09196	.54807	−.05340
.63875	.08518	.59707	−.04785
.68373	.07668	.64604	−.04093
.72795	.06688	.69476	−.03316
.77109	.05656	.74277	−.02532
.81244	.04635	.78923	−.01803
.85123	.03666	.83325	−.01172
.88668	.02775	.87388	−.00668
.91818	.01962	.91020	−.00304
.94544	.01242	.94132	−.00077
.96806	.00661	.96644	.00029
.98531	.00263	.98490	.00047
.99624	.00057	.99620	.00020
1.00000	.00000	1.00000	.00000

(b) S820.

S821 Airfoil Coordinate Data

Upper Surface		Lower Surface	
x/c	y/c	x/c	y/c
0.00004	0.00203	0.00001	−0.00076
.00037	.00550	.00243	−.01654
.00110	.00874	.00887	−.03393
.00234	.01186	.01876	−.05219
.00405	.01499	.03170	−.07058
.01212	.02520	.04745	−.08838
.02684	.03773	.06576	−.10493
.04636	.04980	.08643	−.11944
.07040	.06118	.10959	−.13110
.09865	.07171	.13548	−.13943
.13075	.08122	.16433	−.14399
.16633	.08955	.19663	−.14462
.20495	.09652	.23262	−.14170
.24618	.10190	.27216	−.13552
.28970	.10538	.31514	−.12635
.33539	.10684	.36142	−.11455
.38300	.10642	.41081	−.10062
.43214	.10431	.46300	−.08518
.48234	.10066	.51756	−.06893
.53312	.09566	.57389	−.05266
.58396	.08955	.63119	−.03717
.63429	.08254	.68850	−.02322
.68353	.07489	.74465	−.01147
.73105	.06680	.79836	−.00239
.77624	.05851	.84823	.00376
.81848	.05016	.89291	.00700
.85715	.04192	.93109	.00763
.89164	.03377	.96165	.00615
.92166	.02552	.98346	.00340
.94740	.01733	.99601	.00093
.96886	.00996	1.00000	.00000
.98550	.00432		
.99625	.00102		
1.00000	.00000		
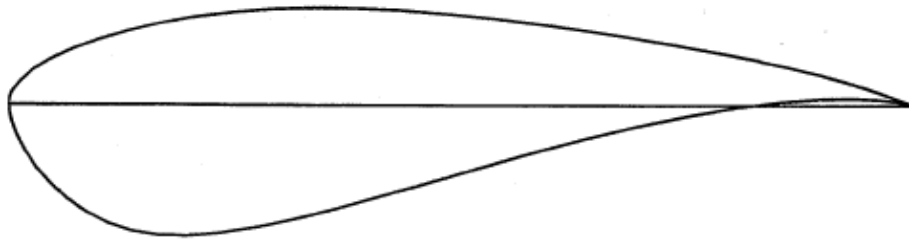
(c) S821.

APPENDIX E

<u>Optimized Blade Design from Optimization Routine 2</u>
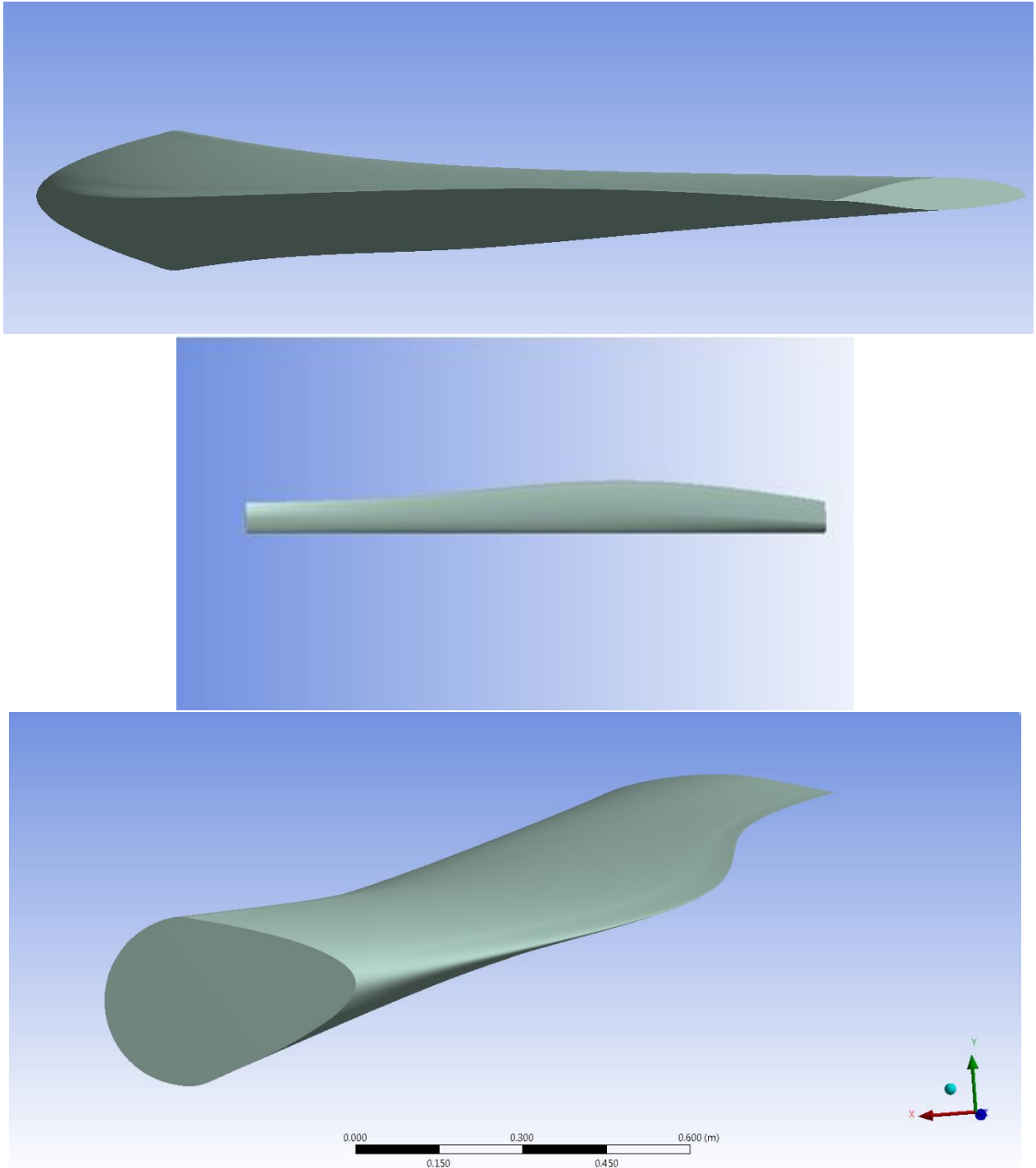
Figure 101: Optimized Blade Profile from Optimization Routine 2

APPENDIX F

Tradeoff of Design Variables and its Plots

Tradeoff between torque and sample points of different design variables are displayed in the following scatter plots colored by Pareto Front. The hollow gray circles highlight infeasible points, while green colored points signify the feasible region with darker shades of blue defining most suitable candidate points as per the optimization routine carried out.
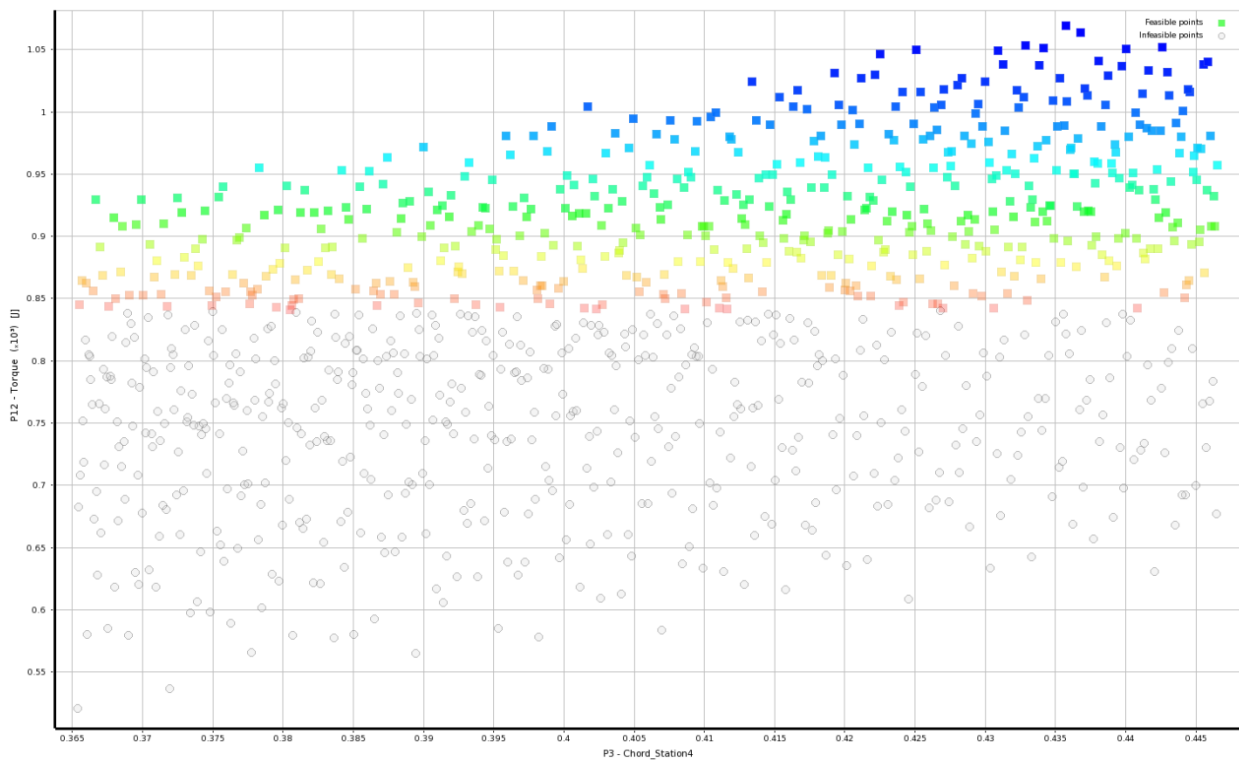
Figure 102: Tradeoff Plot for P3 (Chord_Station4) vs P12 (Torque)
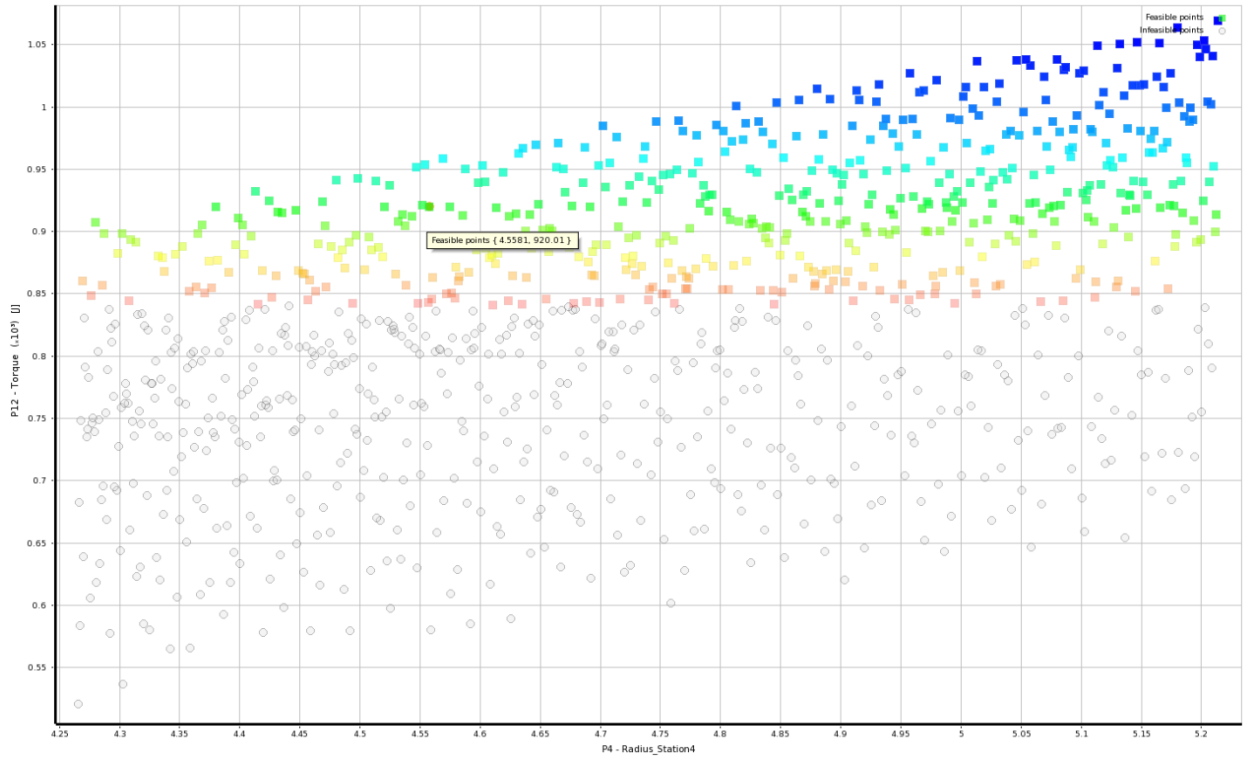
Figure 103: Tradeoff Plot for P4 (Radius_Station4) vs P12 (Torque)

Figure 104: Tradeoff Plot for P9 (Twist_Station3) vs P12 (Torque)

118

APPENDIX G

Description of AOC 15/50 Wind Turbine

The AOC 15/50 test turbine is shown in Figure 103 and its specifications are listed in Table 8. NREL designates the turbine configuration for this test as "AOC B"

Figure 105: AOC 15/50 Test Turbine [10]

Test Turbine Configuration and Operational Data

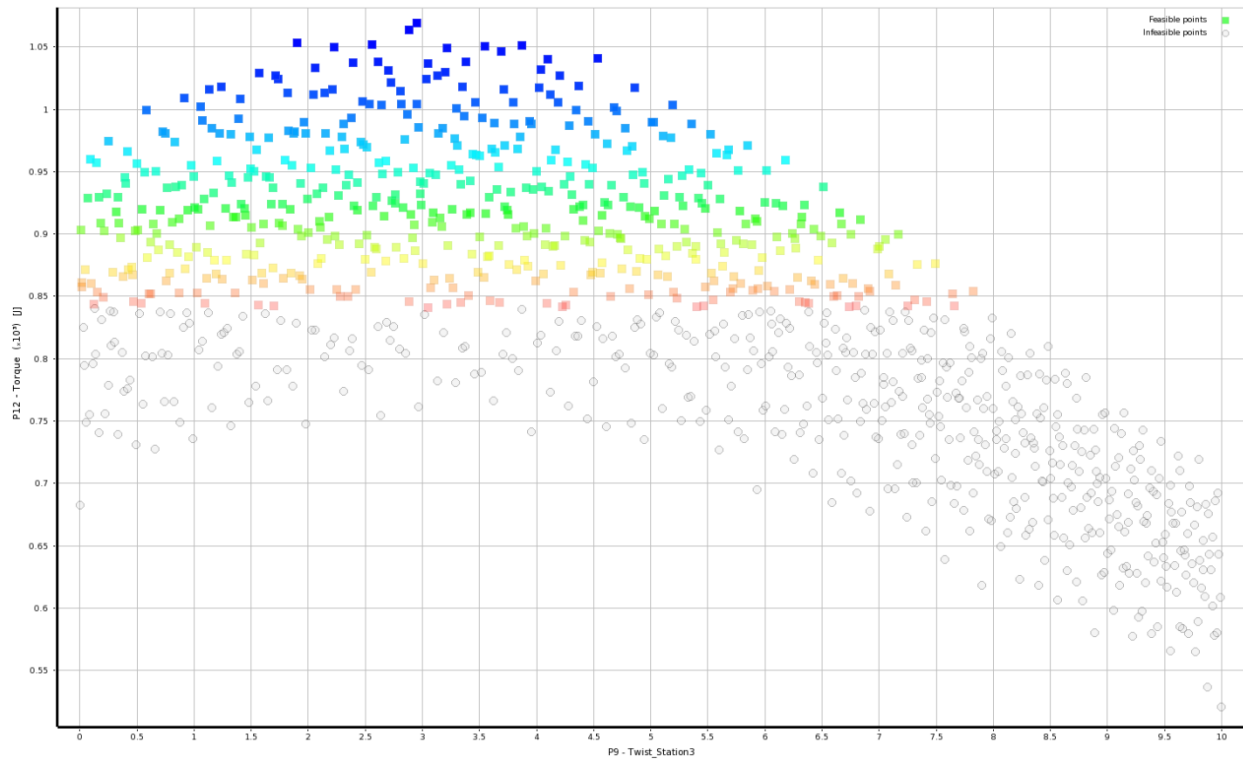| General Configuration:	
Turbine Make	Atlantic Orient Corporation
Turbine Model	AOC 15/50, 60 Hertz
Serial Number	None (This was the third AOC 15/50 turbine installed)
Rotation Axis	Horizontal
Orientation	Downwind
Number of Blades	3
Rotor Hub Type	Rigid
Rotor Diameter (m)	15
Hub Height (m)	25
Performance:	
Rated Electrical Power (kW)	50
Rated Wind Speed (m/s)	12.0
Cut-In Wind Speed (m/s)	4.9
Cut-Out Wind Speed (m/s)	22.3
Extreme Wind Speed (m/s)	59.5 (Peak Survival)
Rotor:	
Blade Make	Merrifield Roberts
Blade Type	Wood-Epoxy
Pitch	Fixed
Swept Area (m^2)	177
Online Rotational Speed (rpm)	65
Coning Angle (deg.)	6
Tilt Angle (deg.)	0
Blade Pitch Angle (deg.)	1.54° toward feather
Power Regulation	Stall Regulated
Over-speed Control	Centrifugal Override of Tip Brake Magnets
Drive Train:	
Gearbox Make	Fairfield/AOC
Gearbox Type	2-Stage Planetary
Gear Ratio	1:28.25
Generator Make	Magnatek
Generator Type	3-Phase Induction
Generator Speed, Nominal (rpm)	1800
Generator Voltage (VAC)	480
Generator Frequency (Hz)	60
Braking System:	
Mechanical (Parking) Brake: Make, Type, Location	Sterns Series 81,000; On Nacelle Aft of Generator
Aerodynamic Brake: Make, Type, Location	AOC, Electromagnetic Tip Brakes, At the Tips of all Blades.
Electrical Brake: Make, Type, Location	AOC, Dynamic Brake, Connected to the Tower Droop Cable at the Base of the Turbine.

Yaw System:	
Wind Direction Sensor	None
Yaw Control Method	Free-Yaw
Tower:	
Type	Three-Legged Steel Lattice
Height (m)	25
Control/Electrical System:	
Controller: Make, Model	Koyo, DirectLogic 205
Controller Type	Programmable Logic Controller
Software Version	Round Robin 86
Electrical System:	
Power Converter: Make, Model	None
Electrical Output: Voltage, Frequency, Number of Phases	480 VAC, 60 Hz, 3-Phases

REFERENCES

[1] Global Wind Energy Council (GWEC), *"Global Wind Statistics 2013"*, Dated: 05.02.2014
http://www.gwec.net/wp-content/uploads/2014/02/GWEC-PRstats-2013_EN.pdf

[2] A. Benmeddour, A. Wall, B. McAuliffe, P.J. Penna and J.C. Su, *"Overview of Wind Energy Research and Development at NRC-IAR (Canada)"*, National Research Council Canada, 2010.

[3] Brouchaert, J.-F., "Wind Turbine Aerodynamics: A State-of-the-Art. Lecture Series 2007-5, Von Karman Institute for Fluid Dynamics", Belgium, 2007.

[4] David Hartwanger and Andrej Horvat, *"3D Modelling of a Wind Turbine Using CFD"*, NAFEMS Conference, United Kingdom, 2008.

[5] Paul Veers, Gunjit Bir, Donald Lobitz, *"Aeroelastic Tailoring in Wind Turbine Blade Applications"*, Presented at Windpower '98, American Wind Energy Association Meeting and Exhibition, Bakersfield, California, April 28 – May 1, 1998.

[6] Tonio Sant, *"Improving BEM-based Aerodynamic Models in Wind Turbine Design Codes"*, DelftUniversity Wind Energy Research Institute DUWIND, January 2007.

[7] J. Gordon Leishman, *"Challenges in Modeling the Unsteady Aerodynamics of Wind Turbines"*, 21st ASME Wind Energy Symposium and the 40th AIAA Aerospace Sciences Meeting, Reno, NV; AIAA 2002-0037.

[8] B. Akay, C.S. Ferreira, G.J.W. van Bussel, *"Experimental Investigation of the Wind Turbine Blade Root Flow"*, AIAA.

[9] John Amund Karlsen, *"Performance Calculations for a Model Turbine"*, NTNU, June 2009.

[10] Seaforth Energy Inc., *"Technical Brief for AOC 15/50 Wind Turbine Generator Version 7.0"*, March 23, 2011.

[11] Tangler J.L., Somers D.M., *"NREL Airfoil Families for HAWTs"*, NREL. https://wind.nrel.gov/airfoils/

[12] Peter J. Schubel, Richard J. Crossley, *"Wind Turbine Blade Design"*, Energies 2012, 5, 3425-3449; doi:10.3390/en5093425.

[13] Juan P. Murcia; Álvaro Pinilla, *"CFD Analysis of Blunt Trailing Edge Airfoils Obtained with Several Modification Methods"*, Bogotá D.C., Colombia, June 2011.

[14] Naishadh G. Vasjaliya, *"Fluid-Structure Interaction and Multidisciplinary Design Analysis Optimization of Composite Wind Turbine Blade"*, ERAU Library, Thesis Section, August 2013.

[15] Nianxin Ren , Jinping Ou, "Dust Effect on the Performance of Wind Turbine Airfoils", J.Electromagnetic Analysis & Applications, 2009, 1: 102-107, doi:10.4236/jemaa.2009.12016, Published Online June 2009.

[16] Liersch J., Michael J., *"Investigation of the Impact of Rain and Particle Erosion on Rotor Blade Aerodynamics with an Erosion Test Facility to Enhancing the Rotor Blade Performance and Durability"*, Journal of Physics: Conference Series 524 (2014) 012023 doi:10.1088/1742-6596/524/1/012023

[17] P.J. Moriarty and A.C. Hansen, *"AeroDyn Theory Manual"*, NREL/TP-500-36881, Page 2, January 2005.

[18] Albert Betz, "*Betz Law for Wind Turbines"*, http://en.wikipedia.org/wiki/Betz%27s_law.

[19] D.M. Somers, *"The S819, S820, and S821 Airfoils"*, NREL/SR-500-36334, January 2005.

[20] Tangler, James L.; NREL and Somers, Dan M.; Airfoils, Inc., *"Airfoils for Wind Turbines"*, U.S. Patent No. 5,562,420, 8th October 1996.

[21] Lissaman, P.B.S., *"Wind Turbine Airfoils and Rotor Wakes"*, Wind Turbine Technology, D.A. Spera (Ed.), Chap. 6, ASME Press, 1994.

[22] Ladean R. McKittrick, Douglas S. Cairns, John Mandell, David C. Combs, Donald A. Rabem, and R. Daniel Van Luchene, *"Analysis of a Composite Blade Design for the AOC 15/50 Wind Turbine Using a Finite Element Model"*, SAND2001-1441, Unlimited Release, Printed May 2001.

[23] R. Jacobson, M. Meadors, E. Jacobson, H. Link, *"Power Performance Test Report for the AOC 15/50 Wind Turbine, Test B"*, Rev. 3, 8th August 2003.

[24] M.M. Hand, D.A. Simms, L.J. Fingersh, D.W. Jager, J.R. Cotrell, S. Schreck, and S.M. Larwood, *"Unsteady Aerodynamics Experiment Phase VI: Wind Tunnel Test Configurations And Available Data Campaigns"*, December 2001 • NREL/TP-500-29955.

[25] PROPID. Ver. 3.4. 12 Mar. 2008 http://www.ae.uiuc.edu/m-selig/propid/.

[26] Yang, S.; Chang, Y.; Arici, O., *"Navier-Stokes Computations of the NREL Airfoil Using a $k - \omega$ Turbulent Model at High Angles of Attack"*, J. Sol. Energ. T. ASME 1995, 117, 304–310.

[27] Wolfe, W.; Ochs, S., *"Predicting Aerodynamic Characteristics of Typical Wind Turbine Airfoils Using CFD"*, Technical Report SAND96-2345; Sandia National Laboratories: Albuquerque, NM, USA, 1997.

[28] Fuglsang, P.; Bak, C.; Gaunaa, M.; Antoniu, I., *"Design and Verification of the Riso-B1 Airfoil Family for Wind Turbines"*, J. Sol. Energ. – T. ASME 2006, 126, 1002–1010.

[29] Bertagnolio, F.; Sørensen, N.; Johansen, J., *"Profile Catalogue for Airfoil Sections Based on 2D Computations"*, Technical Report R-1581(EN); Riso: Roskilde, Denmark, 2006.

[30] Rumsey, C.; Ying, S., *"Prediction of High Lift: Review of Present CFD Capability"*, Progress In Aerospace Science 2006, 38, 145–180.

[31] Mayda, E.; van Dam, C., *"Bubble-Induced Unsteadiness on a Wind Turbine Airfoil"*, J. Sol. Energ. –T. ASME 2002, 124, 335–344.

[32] Sorensen N., Hansen M., *"Rotor Performance Predictions Using a Navier–Stokes Method"*, AIAA Paper 98-0025, 1998.

[33] Duque E., Van Dam C., Hughes S., *"Navier–Stokes Simulations of the NREL Combined Experiment Phase II Rotor"*, AIAA Paper 99-0037, 1999.

[34] Duque E., Burklund M., Johnson W., *"Navier–Stokes and Comprehensive Analysis for Performance Predictions of the NREL Phase VI Experiment"*, AIAA Paper 2003-0355, 2003.

[35] Le Pape, A., Lecanu, J., *"3D Navier-Stokes Computations of a Stall-regulated Wind Turbine"*, Wind Energy 2004, 7, 309–324.

[36] Zahle F., Sorensen N., *"On the Influence of Far-Wake Resolution on Wind Turbine Flow Simulations"*, In The Science of Making Torque from Wind. Journal of Physics: Conference Series, vol. 75. Technical University of Denmark, Lyngby, Denmark, 2007.

[37] Laursen J., Enevoldsen P., Hjort S., *"3D CFD Quantification of the Performance of a Multi-Megawatt Wind Turbine"*, In The Science of Making Torque from Wind. Journal of Physics: Conference Series, vol. 75. Technical University of Denmark, Lyngby, Denmark, 2007.

[38] B. Sanderse, *"Aerodynamics of Wind Turbine Wakes: Literature Review"*, ECN-e--09-016.

[39] F. Zahle, N. Sorensen, *"Overset Grid Flow Simulation on a Modern Wind Turbine"*, AIAA Paper 2008-6727, 2008.

[40] Q. S. Li, L. Zhi, F. Hu, *"Boundary Layer Wind Structure from Observations on a 325m Tower"*, J. Wind engineering and industrial aerodynamics, vol. 98(12), pp.818-832, 2010.

[41] J.Meyers, C. Meneveau, *"Large eddy Simulations of Large Wind-Turbine Arrays in the Atmospheric Boundary Layer"*, 48th AIAA Aerospace Sciences Meeting Including the New Horizons Forum and Aerospace Exposition, Orlando, Florida, January, 2010.

[42] Naishadh G. Vasjaliya, *"Fluid-Structure Interaction and Multidisciplinary Design Analysis Optimization of Composite Wind Turbine Blade"*, ERAU Library, Thesis Section, August 2013.

[43] Tsewang Rabga Shrestha, *"3D Aerodynamic Optimization of NREL VI Wind Turbine Blade for Increased Power Output and Visualization of Flow Characteristics"*, ERAU Library, Thesis Section, April 2014.

[44] ANSYS® FLUENT*, "Theory Guide Release 14.5"*, USA: ANSYS®, Inc., 2014.

[45] F. R. MENTER, "*Turbulence Modeling for Engineering Flows*", ANSYS®. Inc.

[46] Box, G. E. P., and Wilson, K. B., (1951), *"On the Experimental Attainment of Optimum Conditions,"* Journal of the Royal Statistical Society, Series B, 13, 1-45.